Investigation of opto-electrical and structural properties of atmospheric pressure chemical vapor deposition of fluorine-doped tin oxide

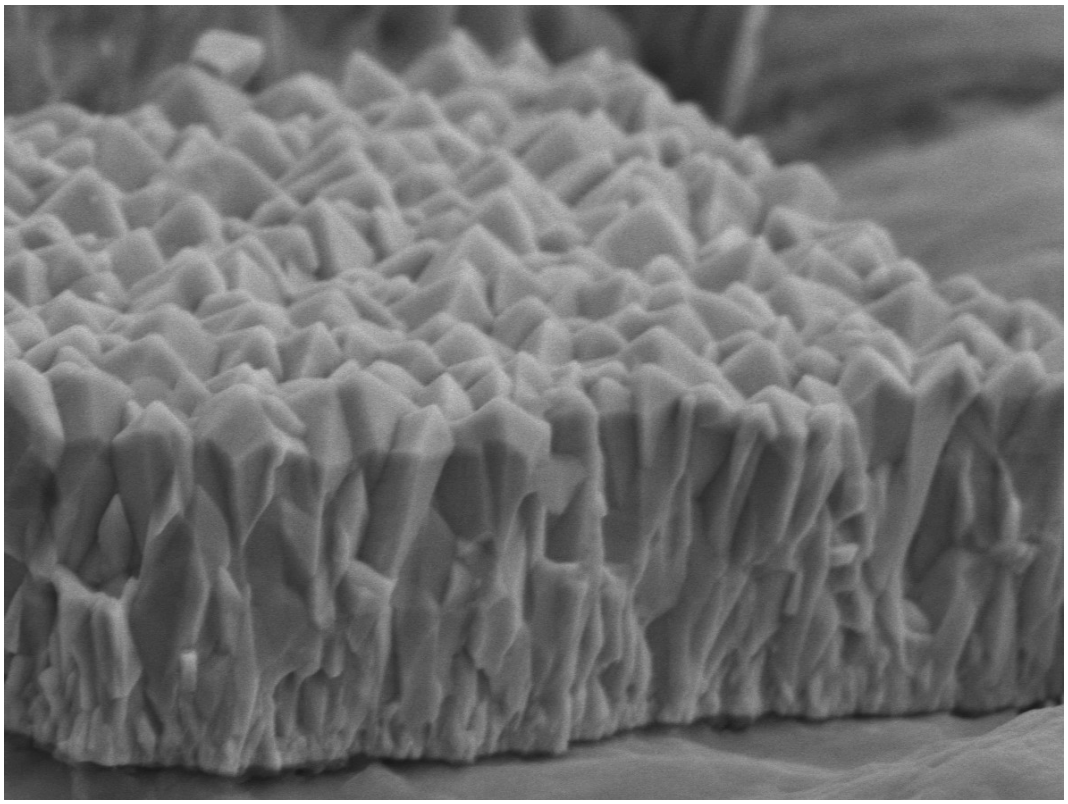

Subhadra Venkataraman (5611008)

Under the guidance of: University supervisor - Prof. dr. ir. Arno Smets
Company supervisor - Dr. ir. Jimmy Melskens

June 25, 2023

TU Delft Delft University of Technology

PVMD Delft University of Technology

HyET Solar Flexible light weight solar modules

Investigation of opto-electrical and structural properties of atmospheric pressure chemical vapor deposition of fluorine-doped tin oxide

by

Subhadra Venkataraman

to obtain the degree of Master of Science
at the Delft University of Technology,
to be defended publicly on Tuesday June 27, 2023 at 11:00 am.

Student number:	5611008	
Project duration:	November 1, 2022 - June 27, 2023	
Thesis committee:	Prof. dr. ir. Arno Smets,	TU Delft,ESE-PVMD, Supervisor
	dr. Malte Ruben Vogt	TU Delft,ESE-PVMD
	dr. Aleksandra Lekic,	TU Delft,ESE-IEPG
	dr. Paula Perez Rodriguez,	TU Delft,ESE-PVMD, Daily supervisor
	dr. ir. Jimmy Melskens,	HyET Solar, Company supervisor

TU Delft Delft University of Technology

PVMD Delft University of Technology

HyET Solar Flexible light weight solar modules

Contents

Acknowledgements

This thesis was an amazing rollercoaster ride, with several ups and downs along its way. I would like to thank everyone who helped me stay motivated during this journey from the bottom of my heart. I would especially like to thanks my colleagues, friends and guides at HyET and at TU Delft who helped keep spirits high throughout this gruelling period. Everything that could go wrong did go wrong, but in the end it all worked out thanks to the positivity and motivation surrounding me. I am still in awe of the amazing people I am surrounded by and the amount of help I got. Special thanks to my friends and family for putting up with the miserable version of me towards the last few months of the thesis. I am very aware how lucky I am and very grateful for you. This section was by far the easiest and the fastest part of the report to write. I have a lot to say but I will stop here with a huge thank you to friends, family, coworkers and guides from the bottom of my heart. I would also like to thank the externals, who were bound by no ties to read my report and agree to be on my committee, but who still accepted and were extremely accommodative of my request to hand in my report a week before the defence.

List of Abbreviations

Abbreviations/chemical formulas	Expansion
AFM	Atomic Force Microscopy
Al	Aluminum
APCVD	Atmospheric Pressure Chemical Vapor Deposition
CH_3OH	Methanol
CVD	Chemical Vapor Deposition
FTO	Fluorine doped tin oxide
LAC	Lab scale APCVD machine
MeOH	Methanol
PEN	PolyEthylene Napthalate
SEM	Scanning Electron Microscope
SnO_2	Tin oxide
TTC	Tin tetra Choride
TCO	Transparent Conductive Oxide

Abstract

The atmospheric pressure chemical vapor deposition (APCVD) process for the deposition on FTO is considered one of the most complex processes in the HyET Solar production process. An increase in the deposition speed can increase the roll-to-roll foil speed which can directly translate to lowering production costs, furthermore increasing throughput. In this thesis several experiments were performed aimed at improving opto-electrical performance while moving to higher deposition speed. However using a production machine for the experiments leads to material consumption. Henceforth, a lab-scale research tool was designed for material deposition. Thereby, optimizing the recipe and investigating the corresponding material growth can be done faster and this has been demonstrated using the lab-scale deposition tool. This tool also facilitates the investigation in different stages of growth to have a deeper understanding of each process parameter, thus making it possible to formulate the correct parameters and facilitate the knowledge transfer to the production APCVD machine.

1 Introduction

The introduction is the first chapter that jointly comprises of the motive, approach, and results of this thesis. The first chapter aims to make the reader familiar with the main concepts that are associated with the thin film solar cell and module production at HyET Solar and explains the questions that motivated this thesis.

This chapter will start with a short introduction into thin film solar cells. Next transparent conductive oxides and chemical vapor deposition (CVD) will be discussed.

This will help the reader grasp the approach of the company to PV production and the relevancy of underlying research in this project and PV production in general. This chapter will end with the description of the aim of the research, the main research questions that will be addressed, the adopted approach, and the structure of the report.

1.1 Thin film silicon photovoltaic cells

Sunlight is directly converted into electric current by photovoltaic (PV) cells with the help of semiconductor materials such as silicon (Si), cadmium telluride (CdTe) or copper indium gallium arsenide (CIGS). Presently the world PV-market is dominated by crystalline silicon (c-Si) with highest efficiencies of around 26.81% [1]. In this report, we will focus on thin film solar cells which have far lower efficiencies of about (7-18)% depending on the PV material and the structure used. Figure 1 shows the flexible HyET thin film power foil, which is based on thin film silicon as the active layer that converts sunlight into electricity.

Figure 1: HyET thin film power foil [2]

Thin film solar cells require a much thinner layer of active material- in comparison to c-Si the active layer stack is 100 times thinner- and hence consumes less material. These cells are flexible and light weight hence can be used in several niche applications, especially building integrated photovoltaics. Less material usage and cheaper production processes motivates research in this area.

In a PV cell, incoming photons with an energy greater than the material's bandgap will have a certain chance to be absorbed within the material and will proceed to generate an electron-hole pair. In order to prevent the immediate recombination, the electron and hole should be physically separated from each other by means of a built-in electric

field which originates from the p and n doped layers on either side of the intrinsic layer (i-layer).

The p-layer is doped with boron (B) which functions as an electron acceptor while the n-layer is doped with phosphorous (P) which functions as a donor. The resulting layer structure is called the pin-stack. Figure 2 depicts the sectional overview of the thin film solar module at HyET Solar.

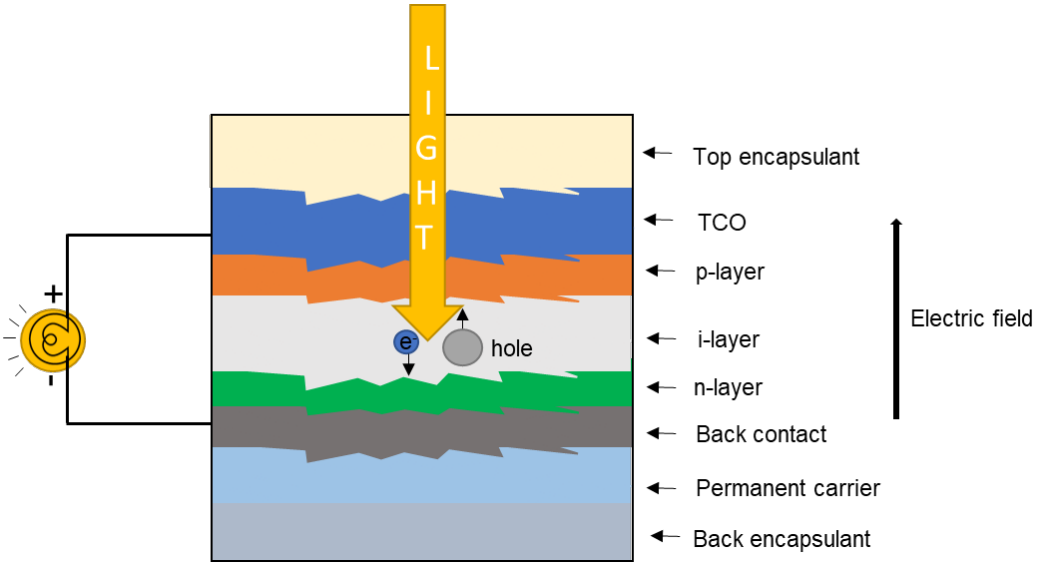

Figure 2: Sectional overview of HyET Solar cell layout[3]

Finally, to close the circuit, the PV cell structure consists of conducting materials on both sides of the pin-structure. A transparent conductive oxide (TCO) such as fluorine-doped tin oxide (FTO) is used as the front contact and acts as a window layer to the incoming sunlight. The back contact is provided by a stack of aluminum-doped zinc oxide (AZO) and aluminum (Al) which can be further optimized to reflect light not absorbed by the pin, back into the active layer. Finally, the stack is protected on the top and bottom side with encapsulants. The top encapsulant is made of glass or polymers and the top encapsulant should be transparent to incoming light.

In this report, we will focus on the production of the front contact, a transparent conductive oxide fabricated by means of the atmospheric pressure chemical vapor deposition (APCVD) method.

1.2 Production process at HyET

This section contains a short overview of the production process at HyET Solar, Arnhem. Roll-to-roll (R2R) manufacturing is used to produce flexible thin-film solar modules. Aluminium is used as the temporary carrier. The aluminum foil can withstand high process temperatures which are involved in APCVD and help in production of high-quality transparent conductive oxide (TCO). The following steps are involved in the R2R production process at HyET as described by Hamers et al. in [3].

1. Texturing of aluminum foil (Pre-treatment)- Crater like structures are created in the surface of the aluminium foil by etching with sodium hydroxide (NaOH), after which the Al foil is cleaned in an acid bath of phosphoric acid (H_3PO_4) to remove residues from etching.

2. Front contact TCO deposition - Fluorine doped tin oxide is deposited as the front contact layer on the textured aluminum foil using the atmospheric pressure chemical vapor deposition (APCVD) method. This process will be explained in detail in the following sections.

3. Active layer deposition - The silicon deposition is carried out using the plasma-enhanced chemical vapour deposition (PECVD) technique. The silicon layer is deposited in superstrate configuration at a temperature of

about 170 °C and a Radio frequency (RF) of 13.56 MHz. There are eight zones in the deposition machine where the p-doped, intrinsic and n-doped layers are deposited.

4. Series connection - The cells are defined using laser scribes to establish a monolithic series interconnection. The first scribe is made through FTO and a-Si:H layers which is used to separate adjacent cells. The series interconnection is made using the second scribe that connects the n-doped and p-doped layers of adjacent cells.

5. Deposition of back contact : Typically 70 nm of aluminium doped zinc oxide (AZO) is sputtered as the back contact using RF sputtering while 300 nm of Al is sputtered using DC sputtering.

6. Transfer to permanent carrier : Lamination of the stack with the back contact is carried out on a permanent carrier foil to provide rigidity.

7. Removal of Aluminum : Wet chemical etching is used to etch the temporary aluminum foil to expose the active region of TCO/Si. An encapsulation layer is then used at the back to ensure mechanical stress is transferred to a polymer material.

8. Encapsulation : The modules are cut and encapsulated from the front side to protect them from moisture or chemical attack. Then the electric interconnectors are added to finish the product.

1.3 Transparent conductive oxides(TCOs)

Transparent electrodes are needed for thin film solar cells on the side of the cell facing the sunlight in order to collect and transport the current generated within the active layers of the solar cell to the metallic contacts on the side of the PV module. Since these electrodes are always oxides and need to be transparent such that the light can reach the silicon layers, they are referred to as transparent conducting oxides (TCO). The TCO acts as a window layer and guides the incident light into the absorber layer of the solar cell. Since the refractive index of the TCO is between that of the encapsulant and the absorber layer, it provides an anti-reflective effect. The texturing in the TCO scatters incident light and helps in prolonging the average path length of the photons through the absorber, boosting the absorption of light in the absorber and consequently increasing the photo current [3].

TCOs are a class of metal oxides that combine the properties of optical transparency and conductivity. Their transparency is due to their sizable bandgap and their conductivity is due to a highly dispersed conduction band owing to the favourable overlap of spatially extended metal orbitals in the metal oxide [4]. They are extrinsically doped to improve conductivity. Commonly used TCO materials are indium oxide, zinc oxide, tin oxide, and titanium oxide. Sputtering, pulsed laser deposition, atomic layer deposition and chemical vapor deposition have been used to prepare thin films of conductive oxides.

The charge carrier concentration, and the mobility determines both the conductivity and the transparency of the TCO. One of the important requirements of a TCO is that it should have low resistivity to prevent excess ohmic losses during lateral charge transport to the metal grid. Since resistivity is determined by charge carrier concentration, we can achieve low resistivity values with high charge carrier concentration which is promoted by doping. The TCO should also serve as an anti-reflection coating to maximize the transmitted light and be highly transparent to minimize the parasitic absorption losses.

1.4 Chemical vapor deposition (CVD)

Due to high volume, good uniformity, improved hardness and adhesion and fast deposition rates the CVD technique is preferred in industry. This technique can be used for depositing uniform, homogeneous coatings over large area at high deposition rates. Usually with CVD, gaseous reactive chemicals are used to deposit a thin film on top of a substrate. The reaction is driven usually through heat transfer; alternatively plasma can also be used. By adjusting the experimental parameters, it is possible to deposit thin films of varying thickness and growth rates [5].

According to [6], the CVD process proceeds in the following steps as shown in Figure 3:

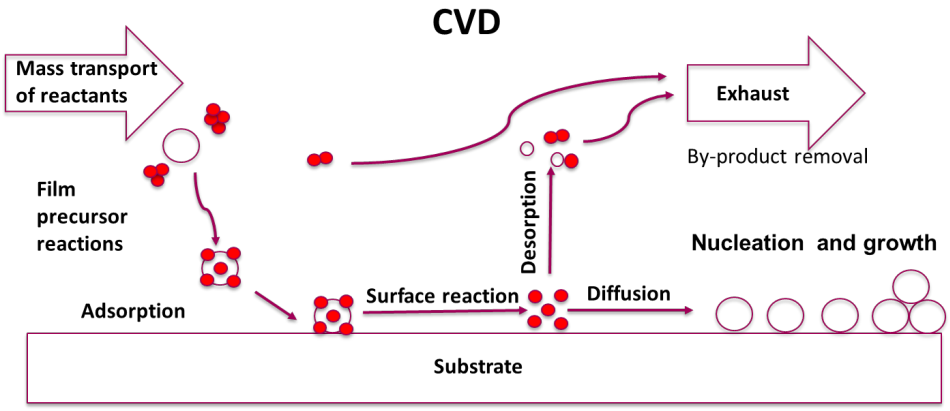

Figure 3: Schematic view of CVD process. This picture has been adapted from [7]

The first phase involves mass transport of reactants. This begins with the introduction of the atomic species to the substrate surface. This is followed by film precursor reactions, adsorption of the species on the substrate surface, and the surface reaction. The final step is the nucleation and growth phase which involves diffusion of adsorbed species to the nucleation site, followed by formation and coalescence of clusters [7]. The by-products from the film precursor and surface reactions are desorbed and removed by means of exhaust pressure [7].

At HyET, fluorine-doped tin oxide layers are used as transparent electric front contacts. The technique used to deposit these layers is atmospheric pressure chemical vapor deposition (APCVD). This technique is attractive as it is compatible with industrial requirements of high process speed, up-scaling to wider substrates, and low costs.

1.5 Aim of the thesis

The APCVD process is a complex process, involving gas phase reactions, surface reactions based on precursor chemistry, dynamic gas flows based on injector geometry and various process conditions that governs these reactions. Due to the complexity of the system when used in an industry, these processes may have some disadvantages such as low process yield, and high product fall out.

To increase the production capacity and lower the cost/kWh at HyET Solar, wider carrier (Al) foil is planned to be commissioned. Thus, improving the current APCVD process parameters to match the new Al foil width is indispensable. Excess resources would be unnecessarily consumed if a production machine is used in carrying out experiments to identify the required process parameters. Henceforth, a lab-scale research tool was designed for material deposition. Thereby, optimizing the recipe and investigating the corresponding material growth can be done faster. It also facilitates the investigation in different stages of growth to have a deeper understanding of each process parameter. Eventually, the right process parameter can be formulated and the knowledge transfer to the production machine can be made easy.

To further dwell in this direction, the following questions need to be addressed:

1) How do the different deposition conditions (web speed, flow rate of the gases) affect the opto-electrical and morphological properties of the TCO?

2) What is the dependence of substrate temperature on the growth rate of the material?

3) Can we improve opto-electrical properties by varying gas flow ratios?

3.1) What effects does HF have on the opto-electrical and morphological property of the deposited FTO and how to identify optimal dopant concentration.

3.2) How does variation in water concentration affect the FTO properties.

4) Can we achieve control over growth rate, larger grain, higher mobility, and extend the transmission range by changing methanol and water concentrations while lowering dopant concentration ?

5) What effect does methanol have on the nucleation and growth rate?

In the aim of finding the answers to these questions, this thesis is divided into the following phases -

1) Recipe optimization aimed at improving opto-electrical performance while moving to higher webspeed and gas flow rates of TCO films.

2) Characterization of the deposited material in terms of surface morphology, optical, and electrical properties.

3) Making the lab-scale research tool (LAC) operational and perform depositions on the LAC.

The APCVD process for the deposition on FTO is considered one of the most complex processes in the HyET Solar production process. An increase in the webspeed can increase the roll-to-roll foil speed which can directly translate to lowering production costs, furthermore increasing throughput. Recipe optimization aimed at improving opto-electrical performance while moving to higher webspeed will further contribute to lowering the time required to produce modules by improving the performance and hence reducing the cost/kWh, through higher efficiency and economics of scale respectively.

1.6 Structure of the report

To mark the end of chapter one, this section will give a short review on the structure of the report. Chapter two deals with the literature review on the opto-electrical properties of transparent conductive oxides. This chapter will also include the influence of nucleation, process parameters such as temperature, and precursors on the properties of the deposited material.

Chapter three will contain information on the experimental setup. This chapter consists of two sections. In section one, the production APCVD machine, the apparatus, materials used, and the precursor chemistry specific to the process at HyET Solar will be discussed. The choice of chemicals used will be discussed in detail. In section two, the lab-scale APCVD tool and the deposition using this tool will be reviewed.

In chapter four we will summarize the methods used to analyze the samples. Chapters five and six will deal with experiments performed on the production APCVD machine. Chapter five will begin with studying the effect of gas flow and web speed variations on morphological and opto-electrical properties of deposited FTO. This is followed by chapter six which will discuss experiments on recipe optimizations. The first experiment is identifying the optimal dopant concentration followed by the second experiment on recipe variations for HF, water and methanol. This will be followed by chapter seven which will involve experiments on the LAC to study the influence of methanol on morphology. In chapter eight we will discuss overall conclusions followed by chapter 9 which will contain a short summary of the thesis. Chapter ten will contain recommendations for the future work.

Finally, the Appendix will contain detailed information on the haze measurements and XRD analysis, followed by an analysis of the quality of the deposited TCO. This will be followed by a description of the safety model built to calculate leak rates of gases through the injector and the challenges faced in getting the LAC operational and the approach taken to troubleshoot the problems in the LAC.

2 Literature review

This chapter discusses the literature review done during the start of the thesis. The first section begins with a discussion on the opto-electrical properties of the TCO and the trade off between them. This is followed by discussing the precursors used in the HyET process for the deposition of FTO, followed by an extensive literature review on the influence of methanol on the TCO properties. This chapter will end with a section on the influence of process parameters such as deposition temperature on the growth rate and electrical properties of the TCO.

2.1 Properties of TCO

In this section we will discuss the electrical, and optical properties of TCO in detail.

For solar cells to increase their efficiency, it is important that the TCO has to be able to transmit light in the regions of the electromagnetic spectrum that can be absorbed by the cell. Transparent conductive oxides should thus be highly conductive and highly transparent in the active wavelength region of the absorber as it guides incident light to the active layers of the solar cell. Creating nano-textures in TCO thin films helps in increasing the average path length of the photons (in the absorber layer) as these textures scatter the incident light [8],[9].

The TCOs should exhibit low resistivity to efficiently collect charge carriers. Low sheet resistance would result in lower power loss, I^2R [9]. In addition to basic properties such as average transparency around 80 percent in visible range and low resisitivity in the order of 10^{-3} Ωcm or less, morphological and chemical properties are also important and and vital to device performances [10].The morphological features on the surface of the TCOs determine the degree of light scattering and thus the light trapping. In superstrate devices there is a possibility that large morphological features of TCO can result in cracks or pin-holes in successive layers, leading to shunting issues [8].

Haze is defined as the ratio of the scattered transmitted light divided by total transmitted light. For transmitted light, high haze translates to an increase in the optical path length of the scattered light into the absorber layer, which increases optical absorption in the absorber, increasing the conversion efficiency of the cell [11].

In PV devices, it is preferable to have low resitivity to facilitate current transport. [10]. To improve the conductivity of the TCO, the possible ways are to control the charge carrier concentration or the mobility. This is related to the intrinsic material of the TCO and the type and concentration of the dopant. The conductivity is related to the charge carrier concentration and mobility through the following formula:

$$\sigma_{n,p} = n_e * q * \mu \tag{1}$$

where $n_e$is the charge carrier density or the density of electrons in the conduction band (hole in the valence band), q is the charge of the electron (1.6x10^{-19} C) and μ is the mobility of the charge carriers.

TCO needs to have a minimum carrier concentration in the order of $10^{20} cm^{-3}$. This is achieved with the help of doping. In order to avoid absorption of light over most of the solar spectra it is also necessary for the TCO to have a bandgap greater than 3.2 eV [10].

According to [10], in wide band gap oxides, good electrical conductivity and high transparency in visible region are achieved by introduction of degenerate doping. Doping refers to the introduction of appropriate external impurities with the intention to improve conductivity. Therefore, to improve conductivity, dopants are introduced in the material. Depending on the valency of the dopants, the doping will induce p or n type conductivity. TCOs are most commonly doped with n-type impurities [10].

Most TCOs are heavily doped so that the Fermi level is positioned above the conduction band edge. The photons need a larger energy than the fundamental bandgap to excite electrons from valence band to unoccupied state in the conduction band, as the conduction band is partially occupied. The required additional energy is called Burstein-Moss shift. This can be seen in Figure 4.

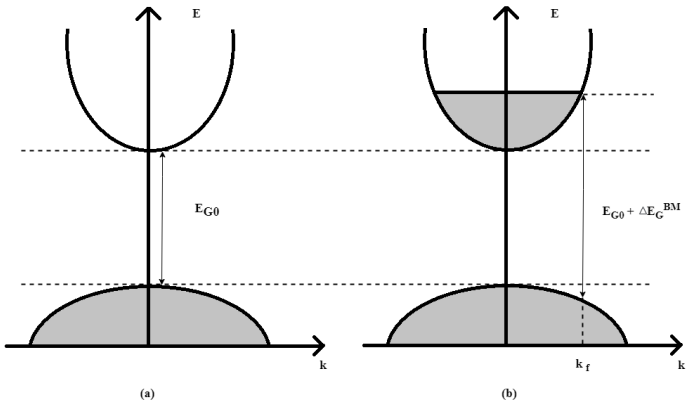

Figure 4: (a) Schematic band structure of a TCO with parabolic bands separated by the fundamental gap and with vertical optical transitions. (b) Widening of the optical gap by the Burstein-Moss shift

The Burstein Moss effect shifts the transparency limit towards the short wavelengths and increases the energy required to make an interband transition. However, there is an increase in Fermi energy due to increase in density of charge carriers while the transparency decreases with increase in doping.

However, higher level of doping can deteriorate the optical properties by increasing the absorption near infra-red wavelengths. At higher levels of charge carrier concentration in the TCO, there is a reduction in transmission due to increased IR reflectivity as well as free carrier absorption [12]. Hence reducing the carrier density in the TCO can extend the transmission spectrum. However, good electrical properties of the TCO need to be maintained. Finding an optimum between high transparency and high carrier density is an important issue in designing TCOs. High carrier density also reduces the carrier transport which is also limited primarily by ionized impurity scattering. In addition, the scattering rate could be significantly increased due to clustering of dopant ions at high dopant concentration. [4]. The transmittance, reflectance and absorptance spectra of AZO can be found in Figure 5.

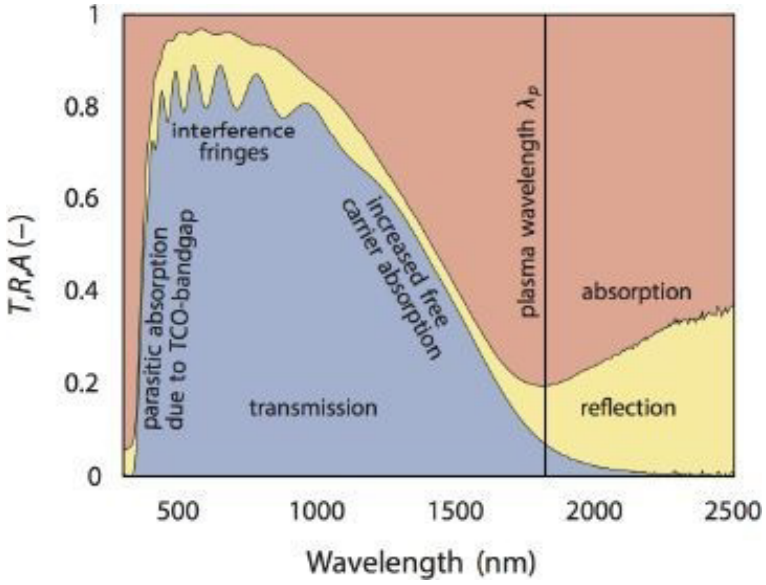

Figure 5: An example for the transmittance, reflectance and absorptance of AZO with thickness of 880 nm This figure has been adapted from [9]

The TCO should also have a low absorption coefficient in the near UV-VIS-NIR region. Photons with an energy greater than the bandgap are absorbed, hence the transmittance in the shorter wavelength (in the near UV region) is limited by the bandgap. for longer wavelengths. However, the transmittance is very high for photon energies below the bandgap and the absorption increases after a broadly transmissive part with increasing wavelength, due

to free carriers absorption [9].

Furthermore, for the wavelengths longer than the plasma wavelength (the wavelength at which the reflection of the TCO is close to zero), the material becomes very reflective, which is the second transmission edge. For application in solar cells, the plasma wavelength of the TCO should be longer than the bandgap of the absorber material. However, the plasma frequency is proportional to the free carrier density. Therefore, longer plasma wavelength corresponds to lower free carrier density. Thus it is very important to design the TCO by finding an optimum between high carrier density and high transparency [9].

The Drude model [4] can describe the phenomena: that increasing carrier density reduces transmission in the infrared as this increase in charge carrier density results in shifting the plasma frequency towards the visible range of the spectrum.

The Drude theory uses plasma frequency to express the reflection by free carriers according to the following equation.

$$\omega_p = \sqrt{\frac{q^2 n_e}{\varepsilon_0 m^*}} \tag{2}$$

where ω_p is the plasma frequency, n_e is the measured carrier concentration, q the elementary charge m^* is the effective mass, and ε_0 is the permittivity of free space.

Drude absorption leads to an increased free carrier absorption of the free carriers generated by doping at low photon energies. This is detrimental since most photons in the solar spectrum are low energy photons. Furthermore, there is a reduction of the refractive index n at low photon energies with the increased Drude contribution. This leads to enhanced free carrier reflection due to refractive index mismatch. High mobility helps in boosting conductivity at lower n_e thus improving NIR transparency and also reducing ω_p [4].

Thus it is preferred to improve the conductivity by increasing the mobility, μ. Mechanisms that negatively influence the mobility of the electrons are scattering at grain boundaries and scattering due to ionized impurities. These two phenomena depend on material thickness, quality of layers, and the deposition method.

One possible method to enhance mobility is to grow large grain TCOs. This reduces the number of grain boundaries from which scattering can occur thus enhancing mobility. [12]

The sheet resistance R_{Sq} can be improved by increasing either carrier electron density n_e or carrier mobility μ.

$$\rho = 1/(n_e * q * \mu) \tag{3}$$

$$R_{sq} = \frac{1}{\mu n e d} \tag{4}$$

where d is the thickness of the deposited TCO, ρ is the resistivity, q is the elementary charge and n_e is the charge carrier density.

As discussed earlier, optical absorption in the visible wavelength range will increase with increasing carrier density, however it will not increase with mobility. Hence increasing the electron mobility is the best way to optimize the front TCO properties for its application in solar cells and modules.

2.1.1 Factors that affect electron mobility

Unavoidable scattering processes such as phonon scattering (arising due to thermal lattice vibrations) and scattering due to ionized impurities (from intentional dopants) limit the electron mobility, while other forms of scattering arise due to material imperfections including, grain boundaries, impurities, and unintentional dopants (such as oxygen vacancies).

Scattering at grain boundaries and scattering at ionized impurities are two dominant mechanisms that limit the mobility of electrons. Grain boundary scattering dominates within the carrier concentration ($2 * 10^{19} cm^{-3}$ - $2 * 10^{20} cm^{-3}$) while coulombic scattering due to the introduction of ionized dopants, known as ionized impurity scattering, is the dominant scattering process for carrier density values greater than $2 * 10^{20} cm^{-3}$ [4].

In polycrystalline materials, grain boundary scattering is a dominant source of scattering. A high electronic trap density is exhibited at the grain boundaries and the conduction electrons from the grains charge these electrons. As a result, at the grain boundary, there is a formation of a space-charge region which mirrors the trapped charge and transport over this energetic barrier is dominated by thermionic emission [4].

The scattering rate is strongly dependent on the carrier density. If the trap density is higher than the carrier density per grain, the grain will be depleted and little traps will be filled. At higher carrier density, all traps are filled and little depletion of the grain occurs. The scattering at grain boundaries can still be low in this case as screening is enhanced and hence transport can transition from thermionic emission to tunneling. Scattering at the grain boundary is maximized when the barrier height is maximized at an intermediate carrier density. Maximizing grain size and defect passivation at grain boundaries (for example with H) are some steps to mitigate grain boundary scattering [4].

In moderate to high doping densities ($> 10^{19} - 10^{21} cm^{-3}$) , strong scattering exists due to the charged nature of dopants. Therefore, doubly charged oxygen vacancies are detrimental to mobility since the net scattering from ionized dopants is doubled compared to singly charged dopants [4].

The effect of temperature on electron mobility will be detailed in section 2.5.1.

2.2 Tin oxide

Indium tin oxide is presently the most commonly used TCO. Since indium is toxic and is expensive, being a rare earth element, a renewed interest has grown to find replacements which have similar or higher performance. Since the TCO films are exposed to silane plasma during amorphous silicon deposition, a chemically stable TCO is required, which involves lower production costs, higher availability and lower toxicity [13]. FTO shows higher chemical resistance (in acidic and hydrogen rich environments) and thermal resistance and better mechanical properties than that of ITO while also being cheaper and less toxic than ITO [14].

Since flexible PV modules are not covered in glass but rather by a polymeric top encapsulant that is always slightly accessible to air or moisture, chemical stability is essential. SnO_2:F is substantially more resistant to acid and moisture damage than ZnO, another often used TCO material [3].

Tin oxide (SnO_2) has the desirable properties of being transparent in the visible region, reflective in the infrared region, has low electrical resistance, is chemically inert, stable to heat treatment and has high mechanical hardness [6].

SnO_2 has a tetragonal rutile structure with one tin atom surrounded by six oxygen atoms in a octahedral structure and oxygen atoms surrounded by three tin atoms in a triangular structure. In its completely stoichiometric form it would be an insulator. The cause of non-stoichiometry and conductivity in pure SnO_2 is caused due to oxygen vacancies during oxide growth. Structure of SnO_2 is shown in Figure 6.

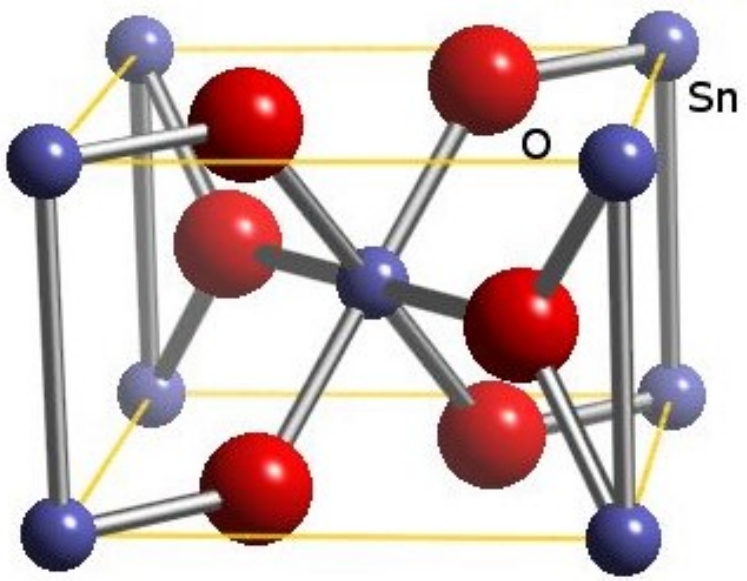

Figure 6: Crystal structure of SnO_2. This has been adapted from [15]

SnO_2 has a high bandgap of 3.6 eV and thus a very low intrinsic carrier concentration. The conductivity of the tin oxide increases with higher oxygen vacancies. It is thus doped with elements such as chlorine / fluorine to further enhance its conductivity. n-type doping offers better stability and helps to achieve sufficiently low values of resistivity [15].

2.3 Precursors

In this section we will look at the precursors used in the FTO deposition process.

2.3.1 Tin tetra chloride (TTC)

There is a wide array of precursors used for obtaining tin oxide films which are highly transparent and conductive. For the deposition of fluorine doped tin oxide, several deposition methods can be used such as chemical vapor deposition, sputtering, and spray pyrolysis using the precursor tin tetra chloride [16]. Tin tetra chloride ($SnCl_4$) is used as the precursor in the APCVD process in our experiments with water. Tin oxide is formed by the hydrolysis reaction of tin-tetra chloride in the following reaction.

$$SnCl_4 + 2H_2O \rightarrow SnO_2 + 4HCl$$

2.3.2 Methanol

On addition of methanol, the morphological properties of the resulting grains change due to the desorption of HCl during the deposition process. This is given by the equation below.

$$HCl + CH_3OH \rightarrow CH_3Cl + H_2O$$

As discussed in [6], there is an increase in grain density during early stages of film formation and reduction in the grain size due to the increase in the adsorption sites for TTC and water on desorption of HCl from the surface by the methanol. Methanol helps in controlling the intial layer formation which in turns helps in controlling the final layer formation. This will be discussed briefly in section 2.4.1.

2.3.3 Fluorine doping

Fluorine has been chosen as the dopant for tin oxide, due to its thermal and chemical stability in addition to its low processing costs. On introducing the dopant, oxygen is replaced by fluorine ions along with the release of a charge

carrier. The ionic radius of fluorine is 0.133 nm which is closer to the ionic radius of oxygen which is 0.132 nm. Thus the doped F is included into the tin oxide network without disturbance, ensuring increased conductivity [16].

Increasing the level of F-doping leads to an increase in the Fermi energy until the edge of the conduction band. At high doping densities, the Fermi level moves away from the conduction band edge into the conduction band. This is called degenerate doping. Thus the the band gap exceeds 4 eV and the transparency of the film is improved in the ultra violet range [16].

2.4 Nucleation

The initial growth of a film on a substrate or on another film is referred to as film nucleation. In polycrystalline materials, the final grain size is influenced strongly by the nucleation (initial layer formation). Precursor reactivity towards the substrate surface is one of the key factors concerning the initial layer morphology. Large grain size and high carrier mobility can also be achieved by controlling the nucleation stage. When the nucleation density is lower, larger grains are obtained since each grain has more room to grow before coalescing together. Another strategy to improve grain size would be to subject the already fully polycrystalline film to high temperature annealing. This leads to the grains merging with other grains and also helps in removing defects in the crystal [4].

Nucleation in case of the formation of SnO_2 crystals can be controlled by means of adding methanol to the gas mixture needed for growing the SnO_2 film. We will look at this in detail in the following section.

2.4.1 Literature review on influence of methanol on TCO properties

According to Archer in [12], varying the amount of water and methanol in the deposition process, helped in tuning the grain size in the deposited TCOs. Reducing the amount of methanol also gave rise to larger grain size. Initially, with increase in methanol content there was a decrease in resistivity (due to increase in charge carrier density since methanol is a reducing agent).

The deposition rate also decreased with an increase in methanol content due to competing nature of MeOH on surface sites with water. The carrier concentration did not vary significantly over the methanol range studied. There was a slight decrease in haze observed with increasing MeOH concentration but there was little change in overall transmission. In this study, at higher levels of HF, the electrical properties were more favourable. However at lower levels of HF, the transmission extended further into the near infrared (due to a decrease in the number of charge carriers there is less absorption in the near IR) [12].

Literature shows that the electrical resistivity of a film decreases with the addition of methanol. Matsui et al. in [6], studied the influence of alcohol on grain growth of tin oxide deposited using chemical vapor deposition. Atomic force microscopy (AFM) results showed increased micrograin density on addition of methanol and decreased grain size. The chlorine contamination at the bottom of the film was highest when methanol was used. In this study, they propose a model of the desorption of chlorine by reaction with alcohol in the early stage of the film growth which can explain the morphological change in the tin oxide grains.

$$HCl + CH_3OH \rightarrow CH_3Cl + H_2O$$

Hydrogen fluoride is added to increase the carrier concentration through fluorine doping into tin oxide micrograins.

Carrier scattering is a dominant scattering mechanism in tin-oxide with decreasing film thickness. As with decreasing film thickness the scattering due to ionized impurities, becomes the major scattering mechanism, Grain boundary scattering can be ruled out as a dominant scattering mechanism with increased grain size. Addition of MeOH increases conductivity of TCOs. MeOH is a reducing agent and results in an increase in carrier concentration. Therefore Matsui et al, [6] use alcohol to control the grain size and density during the nucleation stage to ultimately control conductivity. The effect of addition of methanol on density and deposition rates can be found in Figure 7.

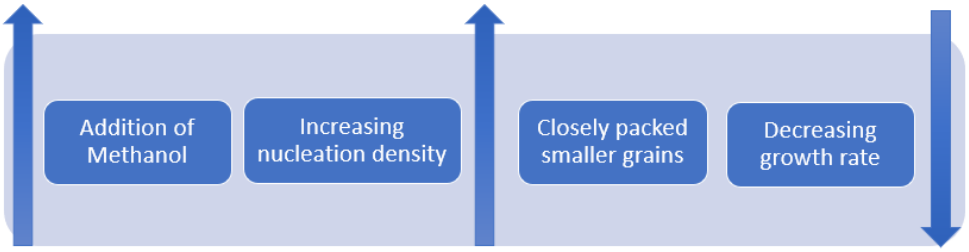

Figure 7: Effect of methanol on density and deposition rate [13, 6]

According to [6] alcohol addition increased the density of the micro-grains and decreased the grain size simultaneously. This concurs with what was observed in [12]. Archer observed that, lowering the concentration of MeOH favours the growth of larger grains. With increasing concentration of MeOH, it was observed that the growth rate of the coating decreased due to the competing nature of MeOH on surface sites with water. The grains become smaller but they retain their pyramidal shape as they become more homogeneous in size. There is a slight decrease in resistivity as the concentration increases and a similar trend is observed with sheet resistance. The carrier density and the mobility also increase initially before levelling off.

Figure 8 captures the different growth stages of the film on addition of methanol and without methanol.

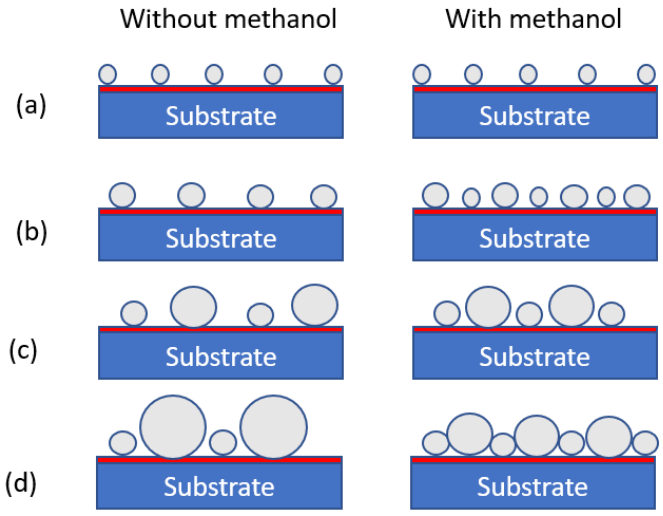

Figure 8: Stages of grain growth : (a) Nucleation stage (b) Initial growth (c) Intermediate growth (d) Final growth [6]. Figure adapted from [17]

From [6], [12], it is clear that the average grain size decreases with the dosage of methanol while the density of nucleation increases with the dosage. With the right amount of methanol dosage, the nucleation can be controlled. The grain growth mode observed by Matsui in tin oxide without methanol is isolated island mode, where islands are formed further apart and grow larger before coalescence. This type of growth can be classified as Volmer-Weber type growth [18]. On introducing small doses of methanol, first closely packed grains are observed and on increasing the dosage, interconnected small grains with irregularly large grains can be observed [6].

An increase in water concentration can cause the growth rate to rise and also increases the grain size. [12]. Water adsorption controls the tin oxide film deposition rate. Increasing methanol dose can lead to a decrease in nucleation rate due to the nature of methanol to compete with water for reactive surface sites [6].

In [19] the influence of different concentrations of methanol on the properties of tin-oxide has been investigated. In [19] it is interesting note that they were able to achieve electron mobility values to 55 cm^2/Vs for a lower concentration of methanol (in water) while higher concentrations led to a decrease in the mobility. The dominant mechanism for higher mobility values at lower concentration of methanol could be due to the lowering of the potential barrier at the grain boundaries (due to reduction of the gap between the grains) which enhances mobility.

The effect of methanol addition on the formation of tin oxide by chemical vapor deposition was studied by Gotoh and Mizuhashi in [13]. They observed that on adding methanol, there was a gradual decrease in the deposition rate due to the competition between methanol and water for available surface sites for absorption on the surface of tin oxide where hydrolysis is taking place. The reduction effect by methanol led to an increase in electrical properties of the film in terms of carrier density and mobility.

For methanol and water variations, we should consider the deposition rate because it is a heterogenous reaction that involves steps of diffusion, adsorption, hydrolysis and desorption.

Irrespective of the substrate used, addition of methanol reduces the deposition rate, further proving that addition of methanol is an inhibiting factor. The methanol molecules occupy parts of water absorption sites reducing deposition rate. In additon to gas-phase reactions due to presence of methanol, equilibrium (between physical desorption and chemical adsorption of water) shifts towards the chemisorption side. Physisorption involves weak van der Waals forces which weaken with a rise in temperature while chemisorption involves formation of chemical bonds involving activation energy and is favored by a increase in temperature. At higher temperature, adsorption of methanol becomes weak compared to water, providing more adsorption sites for water.

The deposition rate increases slightly with increase in temperature as rise in temperature leads to an decrease in the activation energy. This decrease in activation energy can contribute to the increasing trend of chemisorption of water molecules due to the presence of methanol [13]. In [13] Gotoh et al, demonstrated that improvement in crystallinity and increase in grain size led to an increase in mobility.

Methanol being a reducing agent increases carrier density. The carrier density is much larger in the sample with methanol rather than in the sample with no methanol. Grain size became smaller in spite of the increase in mobility. The formation of less reactive species like CH_3Cl reduces the amount of free HCl. From the experiments by Gotoh in [13], it is probable that either the elimination of the electron traps formed by chlorine in the grain boundary or the formation of very thin grain boundaries (normally assumed to be composed of chlorine containing substance) as a consequence of chloro methane leaving the surface due to the reaction of HCl with methanol are responsible for the increase in mobility despite the decrease in grain size.

Gotoh [13] concluded that methanol helped in providing films of low resistivity either through good crystallinity, through reducing behaviour of methanol or elimination of grain boundary structure composed of chlorine containing substance.

2.5 Process parameters

Some of the important parameters that determine the quality of FTO layers deposited are the substrate temperature, exhaust pressure, deposition time, carrier gas flows and flow rate of the precursors. The thickness of the deposited FTO material can be controlled by varying the exhaust pressure in the APCVD machine. The thickness of the deposited material also varies as a function of the deposition time. The deposition temperature defines the kinetics of the various reactions between the chemical species present and the regime.

In literature, it is further explained that the crystallographic phase of the deposited material is conditioned by the substrate temperature during the growth process [16]. Sanon et al. observed the change in preferred orientation from (101) to (200) at temperatures over 350 °C [20]. We will look at this in detail in section 2.5.1.

Olopade et al., in [21], study the effect of deposition temperature and deposition time on sheet resistance and transmittance. It was observed that the films with a large deposition time were thicker and appeared milky, and the surface roughness is known to increase with thickness, giving it a milky appearance. This revealed improved conductivity due to low sheet resistance values (due to increased charge carrier incorporation linked to high doping

gas concentrations) but the transmittance to light in the UV region was poor (which can also be explained by free carrier absorption in all spectral ranges) [22],[21]. This is summarized in Figure 9.

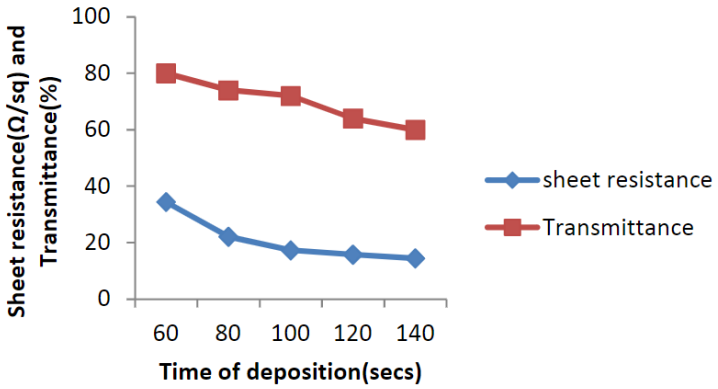

Figure 9: Dependence of sheet resistance and transmittance of FTO film as a function of deposition time [21]

The relation between high doping gas concentration, low resistivity, and high IR optical absorption for films with similar thickness can be related by the Drude model, which further explains that in a highly doped sample, there are a large number of free carriers which in turn lead to an increase in IR optical absorption.

Increasing dopants during TCO growth in addition to increasing free carrier concentration introduces new defects. The increase in optical absorption in the visible region proves the introduction of new defects. Therefore, the optical absorption of TCO films grown by APCVD is sensitive to deposition parameters such as doping gas concentration and substrate temperature during growth [22]. Figure 10 shows the effect of temperature increase on opto-electrical properties of the film.

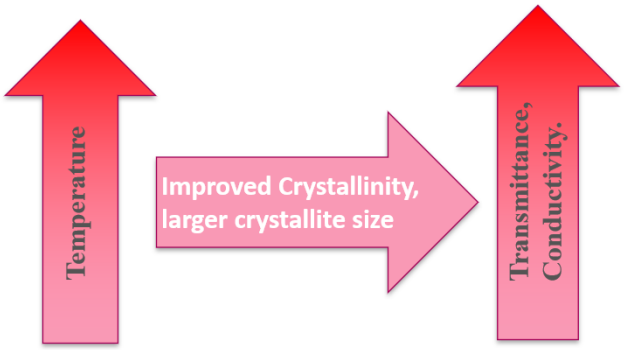

Figure 10: Dependence of Transmittance and conductivity of FTO film on deposition temperature [21]

2.5.1 Effect of deposition temperature on growth rate and electrical properties

The deposition temperature influences the growth rate and the grain size which in turn influences electrical properties of the film. In this section, we will review studies where the effect of increasing deposition temperature on deposition rate and electrical properties of the deposited films are analysed and reported.

Figure 11 reports the variation in growth rate of tin oxide prepared from $SnCl_4$ and H_2O as a function of temperature reported in several studies[23],[13],[20].

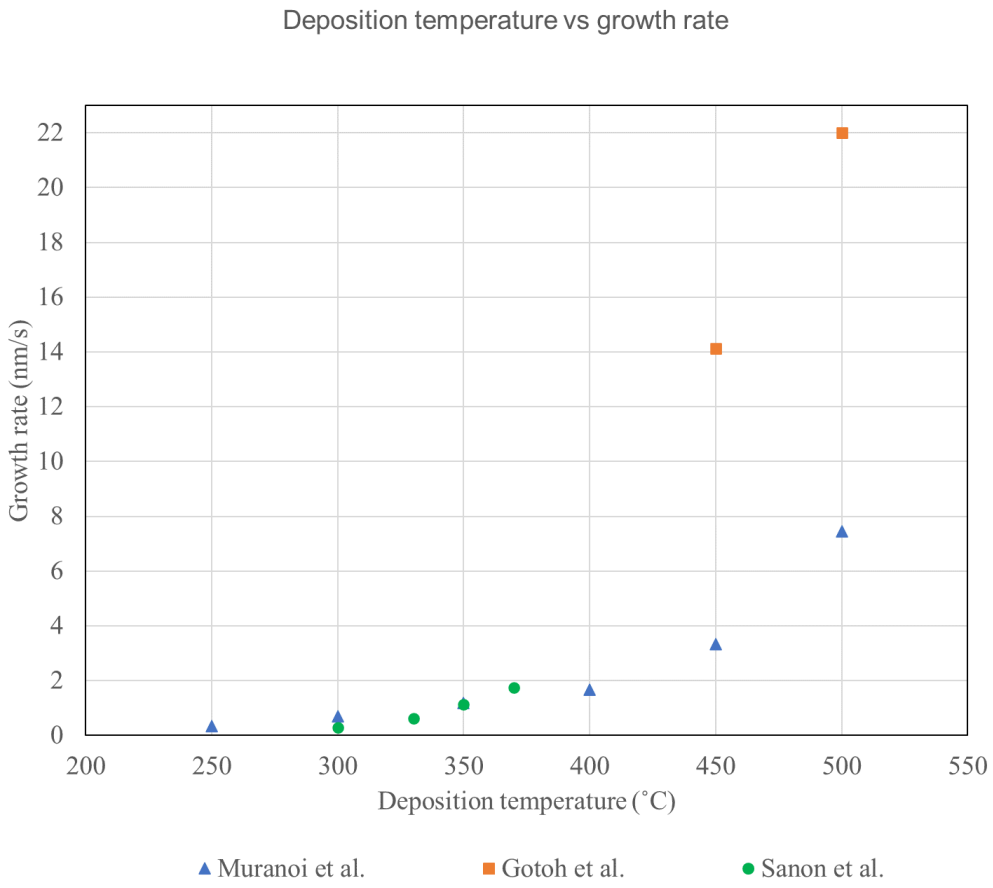

Figure 11: Deposition temperature vs growth rate for $SnCl_4$ $+H_2O$ system
[23] [13] [20]

The quantitative difference in growth can be explained by differences in reactor system and process conditions.

Sanon et al. studied the growth and characterization of tin oxide films prepared by CVD in [20]. The preferred orientation for the film deposited upto 350 °C was (101). Beyond this temperature, the preferred orientation changes to (200) which can be seen in Figure 12a. At 350 °C they noticed a change in the electrical properties of the film as well which is plotted in Figure 12b. In their setup, the sheet resistance is minimum at the position where the temperature is maximum, indicating that for higher substrate temperatures, the sheet resistance will keep decreasing. The films were noticed to become hazy and greenish white in color which reduced the transparency at these high temperatures. It was assumed that re-evaporation of the material might have caused the haziness [20].

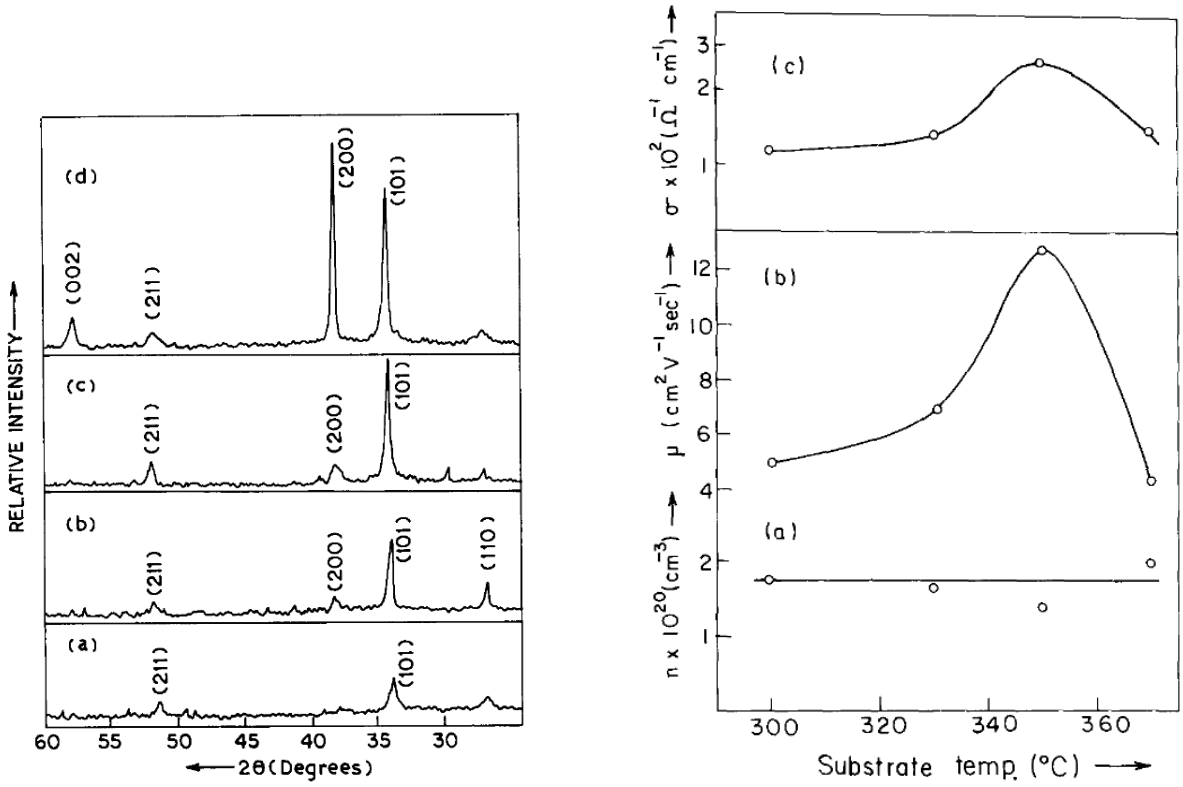

(a) A (b) B

Figure 12: A) X-ray diffraction patterns for films deposited at different substrate temperatures: (a) 300 °C; (b) 330 °C; (c) 350 °C; (d) 370 °C [20], B) Variation in carrier concentration n, mobility and conductivity of SnO_2 films with substrate-temperature These figures have been adapted from [20].

The reaction is kinetically controlled as the growth rate was found to increase with increase in temperature as seen in Figure 11. This concurs with the studies done by [13] and [23]. The grain size also showed an increase with increase in temperature [20]. The carrier concentration was found to be nearly independent of the deposition temperature while mobility was found to be highest at the highest temperature of 350 °C used in the experiment. This can be seen in Figure 12b.

In [20] it was observed that more and more defects are annealed out for films grown at high temperatures which result in an increase in mobility. However, beyond 350 °C there is a drop which is assumed to be caused by the presence of voids inside the film, while a change in preferred orientation could be another reason.

In Figure 11, from the experiments performed by Muranoi et al. Sanon et al. and Gotoh et al., [23], [20] and [13], it is clear that the growth rate increases by around a factor of 2 for a 50 °C increase in temperature.

The deposition rate increases slightly with an increase in temperature as a rise in temperature leads to a decrease in the activation energy. [13]

The Arrhenius equations relates the rate of a chemical reaction to the magnitude of the activation energy:

$k = Ae^{-E_a/RT}$

where
k is the reaction rate coefficient or constant
A is the frequency factor of the reaction. It is determined experimentally.
R is the universal gas constant
T is the temperature in Kelvin

2.5.2 Effect of temperature on mobility

In [23], undoped tin oxide films were produced using $SnCl_4 - H_2O$ and $SnCl_4 - H_2O_2$ reaction systems on soda glass from relatively low temperatures of 250 °C upto 500 °C by CVD. It has been observed by Muranoi et al. in [23], that with an increase in deposition temperature, the grain size increases for deposited films. Mobility is observed to increase with increase in deposition temperature. There is also a change in deposition rate as function of temperature, which is plotted in Figure 11.

Muranoi et al. in [23], observed that the electrical properties such as the mobilities and resistivities were an order of magnitude higher for the films produced using the $SnCl_4 - H_2O$ reaction system compared to the films produced by the $SnCl_4 - H_2O_2$ reaction system between 250 and 500 °C. The electrical properties are influenced by the absorption of water/hydrogen peroxide and the grain size which is determined by the deposition temperature and the reaction mechanisms. For both the reaction systems, the grain size and mobilities increased with increase in deposition temperature.

According to results from [23] deposition rate and resistivity are proportional to the square root of the flow rate and the mobility is inversely proportional to the deposition rate. We will focus on the $SnCl_4 - H_2O$ system as it is more relevant to this research.

The scattering at grain boundaries which is one of the dominant scattering mechanisms that limits mobilities is reduced as the grain size increases with increasing deposition temperature, consequently reducing the number of grain boundaries. The resistivity tends to initially drop with increasing deposition temperature after which it stays constant. This initial decrease is considered to be due to an increase in carrier concentration, after which the resistivity approaches a constant value as defects which contribute to carrier concentrations might be annealed out at high temperatures [23].

3 Experimental setup

3.1 Introduction

This chapter is divided into two sections. 3.2 contains information on the production APCVD machine which was used for depositing fluorine-doped tin oxide. Section 3.3 consists of information on the lab-scale APCVD research tool used to perform depositions of undoped tin oxide.

APCVD is a CVD deposition technique at atmospheric pressure (1 bar). Typically, a "moving belt reactor" is employed in this procedure in industry. This method's benefit is continuous deposition on large surfaces. Controlling the film morphology and thickness is challenging due to the lack of control caused by rapid growth rates and complex temperature and concentration profiles [17].

3.2 Experimental setup 1 : Production APCVD machine

In this section, the details on the Production APCVD machine which is the experimental setup used for most of the experiments are detailed.

3.2.1 Materials

Hydrolysis reaction between stannic chloride, ($SnCl_4$) (TTC) and water is used to deposit the tin oxide films. In HyET, methanol of 0.05% (wt%) concentration is premixed with water. The presence of methanol retards the rate of the reaction and results in denser films. Without methanol addition, grain growth dominates over nucleation, but with methanol nucleation and grain growth occur together. To increase the number of conduction electrons, fluorine from hydrogen fluoride is used as the dopant.

Aluminium substrate around 350 mm wide and 100 microns thick is used as the substrate for fluorine doped tin oxide (FTO) deposition. All of the depositions were performed with two injectors (while there is room for three injectors in the machine). To determine what each injector contributed individually to the overall thickness, the injectors were tested separately. It was found that when both the injectors were set at the same set point, injector 2 which was placed perpendicular to the drum contributed to 51% of the overall thickness of the coating while injector 3 which was placed with a tilt angle of 44.6°, contributed to the rest of the thickness.

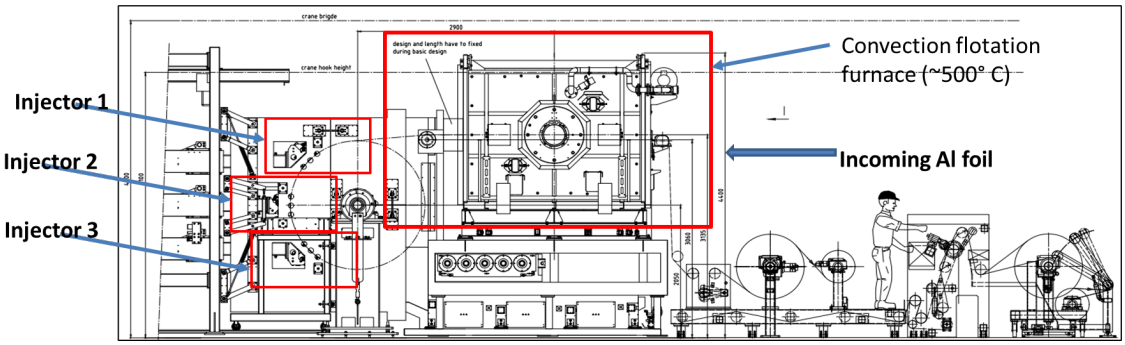

Figure 13: Overview of APCVD machine [24]

3.2.2 Apparatus

The large scale roll to roll APCVD production machine was used for the experiments. The coating section is located in the central part of the furnace. Two injectors are used to blow the process gases which react on the aluminum substrate which is heated to around 505 °C as it is transported to the main drum from the entrance of the furnace. The substrate temperature is assumed to be around 500 °C due to the temperature decrease caused by rather cool CVD gas and radiation cooling to the injector assembly at relatively low temperature. The transportation speed of the aluminum foil is varied throughout the experiment and is reported in the experimental Table 3.2.5. The

experimental set up is depicted in Figure 14.

Figure 14: Experimental setup of the production APCVD machine

TTC, methanol/water mixture and HF are evaporated using controlled evaporator mixer and are fed into pipelines heated at 150 °C. 10 ln/min of Nitrogen heated to 150 °C is used as the carrier gas. Several thromocouples mounted on different positions of the drum record the temperature of the substrate. The injectors have two slits. One slit for the deposition of the process gases and the other slit is connected to the exhaust. The exhaust pressure is set to 20 Pascals. The TTC and water/MeOH mixture get mixed up with HF and TTC mixture at the entry of the injector. The quantity of the reactant gases are adjusted by the respective coriolis flow meters.

The electrical properties were measured by Hall effect under a magnetic field of 0.55 T and current of 10 mA.The surface morphology was examined by Scanning electron microscopy, (SEM) and Atomic Force Microscopy (AFM) (for selected samples) and the optical properties were determined by means of transmittance measurements on the UV-VIS spectrophotometer.

3.2.3 Precursor chemistry

In our APCVD reactor, tin oxide film is deposited on the metal foil by hydrolysis of tin tetra chloride with water. The characteristic process is determined by a complicated interplay between gas phase, surface reactions, and fluid dynamics of the CVD reactor. In this subsection, we will focus on the reaction kinetics of hydrolysis of tin tetra chloride.

From literature, it is known that $SnCl_4$ forms a stable complex with water molecules in gas phase, resulting in a $SnCl_4 \cdot 5\,H_2O$ complex [25]. The complex contains two strongly bound water molecules resulting in an octahedral surrounding of the Sn atom. The remaining three water molecules are less strongly bound to the Sn atom. In [25], the activation energies of the different possible tin complexes for hydrolysis has been calculated by Reedijk. The geometries of the four most important tin species predicted by Reedijk are represented in Figure 15. Reedijk observed that the presence of F in the TTC complex, lowers the energy required for hydrolysis which might influence the growth speed.

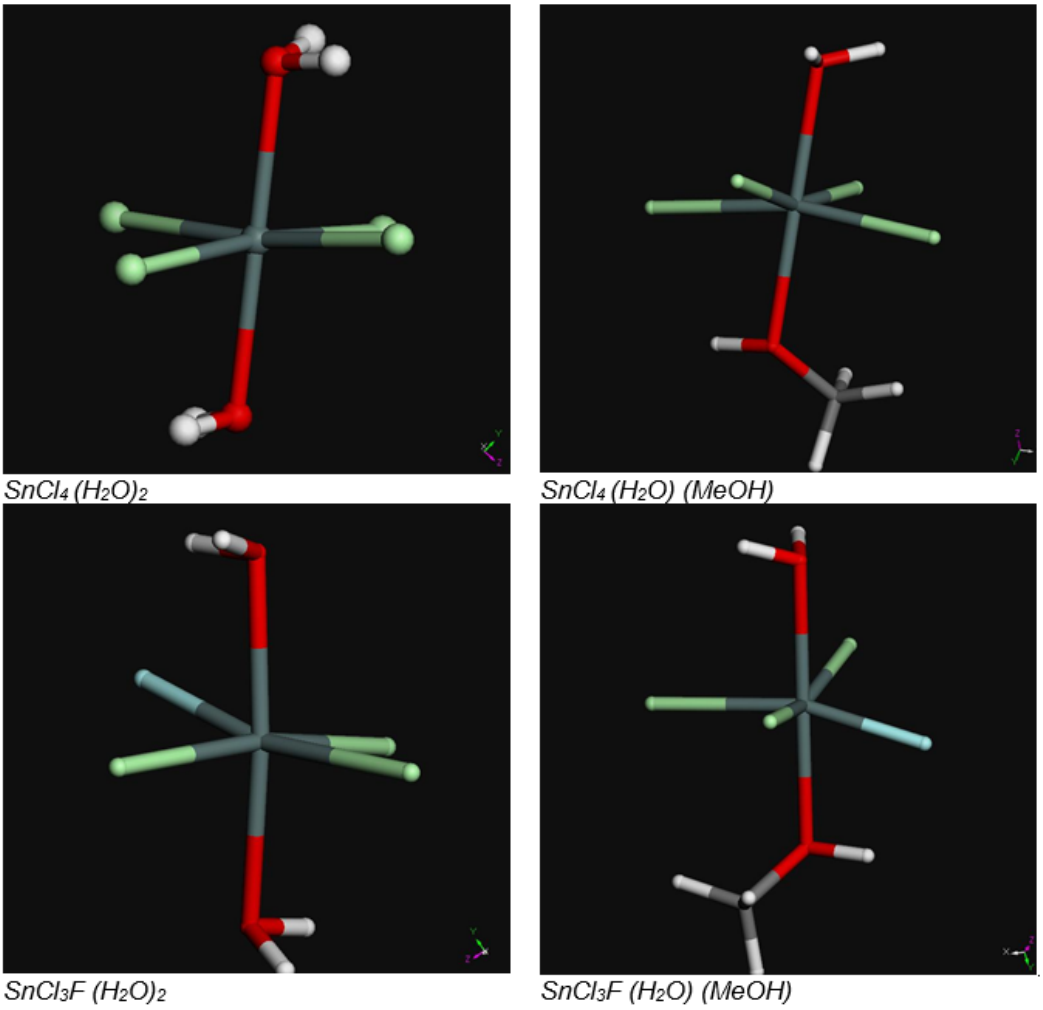

Figure 15: Geometries of the four most important tin species predicted by Reedijk and adapted from [25]

The calculations done by Reedijk in [25] predict that it is not likely that the hydrolysation of the TTC takes place in gas phase since the energy required for this is very large. The study concludes that the reaction takes place at the tin oxide surface when the molecule is incorporated in the surface. The reaction has been found to be more favourable when the Cl-ligand is replaced with the F-ligand as the energy required for this has been calculated to be very low around 140.54 kcal/mol (this reaction can take place in gasphase).

It is interesting to note now that in the production APCVD machine, TTC, and HF are evaporated separately and mixed together after evaporation and travel in the same pipeline. It is probable that this helps in increased growth rate.

In the experiments done by Goshtagore and Gotoh in [26], [13], it was demonstrated that for temperatures above 400 °C the hydrolysis reaction is not dependent on temperature. The diffusion of the species to the substrate (Eley-Rideal mechanism) limits the reaction. Here the $SnCl_4$ gas molecules react with two water molecules adsorbed on the surface of the substrate. This can be visualized in Figure 16 [26].

In Eley-Rideal mechanism, one of the reacting species adsorbs on the surface. Molecules of the other species pass by and interact with other adsorbed species. The product subsequently is either desorbed or stays on the surface.

3.2.4 Hydrolysis reactions

The hydrolysis reaction of tin tetra chloride proceeds as follows [6].

$$SnCl_4 + 2H_2O \rightarrow SnO_2 + 4HCl$$

Here water acts as a chemisorbed species and reacts with gaseous $SnCl_4$. This mechanism can be visualized below.

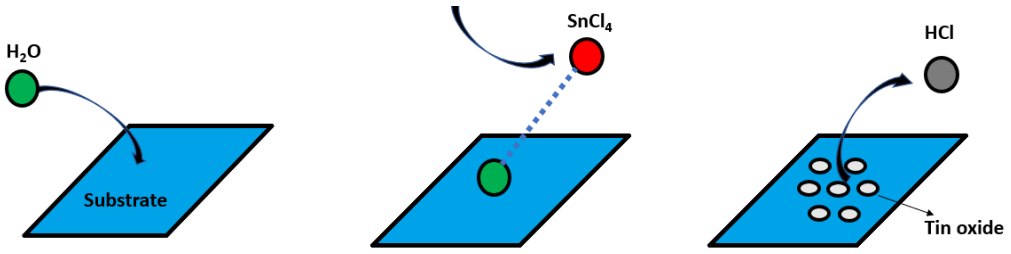

Figure 16: (a) H_2O molecules adsorb on the surface (b) $SnCl_4$ molecules pass by and interact with H_2O on the surface (c) A HCl molecule is formed which desorbs and tin oxide is deposited on the surface [11]

3.2.5 Reaction with methanol

The desorption of HCl from the substrate surface proceeds as below proceeds as follows [6].

$$HCl + CH_3OH \rightarrow CH_3Cl + H_2O$$

Since the reaction must be activated by thermal energy, in temperatures above 400 °C, the hydrolysis of $SnCl_4$ can be assumed to take place on top of the substrate surface resulting in negligible activation energy.

In our experimental setup, the deposition pattern is noticed along the width of the injector. The injector is maintained at 150 °C and placed 1.5 - 2 mm away from the drum which is at 500 °C. Gas molecules of $SnCl_4$, the water-methanol mixture and HF-TTC mixture are mixed in the short pipe at the inlet of the injector, the fluid flow is diverted into four branches and further mix in the bevels with three horizontal indentations for homogeneous mixing of the reactants in the injector. The residence time of the gas molecules in the injector should be as low as possible to prevent the deposition of an intermediate product inside the injector. At the exit of the mixing plate, the gases exit a slit through the injector, hit the aluminum substrate with laminar flow, where the surface reaction takes place and then the desorbed products are removed through the exhaust. A schematic of one of the injectors during deposition is represented in Figure 17.

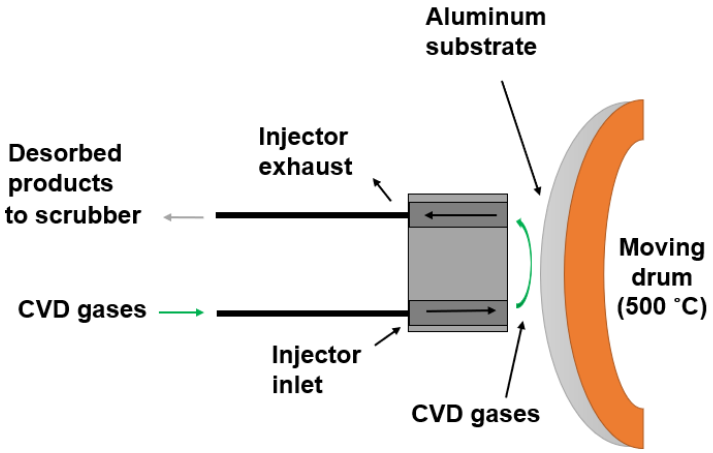

Figure 17: A schematic of one of the injectors of the production APCVD machine during deposition

Deposition parameter	Baseline recipe value for production APCVD
TTC CEM temperature (°C)	150
HF evaporation temperature (°C)	70
Water and methanol CEM temperature (°C)	70
N_2 flow (TTC, HF) (ln/min)	10
N_2 flow (Water, Methanol) (ln/min)	10
Ratio of H_2O/TTC	6.5
Ratio of CH_3OH/TTC	0.0018
Ratio of HF/TTC	0.4
Deposition speed (m/min)	0.6

Table 1: Deposition parameter and baseline recipe value for production APCVD machine

The carrier gas is represented in ln per minute which expands to normalized litres per minute. The standard reference in this case is selected to be gas at a temperature of 0 °C and a pressure of 1013.25 hPa(a). This is a standard term used in the mass flow controller (MFC) supplied by Bronkhorst.

One of the crucial manufacturing processes in the roll-to-roll fabrication of solar cells is continuous atmospheric pressure chemical vapor deposition, or APCVD. It is crucial that a uniform coating of FTO be applied to as much of the substrate as feasible in this step. The economics of the process are improved by the widening the deposition zone, which allows for the production of more square meters of solar cells on the same foil. The vapor flow pattern between the injector and the substrate layer is one of the most crucial process factors affecting the deposition width. The injector design, injector functioning, and injector positioning all have an impact on the laminar vapor flow, which is powered by forced convection.

During our experiments, the injector 3 wrap angle was changed to 44.6 °, from 45°. This is because there was a hypothesis that some of the process gases exiting the injector on their way to the substrate was either leaking into the surrounding area or being extracted through the exhaust, narrowing the deposition width.

The gas conversion efficiency of $SnCl_4$ to SnO_2 was estimated to be around 26% by calculating the volume of the deposited SnO_2 from the result of experiments. This matches with the gas efficiency calculated by R. Schlatmann through prior experimental work which was found to be between 22.5 to 27.5 percent [27]. Consequent CFD work on the gas flows in the injector by Goldschmidt in [27] was also estimated to be around 26.9 percent.

3.2.6 Background information on the APCVD production machine

The chemicals are stored in a 316 stainless steel vessel (316 stainless steel is resistant to corrosion due to presence of molybdenum). The chemicals are of 99.9% purity. The HF cylinder was replaced in January 2023 and the TTC vessel was refilled in March 2023. The experiments were carried out in April 2023.

Foil breakage in the production APCVD machine is most commonly due to incorrect web tension regulation, misalignment of the rollers, winding problems due to malfunction of the diameter sensor resulting in an incorrect web tension which ultimately leads to foil breakage. Less frequently, an error in the driver of the motor stops the main drum stops moving and the foil heats up and melts over the surface of the drum.

3.3 Experimental setup 2: Lab-scale APCVD (LAC) research tool

In order to gather information for the upscaled production capacity at HyET Solar, which depends on deposition over wider Al foil than is now employed as well as deposition at higher web speeds, it is necessary to upgrade the current APCVD system. In order to analyze the deposited material at various phases of growth, identify and address the faults originating in the formed material, and apply the lessons learned from this to the large-scale APCVD machine, a lab-scale research instrument was created. A schematic of the lab-scale APCVD (LAC) instrument can be found in Figure 18.

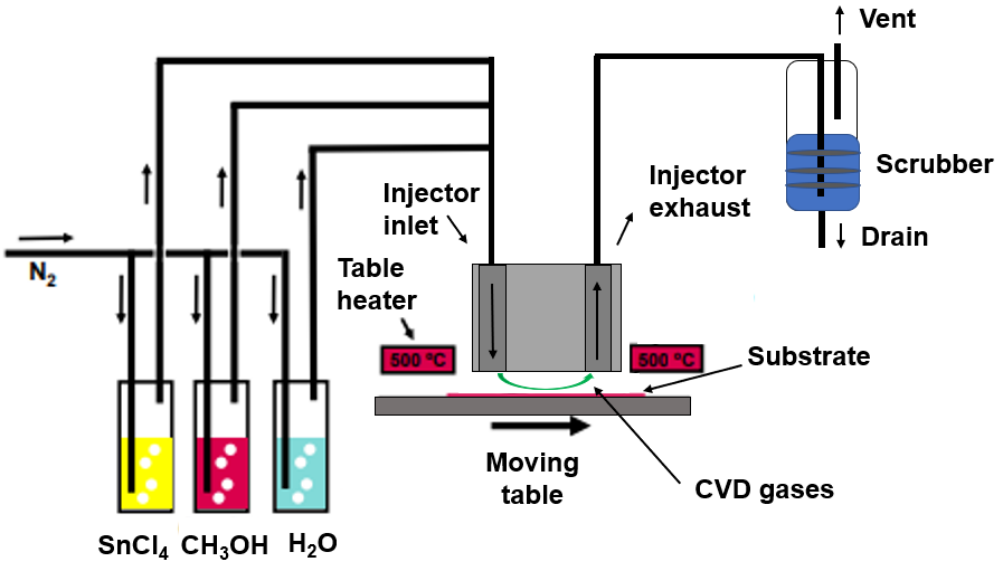

Figure 18: A schematic setup of the lab scale research APCVD tool. Note : The gas system of the LAC is slightly different from the illustration

The goal is to characterize and analyze the material that has been developed in the LAC by adjusting the process parameters and creating a standard operating procedure for both the research instrument and the production machine. The lab-scale APCVD instrument can be found in Figure 19.

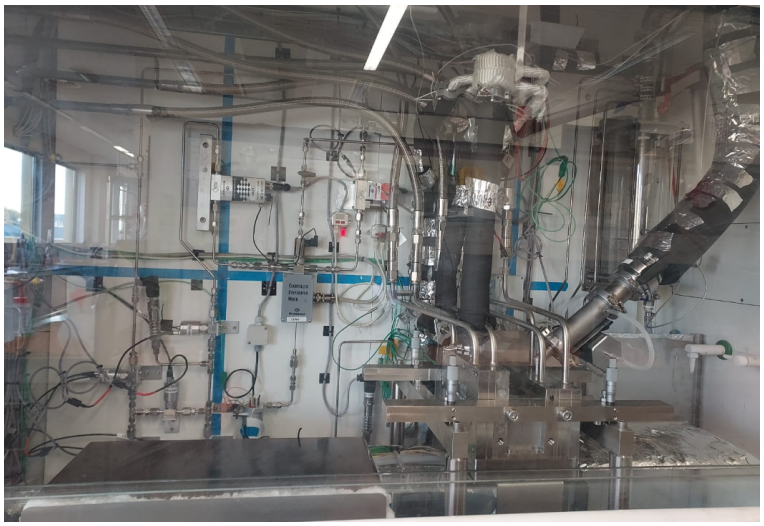

Figure 19: Experimental setup of the lab scale research APCVD tool

3.3.1 Materials

The undoped tin oxide thin films on the aluminium substrate was prepared by atmospheric pressure chemical vapour deposition (APCVD) with tin (IV) chloride ($SnCl_4$) as the precursor. High purity N_2 was used as the carrier gas and H_2O was used as the activator. 0.05% of methanol was mixed with water.

3.3.2 Process

Fifty five grams per hour of TTC is allowed to pass through the liquid flowmeter (LFM1). Nitrogen is used to pump the TTC to the Liquid flow meter. The mass flow controller (MFC1) is set to 5 normalized litres per minute

Deposition parameter	Baseline recipe value for LAC
TTC CEM temperature (°C)	24
N_2 flow (TTC) (ln/min)	5
water, methanol, HF CEM temperature (°C)	60
N_2 flow (water, methanol and HF) (ln/min)	5
Ratio of H_2O/TTC	6.5
Ratio of CH_3OH/TTC	0.0018
Ratio of HF/TTC	0.4
Deposition temperature (°C)	500

Table 2: Deposition parameter and Baseline recipe value for LAC

(ln/min) and nitrogen (carrier gas) is allowed to flow through the mass flow controller. This is mixed with TTC at the controlled evaporator mixer and the mixture is evaporated at 20 °C and is carried by Nitrogen through pipelines heated at 150 °C. The CVD gases enter the injector inlet at 150 °C and are deposited on the aluminum substrate (maintained at 500 °C) mounted on top of the moving table.

The vacuum table which carries the aluminum substrate is movable and thus it allows for multiple depositions across the same substrate. The temperature of the aluminum substrate is kept constant at 500 °C, while the deposition speed is set using LabVIEW software.

The substrate temperature is not measured directly and it can easily deviate from the table temperature since the limited thermal conductivity of the gas makes it difficult for the substrate to assume the table temperature. The substrate temperature is thus set to a higher value than 500 °C.

The excess gases and the desorbed products exit through the exhaust into the scrubber, where they are neutralized. After neutralisation, these gases are vented out and the scrubber fluid is drained.

A huge part of the thesis was focused on construction of the LAC and getting it operational. This involved a lot of challenges and new experiences. This has been detailed in the following sections and explained in detail in the appendix in D.

3.3.3 Details on experiment setup

There are differences in the gas system between the LAC and the production APCVD machine. The LAC has a syringe system for water and methanol that is controlled by Lab-VIEW software. There are three syringe pumps. A dual syringe pump which pumps water and methanol and a single syringe pump to pump HF. This can be seen in Figure 20 This is connected by means of luer tubes and the fluids are mixed just above the inlet of the mini-coriolis flow meter. The use of a syringe pump systems allows for more accurate control of the gases. The system had to be approved for safety and the process settings had to be stabilised first before the introduction of fluorine in the setup.

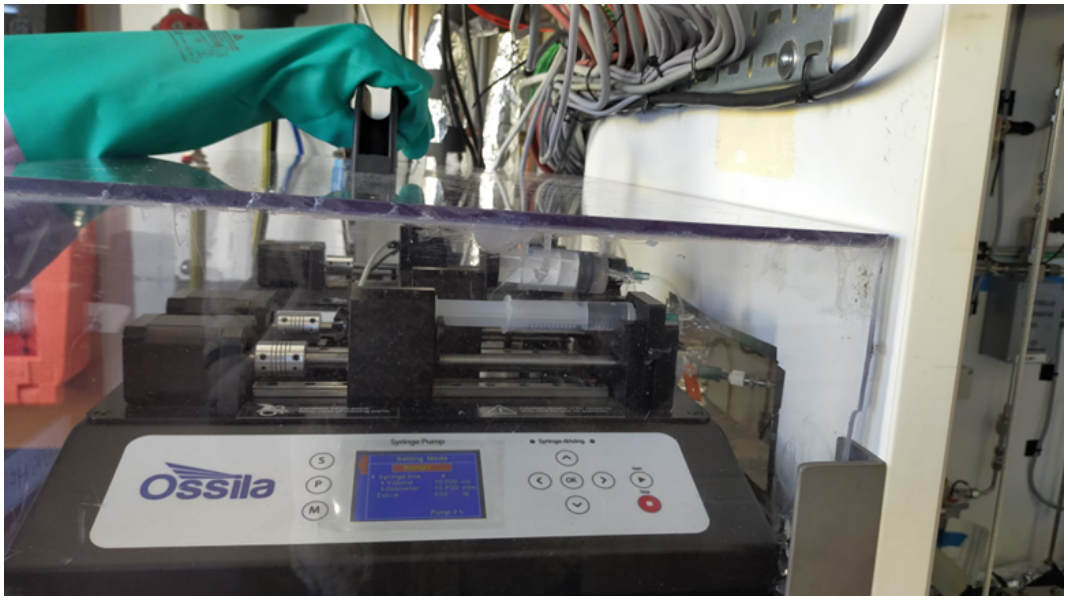

Figure 20: Ossila syringe pump system

3.3.4 Setting up the baseline recipe

The baseline recipe for the LAC was established with half the flow rate of the process and carrier gases as that of the production APCVD machine as the injector of the LAC had half the deposition width as the injector of the production APCVD machine.

The flow rates of the HF, water, and methanol syringes had to be calculated based on the concentration of the gases required for deposition of tin oxide. The recipes for initial deposition using just water and $SnCl_4$ was set up and then the recipes with methanol variations were introduced into the system for subsequent depositions.

The amount of time taken for the pipelines to be filled with the desired concentration of the chemical just before evaporation at the CEM had to be estimated. Based on known parameters listed below and the previously calculated flow rate of the syringes, the time taken for the pipelines to be filled with the desired concentration of the fluid was calculated.

Using known parameters the time required to fill the lines with desired concentration was estimated.

$$\dot{m} = \rho * A * \upsilon \tag{5}$$

$$t = L \div \upsilon \tag{6}$$

where $\dot{m}$ is the mass flow rate, ρ the density of the chemical, A the cross-sectional area of the pipe, υ velocity of fluid through pipe, t the waiting time , L length of piping.

3.3.5 Mounting of the injector : Safety model

The vapor flow pattern between the injector and the substrate layer is one of the most crucial process factors affecting the deposition width. The injector design, injector functioning, and injector positioning all have an impact on the laminar vapor flow, which is powered by forced convection. The out-diffusion of gases through the narrow slits on the top, bottom and side openings of the injector is crucial for safe operation of the tool.

Depending on the distance between the injector and the vacuum table, the gas may enter from or escape to the exterior domain. Figure 21 shows the side opening which is a 1mm high gap between the side of the injector and the vacuum table. Fluid can both flow into or out of the domain, however only perpendicular to the opening. Through this side opening gas may enter from or escape to the exterior domain. The injector-substrate height is

an important factor that influences the flow pattern and it also affects the leak and diffusion rate of the hazardous gases to the atmosphere.

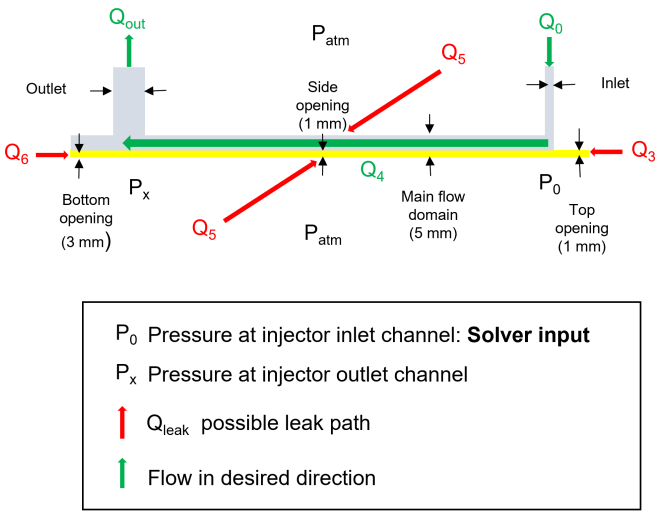

Figure 21: Side view of injector used in the LAC. Figure adapted from [28]

The Peclet number is the ratio between the convective and diffusive transport. It plays an important role in determining whether a particle may cross (due to diffusion) a counter flowing medium. Here the laminar flow is the counter flowing medium (it is the flow of the process gases in the laminar direction, Q_4). To determine the safe mounting distance between the injector and the substrate, the Peclet number was calculated. This is explained in detail in Appendix D

4 Methodology for optical, morphological and electrical measurements

The methodology for sample preparation for the electrical, optical and morphological measurements are discussed in section 4.1. The layer stack for these measurements are detailed in Figure 22. Morphological analysis is performed on the Al-TCO stack while the optical and electrical measurements are performed on the TCO-glue-PEN stack.

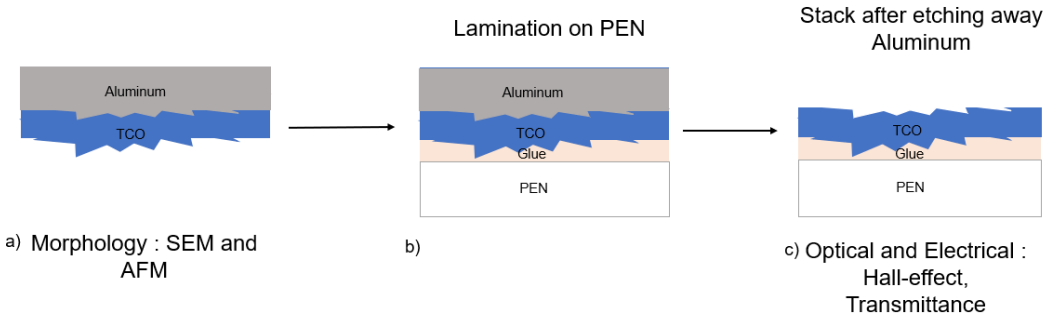

Figure 22: The layer stack for for optical, morphological and electrical measurements

4.1 Sample preparation for optical and electrical measurements

For the measurement of electrical and optical properties, the FTO was transferred from aluminum (100 micron substrate) to polyethylene napthalate (PEN), 125 microns. Every sample (2 at a time) was laminated to PEN film using a heat curing 2-component epoxy resin as adhesive (glue). The samples were heated to 100 °C in a hydraulic press in 13-14 minutes and after a hold time of 5 minutes at 110 °C, the press was cooled down to RT in about five minutes. Removal of the aluminum temporary substrate (one sample at a time) was done by a two-step etching process in a beaker containing a mixture of of 25 wt% of (NaOH 1800 ml) , 0.5g of a resin and 5g of sodium gluconate at a controlled temperature of 70 °C.

The first 80 microns of Al was removed in the first 8 minutes and then post-bake was done at 170 °C in the oven (to release the compressive stress of TCO on the aluminum foil so that it transfers to PEN without delamination) The last 20 microns are etched away in another 2 minutes.

4.2 Optical measurements

Optical transmission was measured on stack c) in Figure 22 using a Varian Cary 5 UV-VIS spectrophotometer. Note that a detector change around 900 nm leads to some signal distortion in the measurement.

To compensate for reflection and transmission losses outside the TCO layers, the sample transmittance was compared to that of a reference stack consisting of PEN. Because we have corrected for reflection losses, the transmittance T plus absorptance A must add upto 1, where absorptance A is given by Lambert beer's law [29],

$$A = 1 - e^{-\alpha d} \tag{7}$$

where α is the absorption coefficient and d is the layer thickness.

$$T + A = 1 \tag{8}$$

$$\alpha = -ln(T)/d \tag{9}$$

4.3 Electrical measurements

The carrier electron density (n_e), resistivity (ρ) and the Hall mobility (μ) were measured on stack c) in Figure 22 using a HMS5000 (by Ecopia 21) Hall measurement setup in standard four point Van der Pauw geometry, with a

measuring current of 10 mA and a magnetic field of 0.55 Tesla for a sample size of 10x10 mm^2.

4.4 Morphology investigation

First the TCO was visually inspected to make sure it was free from visual defects such as wrinkles, milkiness, scratches, splatters and non-homogeneous deposition. The morphology (FTO on Al) was then analysed under the AFM (for surface roughness) and the SEM (for grain inspection).

High resolution SEM images were made by the SEM Hitachi regulus 8430 on samples of FTO on Al. The grain size is calculated by imageJ software. Twenty measurements are made on two to three samples and they are averaged to find the average top surface grain size.

AFM scans were made with the Bruker AFM probe on a 4*4 μm and a 16*16 μm scan area. These scans were then analysed with Gwyddion SPM analysis suite, software version 2.62. The background is corrected using the "align rows" option using a polynomial function of degree two in the horizontal and vertical direction, so that the background and the peaks are differentiated sufficiently by contrast. The minimum data in the scale bar is then shifted to zero using the option under data process. Then the statistical quantities such as average surface roughness, RMS roughness, max Peak-Valley (P-V) height and Kurtosis are derived from the image.

The finish of the optical surface is represented as RMS roughness. It represents the standard deviation of the profile heights and is used in the computation of skew. It is more sensitive than the average roughness [30].

Skewness is a measure of the symmetry of the height distribution. It gives an indication of the amount of hills or valleys on the surface [30].

The distribution of the spikes above and below the mean line plane is measured by Kurtosis. For Kurtosis greater than 3, the surface is spiky. For Kurtosis lesser than 3, the surface is bumpy. For Kurtosis equal to 3, the surface is randomly textured. Figure 23 contains a representation of the Kurtosis and Skewness [30].

These features can let us know the overall scattering ability of the film and could also indicate if shunts are possible [30].

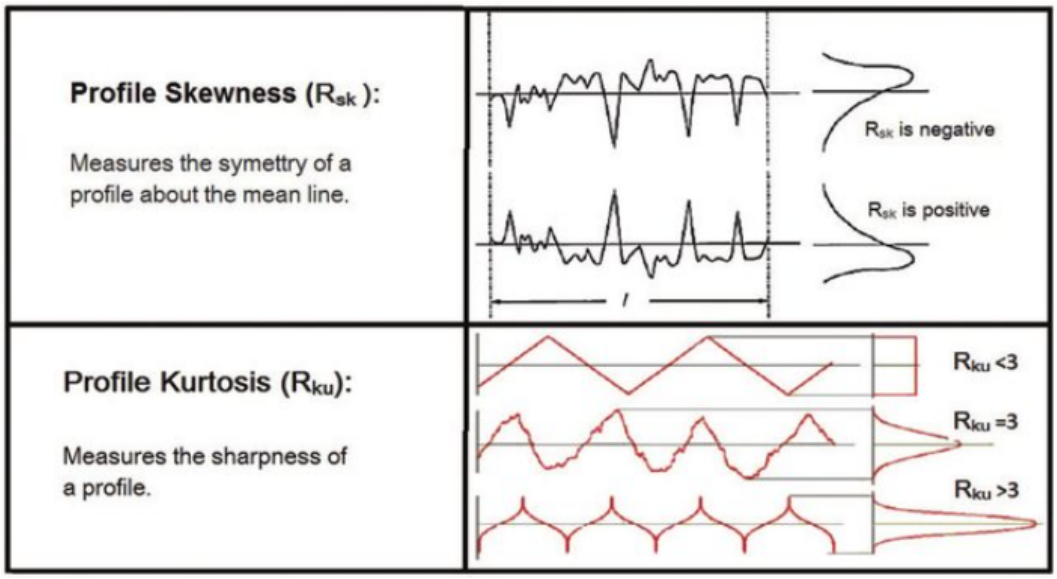

Figure 23: Representation of Kurtosis and skewness. This image has been adapted from [30].

4.5 Leak test

At HyET there is a quick method to verify the quality of the deposited TCO using a leak test in the lab. A beaker containing 1800 ml of a solution of 25 wt% of NaOH with a controlled temperature of 70 °C is prepared along with a resin and sodium gluconate. Then the etch resistance of the FTO is tested by pasting the aluminum side to a teflon plate and exposing the side with deposited TCO to the etching bath. The presence of defects and pin holes can be detected by bubble formation on the TCO as the NaOH seeps in through cracks or pin holes in the FTO and etches the aluminum. The time taken to notice the first bubbles is noted as the leak time. This was done on different parts of the TCO across the width of deposition to determine the presence of defects in the deposited TCO.

4.6 Background details regarding some measurements and units

In our experiments, the layer thickness is calculated from the interference fringes that are measured in the sample's reflectivity as a function of wavelength. The samples have been always cut from the central part of the foil. The effective extraction width varies with the extraction level: higher extraction giving narrow effective width, lower extraction giving larger width. The layer thickness in the central part of the deposition is virtually independent of the extraction level, which is an attractive feature of the injector geometry.

In the following sections the experimental parameters will be discussed in terms of molar ratios. Since TTC is the Sn precursor all the molar ratios are calculated with respect to TTC. For example HF/TTC is the ratio of the molar flow rate of HF expressed in mol/min to the molar flow rate of TTC expressed in mol/min. Similarly water/TTC and methanol/TTC are estimated. Throughout the experiments the molar flow rate of the oxidiser (water), additive (methanol) and dopant (HF) gas will be varied and the variations will be expressed in terms of molar ratio.

The carrier gas is represented in ln per minute which expands to normalized litres per minute. The standard reference in this case is selected to be gas at a temperature of 0 °C and a pressure of 1013.25 hPa(a). This is a standard term used in the MFC supplied by Bronkhorst.

In the following sections, the term web speed will be used quite often. Web speed is the speed with which the main drum moves under the injector and hence it refers to the webspeed.

5 Results and discussions on the production APCVD machine : Effect of gas flow and web speed variations

In this section, the results and conclusions of the experiments on the production APCVD machine will be discussed. First, the experiment parameters will be tabulated followed by a brief explanation of the followed methodology after which we will conclude the results of the experiments.

In the following sections the experimental parameters will be discussed in terms of molar ratios. Since TTC is the precursor all the molar ratios are calculated with respect to TTC. For example HF/TTC is the mol/min of HF to the mol/min of TTC in the experiments. Similarly water/TTC and methanol/TTC are estimated. Throughout the experiments the molar flow rate of the oxidiser (water), additive (methanol) and dopant (HF) gas will be varied and the variations will be expressed in terms of molar ratio.

5.1 Effect of gas flow and web speed variations

One of the most challenging steps in the fabrication of the thin films in HyET Solar is the APCVD process for the deposition on FTO. A faster webspeed and gas flow rate can result in faster roll-to-roll production process, which directly translates to lower production costs and higher throughput. The time it takes to produce modules will be shortened by an increase in webspeed and gas flow rate while aiming to preserve opto-electrical performance.

This section aims at answering the research question on how a change in deposition conditions (web speed, flow rate of the gases) affect the opto-electrical and morphological properties of the TCO.

This series of experiments was carried out by increasing the process gas flow rates and scaling up the webspeed linearly while trying to keep the thickness variation minimal compared to the baseline recipe at 0.6 m/min which yields a film thickness of 740 nm. This can be visualized in Figure 24. The rest of the experimental values such as temperatures and pressures were kept constant and only the flow rate of the process gases and the webspeed were changed. Flow rate of the carrier gas N_2, was also kept constant at 20 ln/min. The experimental conditions and details of speed variations can be found in Table 3. The molar ratio of water/TTC, HF/TTC and MeOH/TTC has been preserved as previously used in the APCVD machine while the web speeds and the process gas flow rates have been increased linearly. Recipe 1x corresponds to the baseline recipe process gas flow rate in g/hr. 1.1x, 1.3x and 1.5x are ten, thirty and fifty percent increase in the process gas flow rate (in g/hr). Here web speed indicates the webspeed.

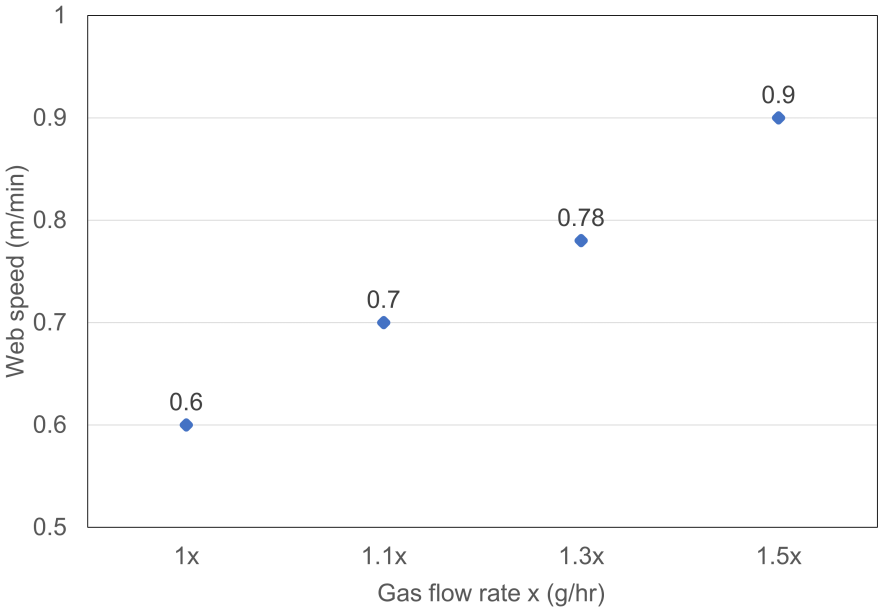

Figure 24: Web speed as a function of gas flow rates

Experiment parameter	constant recipe values
Substrate temperature (°C)	500
Exhaust pressure (Pa)	20
TTC CEM temperature (°C)	150
HF evaporation temperature (°C)	70
N_2 flow (TTC & HF) (ln/min)	10
Water/ methanol CEM temperature (°C)	70
N_2 flow (Water & methanol) (ln/min)	10
Baseline ratio of H_2O/TTC	6.5
Baseline ratio of CH_3OH/TTC	0.0018
Baseline ratio of HF/TTC	0.4
Experiment parameter	**varying recipe values**
Baseline webspeed (1x) (m/min)	0.6
webspeed (1.1x) (m/min)	0.7
webspeed (1.3x) (m/min)	0.78
webspeed (1.5x) (m/min)	0.9

Table 3: Experimental parameters for effect of gas flow and web speed variations

The resulting films were analysed for optical, morphological and electrical properties and the observed properties are discussed in detail in the following sections.

5.1.1 Optical properties

The transmittance was measured on the TCO-PEN stack after gluing and laminating the TCO-Al stack to PEN and etching away the Al. This is detailed in section 4.1. The transmittance is plotted in Figure 25. It is observed that the transmittance is similar for all webspeeds and gas flow rates: the average transmittance from 400-1000 nm was estimated to be around 80 - 84 % for all samples. The transmittance is also influenced by the thickness of the film deposited, hence to visualize the absorption of the film, the absorption coefficient is plotted in Figure 26. The optical thickness was estimated along the width of the foil and averaged. This is tabulated in Table 4.

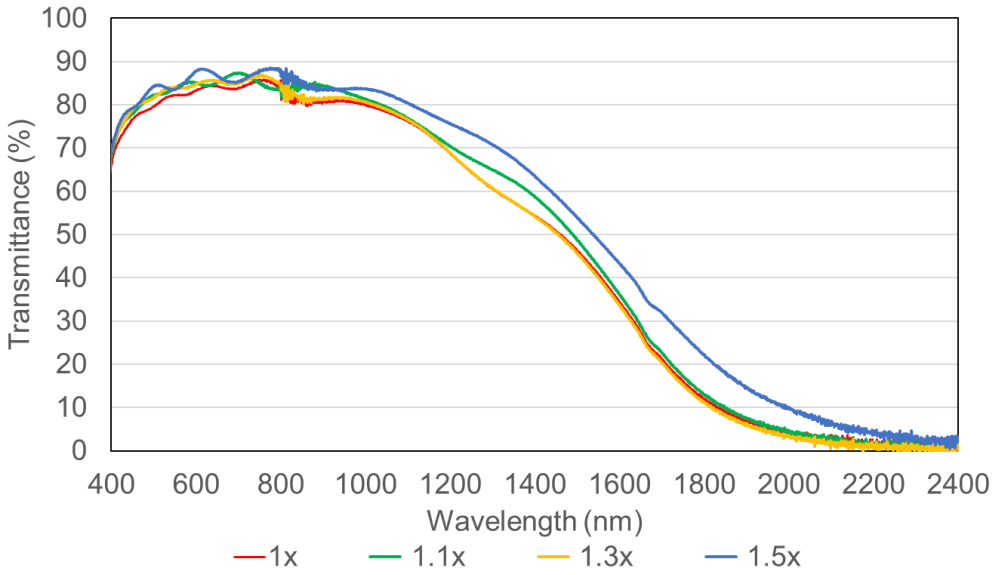

Figure 25: The measured transmittance spectrum for different webspeeds and gas flow rates

Three series of experiments were performed for the variation of webspeed and gas flow rates to gain statistical evidence, the first experiment is tabulated below in Table 4.

Observed material properties of gas flow rates	1x	1.1x	1.3x	1.5x
Thickness of deposited FTO (nm)	804.9	777.5	775	747.6
Average transmittance between 400-1000 (%)	81.3	83.23	82.89	84.53
Average surface grain size (nm)	374	375	382	370.3
Standard deviation in average surface grain size (nm)	115	91	93	52
RMS roughness (16x16 μm) (nm)	29.39	24.43	23.15	21.22
Max P-V (16x16 μm) (nm)	276.2	265.5	240	183.9
Skewness (16x16 μm)	0.2504	0.09988	0.131	0.2476
Kurtosis (16x16 μm)	3.2705	3.109	2.8806	3.0016
Mean free path length of electron (λ_{mfp}) (nm)	12.88	12.46	14.1	12.64

Table 4: Measured values for different webspeed and gas flow rates

From the transmission and layer thickness experiments, the absorption coefficient can be calculated as

$$\alpha = -ln(T)/d \tag{10}$$

Where T is the transmittance and d is the layer thickness. The absorption coefficient as a function of wavelength is plotted in Figure 26. The relation between the absorption spectrum and the free charge carrier density is explained in section 5.1.3.

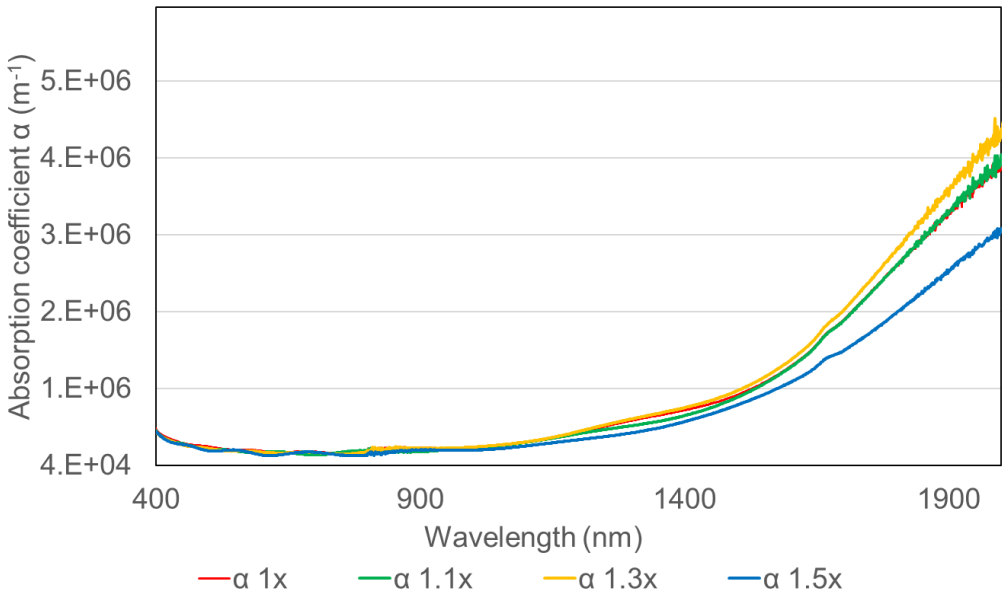

Figure 26: The measured optical absorption coefficient for different webspeed and gas flow rates

The electrical sensitivity to optical measurements is an interesting feature of the TCO. There are fringes present in the optical spectra between 400 and 1000 nm due to multiple internal reflections within the film which can be visualized in Figure 25. Assuming a very small absorption in this region which can be seen in Figure 26, fringes depend on refractive indices of the substrate and film and thickness of the coating. The region of interest is considered from 400 nm as the signal at lower wavelengths is weak due to absorption by the glue.

When the gas flow rates are ramped up to 1.5x, we see an extension of the transmission spectra to the near IR region. From the rise in absorption due to free charge carriers in the near IR region, certain deductions regarding lower carrier density can be drawn which are in agreement with the electrical properties of the film plotted in in Figure 30. This will be discussed in detail in the section 5.1.3.

5.1.2 Morphology

SEM and AFM were performed to analyze the morphology of the deposited film. The top-SEM analysis was done at at an acceleration voltage of 5.0 kV at 25.0k magnification. The scale for all the the images are 2 microns. Figure 27 revealed similar surface morphology for all webspeed and gas flow rates. When the observed surface morphology and electrical properties are analysed together they show an agreement with the electrical values. This is detailed in the following section 5.1.3. The surface grain size estimated from the SEM images below in Figures 27a, 27b, 27c and 27d are listed in Table 4. The average top grain size estimated by means of imageJ software yields similar results for all four samples. The average grain size was between (370-382) nm further confirming the visual observation that the surface morphology does not change for different flow rates. The variation in the surface grain size is due to variation in the thickness of the deposited film. The most commonly observed crystallite shape was pyramidal shape with a pointed peak or with a dimple on top.

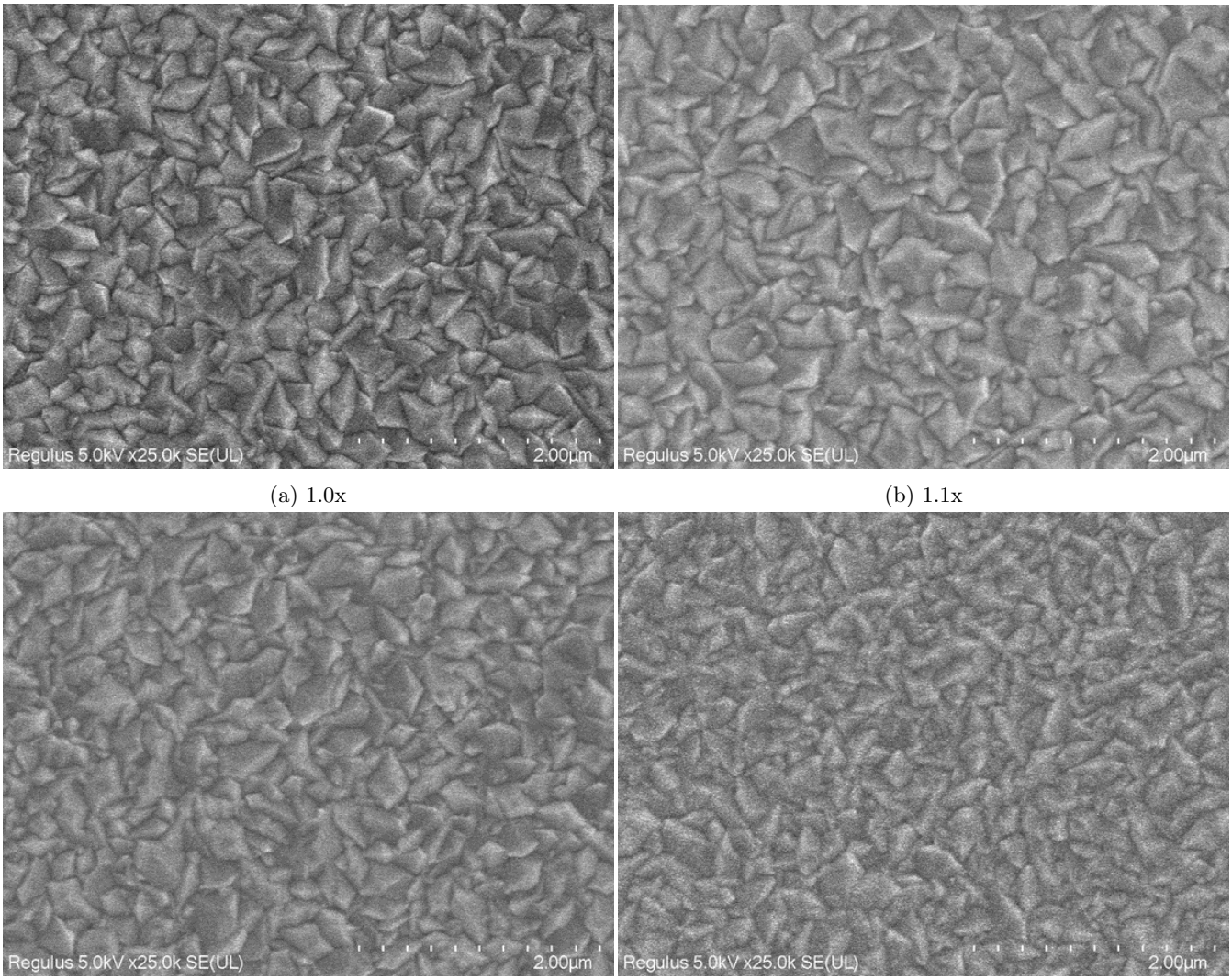

(a) 1.0x

(b) 1.1x

(c) 1.3x

(d) 1.5x

Figure 27: Top - view SEM of different webspeed and gas flow rates

The RMS roughness is highest for the thickest sample and reduces with decreasing thickness. These experiments were performed on Al substrate with texturing (by pre-treatment in an alkaline bath). Texturing is beyond the scope of this thesis and has not been treated in the report. It is expected that the sample with the highest roughness would have the best light scattering. The RMS roughness seems very sensitive to even the slightest variation in thickness (the thickness influences the size of the grain). This relation between RMS roughness and the thickness of the FTO can be visualized in Figure 28. The AFM image of a 16x16 μm sample for each of the webspeed and gas flow rates can be found in Figure 29. The observed morphology is similar but the roughness is different as it is very sensitive to even slight variations in thickness. Hence it is highly likely that the roughness would also be the same for FTO of the same thickness. The surface roughness estimated using AFM is a representation of the roughness observed in a 16*16 μm sample. Probing a larger area with the AFM is required to gather statistical evidence of the surface roughness.

A reduction of the TCO deposition time to achieve baseline thickness of 740 nm while moving to higher webspeed and gas flow rates should be possible without impairing the module output parameters like open circuit voltage, short circuit current, fill factor or efficiency. This is a crucial factor to decrease production time or production costs. To ensure that moving to higher gas flow rates and webspeed does not affect the module performance, a lab-scale device needs to be built on the deposited TCO and it needs to be tested. Due to the limited time, this has not been done as a part of this thesis.

AFM was performed only on one set of samples. The change in the webspeed and gas flow rate has a strong influence on the surface roughness and TCO layer thickness. To achieve the same thickness, the web speed should be adjusted accordingly. Samples of similar thickness should be observed for roughness under the AFM to confirm that the roughness would remain similar for higher webspeed and gas flow rates.

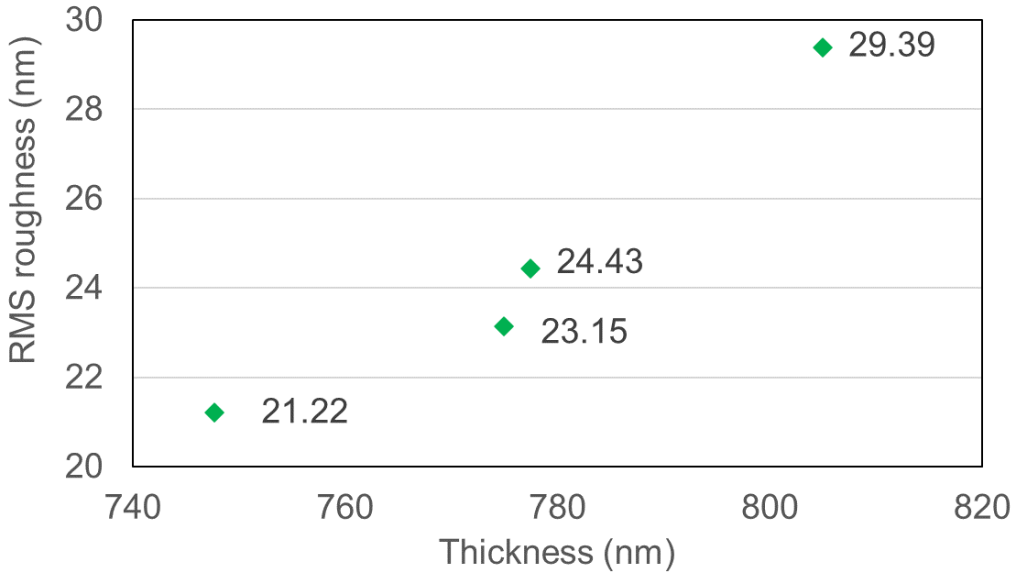

Figure 28: Increase in RMS roughness as a function of thickness

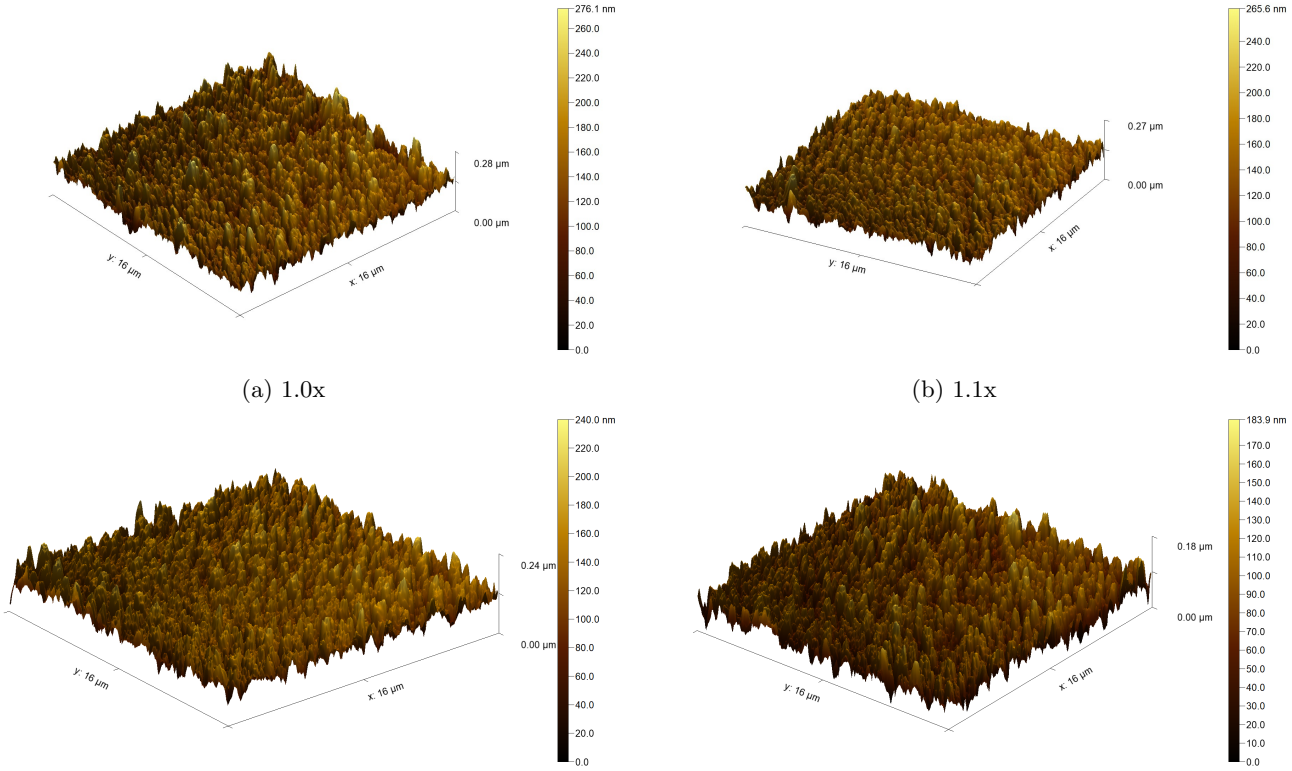

(a) 1.0x

(b) 1.1x

(c) 1.3x

(d) 1.5x

Figure 29: AFM images of different webspeed and gas flow rates on a 16* 16 μm sample

5.1.3 Electrical properties

Figure 30 shows the variation of electrical properties with an increase in gas flow rate and webspeed. The error bars in the graph indicates the standard deviation of the measurement. The charge carrier density remains similar for all flow rates except when the process gas flow rate is ramped up to 1.5x, there is a very slight reduction in charge carrier density. The resistivity decreases with increase in charge carrier concentration and rises up at 1.5x when there is a slight decrease in charge carrier density. It is interesting to note that the morphological properties are in agreement with the electrical properties. The correlation between the increase in free charge carrier density can be visualized here as the absorption in the near IR region seems to increase with an increase in charge carrier density in this region in Figure 26. The mobility values are similar for all the gas flow rates. The average top grain size estimated by means of SEM shows a linear relationship with mobility. The mobility seems to increase with increasing grain size. The highest mobility is observed for the sample with the largest grain size. However, for all the samples there is no large variation in any of the observed opto-electrical properties, as the ratio of the gases are preserved and only the webspeed and gas flow rate is enhanced.

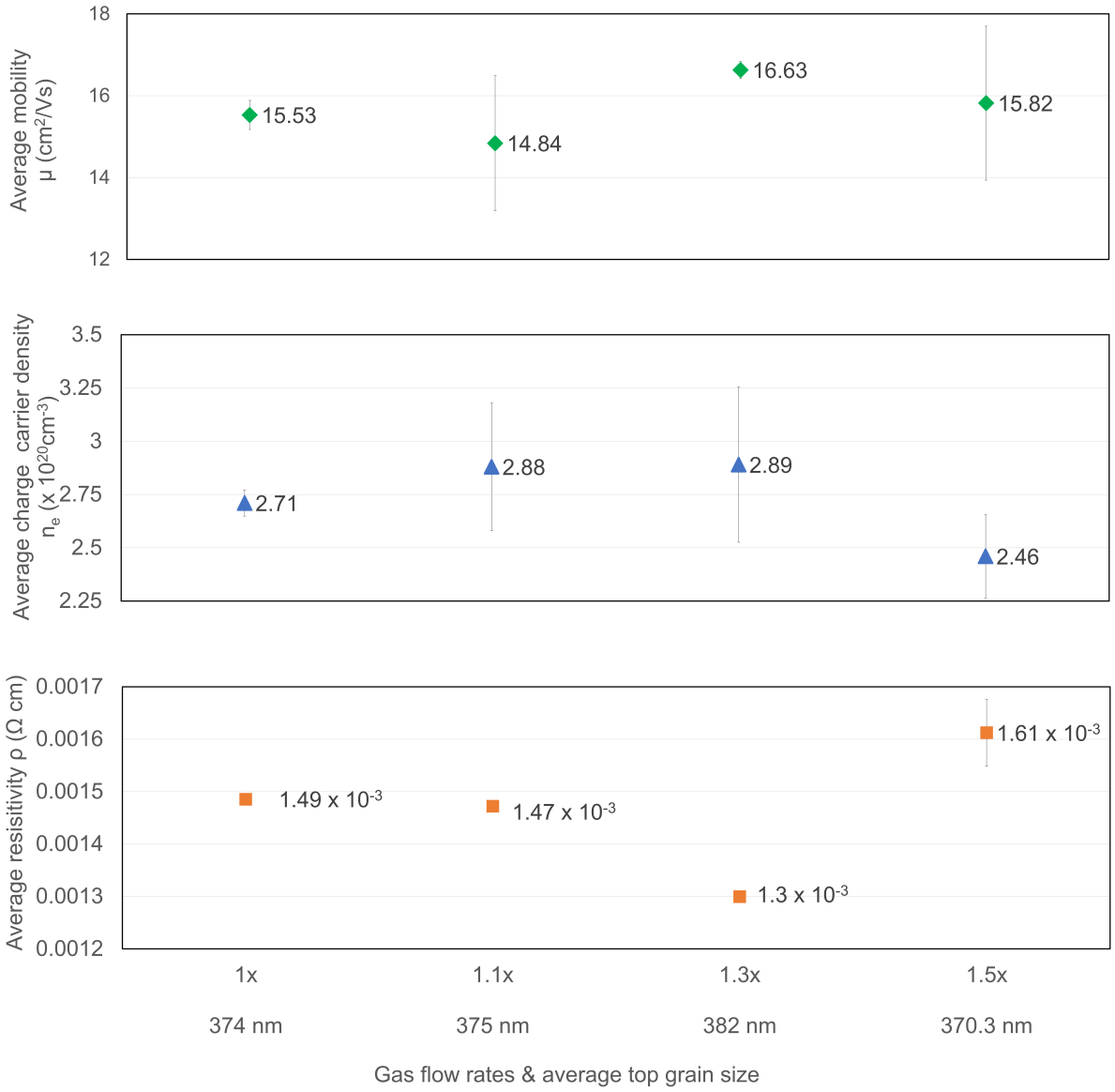

Figure 30: Mobility, charge carrier concentration, and resistivity as a function of average surface grain size for different gas flow rates

The total mobility is affected by grain boundary scattering only if the grain size is comparable to the mean free path of the charge carriers (L$\sim\lambda_{mfp}$). The mean free path can be calculated using a highly degenerate electron gas model [31] given by

$$\lambda_{mfp} = (3\pi^2)^{1/3}(h\mu/e)n^{1/3} \tag{11}$$

From Table 4, it can be observed that the sample with larger grain size has a longer λ_{mfp}, but since the mean free path of the carriers is much smaller than the observed grain size of the films for both the cases, grain boundary scattering is not the dominant mechanism. Hence the scattering within the grains (due to neutral or ionized impurities) could be the cause of low mobility. The ionized impurity plays a major role in scattering for these carrier densities and lowers the mobility of the carriers.

On scaling up gas flow rates and webspeed, a relation can be seen from the estimated grain size, measured optical, and electrical properties. The observed morphological, optical, and electrical properties on moving to higher web-

speed and gas flow rates are comparable to each other which builds confidence in moving to higher webspeed and gas flow rates to increase the throughput, without compromissing on the quality of the TCO.

After repeating three more sets of experiments with varying webspeed and gas flow rates, to gain statistical evidence for the comparable properties, this recipe has been made the new baseline recipe for the TCO deposition process at HyET Solar.

XRD analysis of the new baseline material (1.5x at 0.9 m/min) can be found in Appendix B.

6 Results and discussions on the production APCVD machine : Recipe optimization

In order to investigate the possibility to improve opto-electrical properties of the deposited film, molar ratio of the process gases were varied and their effect on the opto-electrical and morphological properties of the deposited FTO was analyzed.

6.1 Effect of HF

In the literature review, it was discussed that increasing the level of F-doping influences the conductivity and impacts the overall performance of the solar cell. The aim of this this experiment is to investigate the effect of HF in the growth process, in terms of morphology, optical and electrical properties. The HF/TTC ratio was varied from 0.2 to 0.5 while the other experimental parameters were held constant with an aim to find the optimum level of F-doping.

In this experiment, FTO was deposited by variation of the HF settings. The deposition temperature and speed were maintained at 500 °C and 0.6 m/min while the HF flow controller settings were changed. The water/methanol, TTC flow controller and the carrier gas flow settings were kept constant throughout the experiment. During this experiment, there was a problem with extraction and as a result the deposited sample was non-homogeneous; details of the malfunction are mentioned in the following sections.

6.1.1 Optical properties

The HF/TTC range over which the depositions were carried out was 0.2-0.5. Transmittance measurements were carried out on the coating. As shown in Figure 31. Since the transmittance is also influenced by the thickness of the film deposited, hence to visualize the absorption of the film, the absorption coefficient is plotted in Figure 32. The optical thickness was estimated along the width of the foil and averaged. This is tabulated in Table 5.

From the transmission and layer thickness experiments, the absorption coefficient can be calculated as

$$\alpha = -ln(T)/d \tag{12}$$

Where T is the transmittance and d is the layer thickness. The absorption coefficient as a function of wavelength is plotted in Figure 32. The relation between the absorption spectrum and the free charge carrier density is explained in section 6.1.3.

It can be seen that with increase in HF concentration there is a slight drop in transmittance in the near IR region, however this is very subtle. This can be attributed to the increased carrier density due to increasing HF dose. The electrical properties observed are plotted in Figure 34. A free carrier density shifts the edge of the IR tail of the transmission window towards the visible range, increasing the absorption in the TCO. This can be observed in Figure 32 in which the absorption coefficient seems to increase with doping concentration. The absorption coefficient of the sample with HF/TTC = 0.4 seems to be the lowest despite possibly higher carrier density. The measurement was repeated but yielded the same results. The slight decrease in absorption coefficient in IR region despite increasing carrier density could be an effect of fluctuation of the mass flow controller of the HF setup, leading to variation in carrier density across the sample.

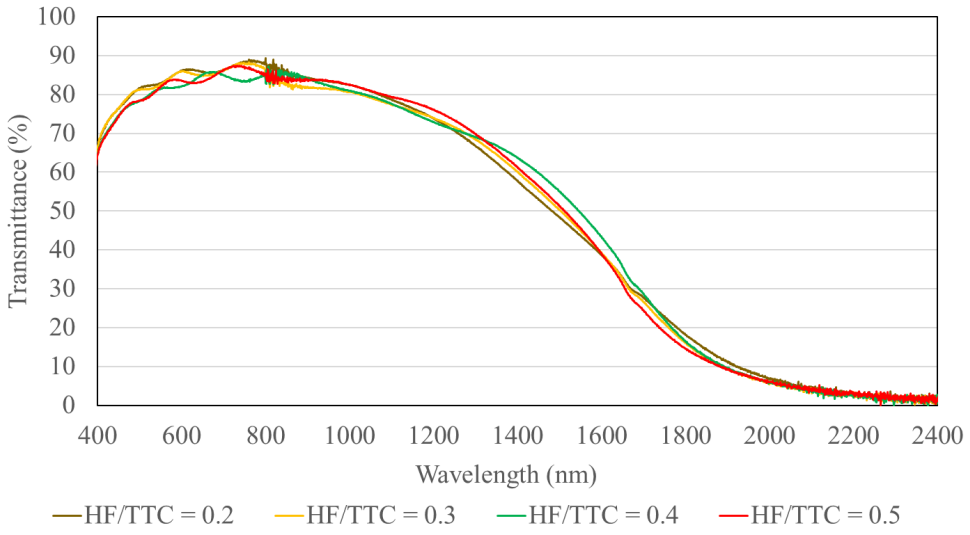

Figure 31: Transmittance of FTO deposited on Al foil for different HF/TTC ratios used in the APCVD process

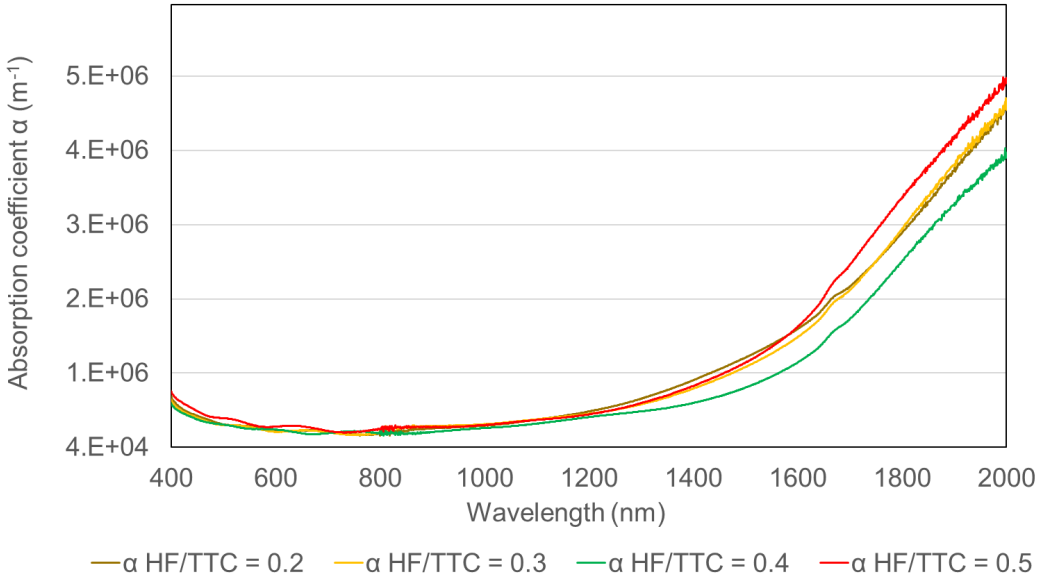

Figure 32: Optical absorption coefficient of FTO deposited on Al foil for different HF/TTC ratios used in the APCVD process

6.1.2 Morphology

The images from the SEM analysis can be found in Figure 33. The effect of increasing dopant concentration on grain size can be viewed in Table 5.

Parameter & measured values of HF/TTC	0.2	0.3	0.4	0.5
Web speed (m/min)	0.6	0.6	0.6	0.6
Thickness of coating (nm)	635	613	694	565
Average surface grain size (nm)	363.2	325.9	487.84	331.3
Standard deviation in average surface grain size (nm)	64	62	144.95	78
Average total transmittance between 400-1000 (%)	83.7	82.89	81.85	81.89
mean free path length of electron (λ_{mfp}) (nm)	6.98	6.82	11.79	8.17

Table 5: Measured values of TCO for HF/TTC variations

It is observed that there is a definite change in the size of the grains as HF concentration is increased but since there is a variation in thickness of the samples they cannot be compared directly. The grain size generally increases with increase in thickness. However, when HF/TTC = 0.5, despite reduced thickness the grain size is larger than when HF/TTC = 0.3. This is in agreement with literature, that there is a slight increase in grain size with HF addition [12]. In [25] it has been observed that HF addition stabilised the morphology. The grains seem to get sharper with addition of HF. This can be seen from the SEM analysis of the samples deposited without HF by the LAC in Section 7 where samples without HF are deposited and they lack the sharpness in their features. The highest grain size is seen when HF/TTC is 0.4, this also matches with the electrical properties which can be seen in section 6.1.3. The grain size remains similar in size except for when HF/TTC = 0.4. The grain remains pyramidal and a change in grain size is observed on varying the dopant concentration. It has to be noted that the sample HF/TTC = 0.4 was the first sample to be deposited with clean injectors. After this a series of experiments with varying gas flow rates were performed and then finally HF series was varied at HF/TTC = 0.2, 0.3 and 0.5. During the start of the experiment on HF series variation, there was a problem with extraction and HF flow had to be stopped and then restored. Subsequently, stripes and splatters were noticed on the deposited TCO, so the deposition was not homogeneous. On taking the injector out, it was noticed that the injector was clogged, which was one of the primary factors affecting the deposition. Pictures of striping, splattering on the deposited foil and the clogged injector can be found in Appendix E.

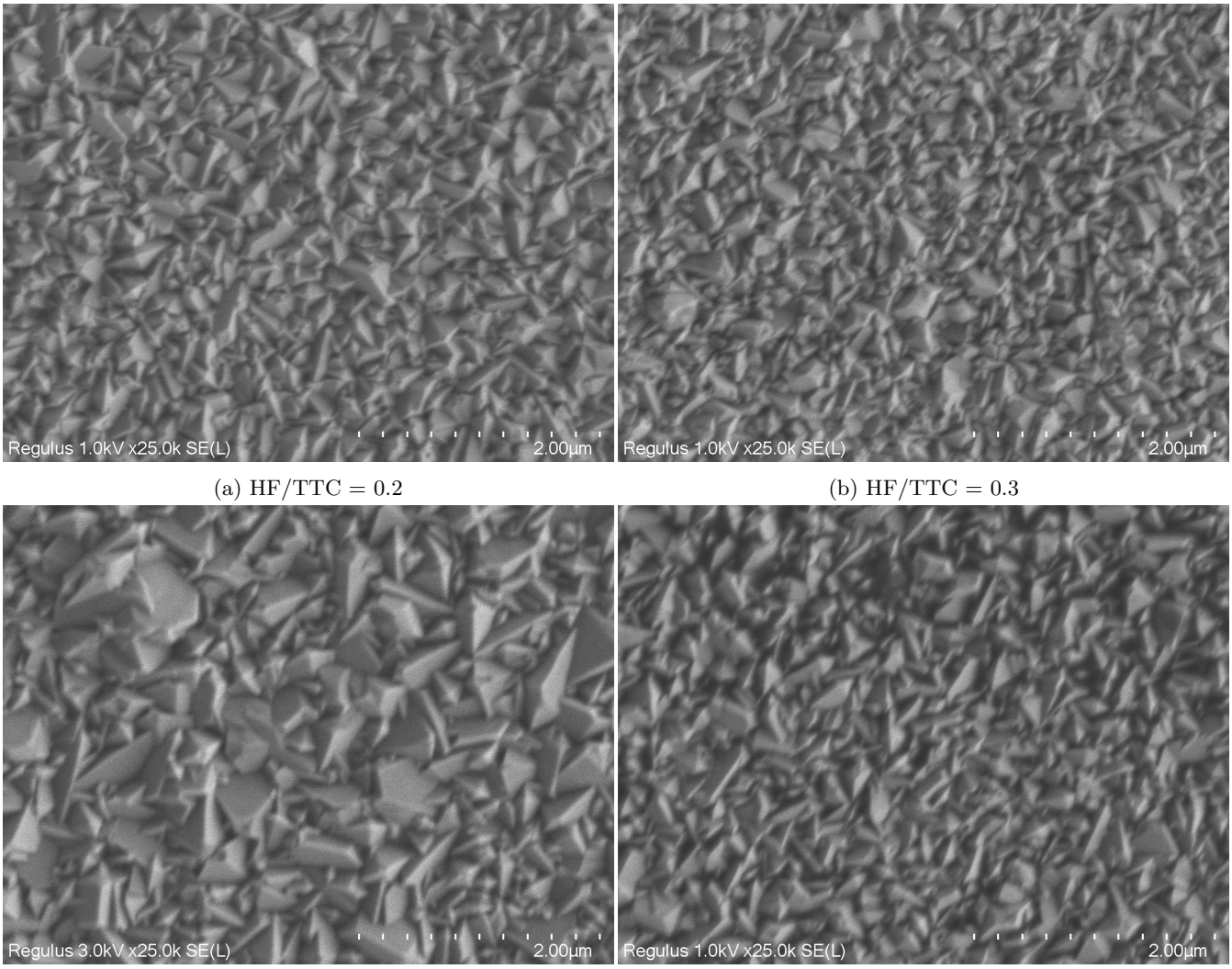

(a) HF/TTC = 0.2

(b) HF/TTC = 0.3

(c) HF/TTC = 0.4

(d) HF/TTC = 0.5

Figure 33: FTO deposited on Al foil with different HF/TTC ratios in the gas mixture during the APCVD process.

6.1.3 Electrical properties

The electrical properties observed are plotted in Figure 34. As HF concentration increases there is a slight rise in charge carrier concentration and this is accompanied by decrease in resistivity. This rise in charge carrier concentration with increase in HF dosage also concurs with a drop in transmittance due to the peak in free carrier absorption.

Increasing HF/TTC beyond 0.4 brings a reduction in mobility as some of the fluorine atoms act as ionized scattering centers against mobile electrons. The other fluorine atoms are accumulated at the grain boundaries, causing grain boundary scattering [4].

As mentioned earlier, the scatter in the Hall-effect measurement values could be due to the inhomogeneous deposition due to the malfunction of the exhaust. Another reason could be poor transfer of TCO from the temporary Al substrate to PEN which could result in delamination at TCO-PEN interface or cracking of the crystals which affects the electrical properties and subsequently the Hall-effect measurements. In order to avoid the effects due to poor transfer, the transfer of the TCO from aluminum to PEN was repeated but the measurement yielded similar results, confirming that the injector clogging affected the film quality. This can be visualized in Appendix E.

The trend in the data in this experiment despite the poor quality of material deposited seems to indicate that HF/TTC = 0.4 is the optimum level of dopant beyond or below which there is a degradation of electrical and optical properties.

Beyond critical concentration a sharp increase in charge carrier density is observed, this reduces resistivity. However beyond this concentration as the excess fluorine are no longer able to replace oxygen ions, they are expelled to segregate at grain boundaries and hence there is no drop in resistivity.

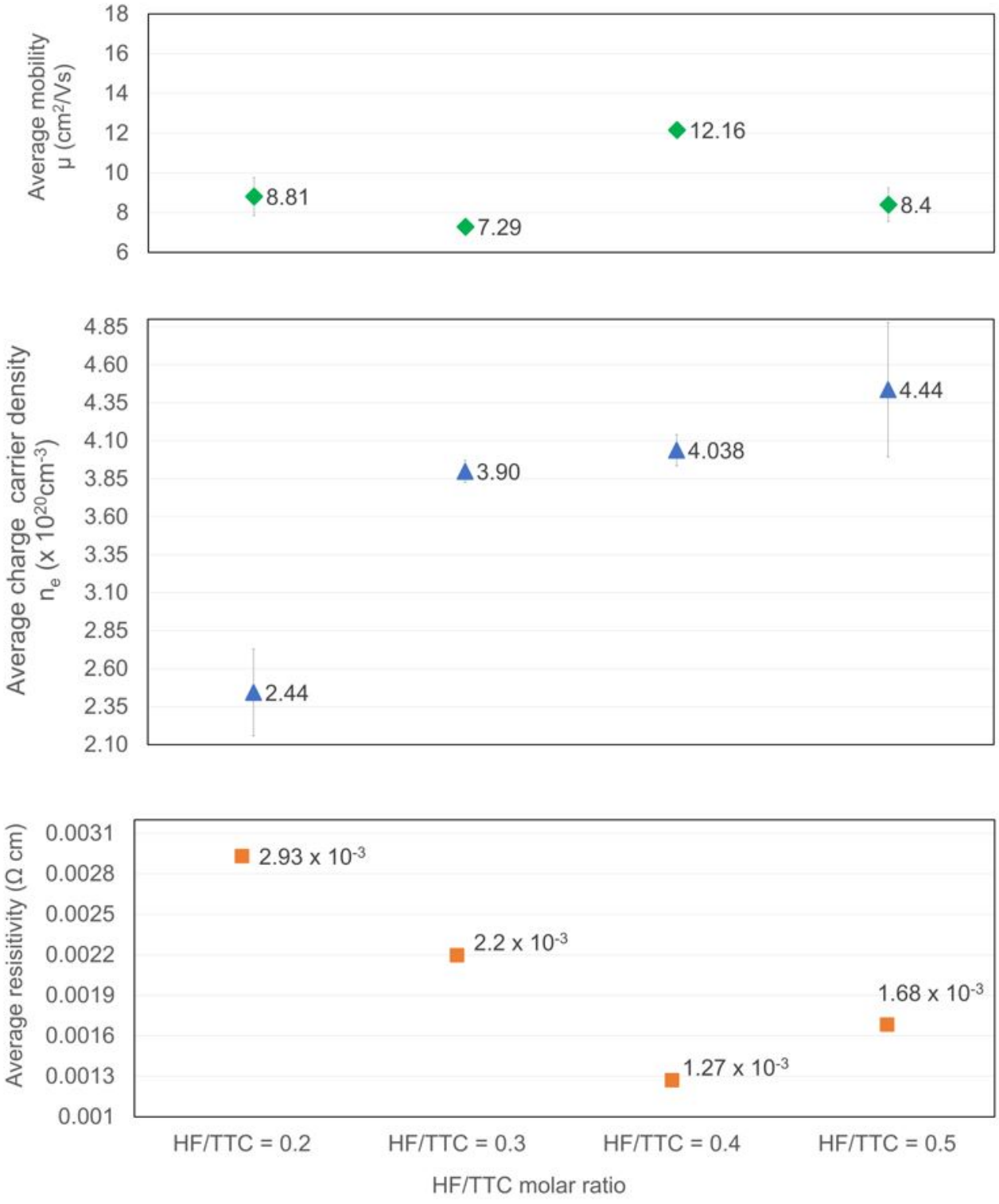

Figure 34: Mobility, charge carrier concentration and resistivity as a function of different HF concentrations

6.2 Experiments for recipe optimization - varying HF, water and methanol

The previous series of experiments on HF showed a trend in the values that suggested that HF/TTC = 0.4 is the optimum dopant limit. But due to clogging of the injector, the material properties were affected. Hence in these set

of experiments, the HF/TTC molar ratio is varied again to analyze changes in the properties. Along with HF/TTC variation, water/TTC molar ratio is also varied over a range of values indicated in Table 6. From initial literature review it was studied that change in water concentration affected the growth rate and morphology of the deposited FTO. Hence to analyze these changes, this experiment was formulated.

Due to the premixing of methanol with water used in the production APCVD machine at HyET, there is little possibility of variation in water concentration independent of methanol. Hence change in water concentration resulted in minor changes in methanol concentration.

Recipe settings	S1	S2	S3	S4
HF/TTC molar ratio	0.3	0.4	0.5	0.6
water/TTC molar ratio	4.8	6.5	8.1	9.8
methanol/TTC molar ratio	0.0013	0.0018	0.0022	0.0027
Web speed (m/min)	0.6	0.6	0.75	0.9
Material properties	S1	S2	S3	S4
Thickness of coating (nm)	581	718	907	747
Average surface grain size (nm)	251.5	271.9	306.6	289.6
Standard deviation in average surface grain size (nm)	41.4	70	90.7	74.9
Average total transmittance between 400-1000 nm (%)	85.59	82.89	83.3	-

Table 6: Measured values of gas flow variations

6.2.1 Optical properties

Transmittance measurements were carried out on the coating. As shown in Figure 35, it can be seen that with increase in HF (and water) concentration there is a slight drop in transmittance in the near IR region. When compared with the electrical properties in section 38, this can be attributed to the increased carrier density due to increasing HF dose. Thus the sensitivity of the electrical properties to the optical data can be visualized. A higher carrier density shifts the edge of the IR tail of the transmission window towards the visible range, increasing the absorption in the TCO due to free carrier absorption. This can be visualized in Figure 36. The sample with the lowest HF concentration has the largest transmittance (also lowest thickness) with the transmittance window extending to the IR region.

Since the transmittance is also influenced by the thickness of the film deposited, hence to visualize the absorption of the film, the absorption coefficient is plotted in Figure 36. The optical thickness was estimated along the width of the foil and averaged. This is tabulated in Table 6.

From the transmission and layer thickness experiments, the absorption coefficient can be calculated as

$$\alpha = -ln(T)/d \tag{13}$$

Where T is the transmittance and d is the layer thickness. The absorption coefficient as a function of wavelength is plotted in Figure 36. The relation between the absorption spectrum and the free charge carrier density is explained in section 6.2.3.

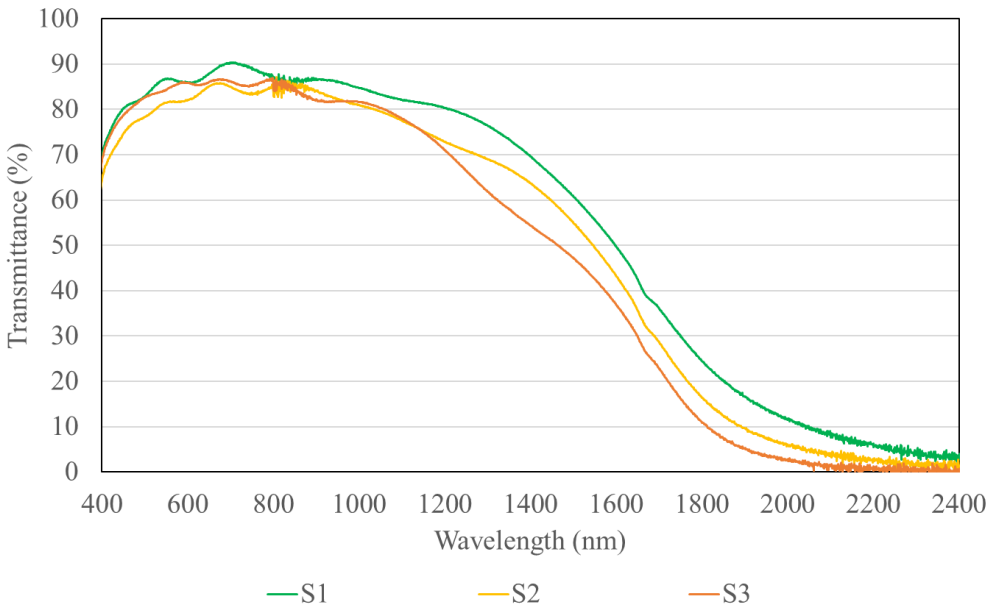

Figure 35: Transmittance measurement for recipe variation series

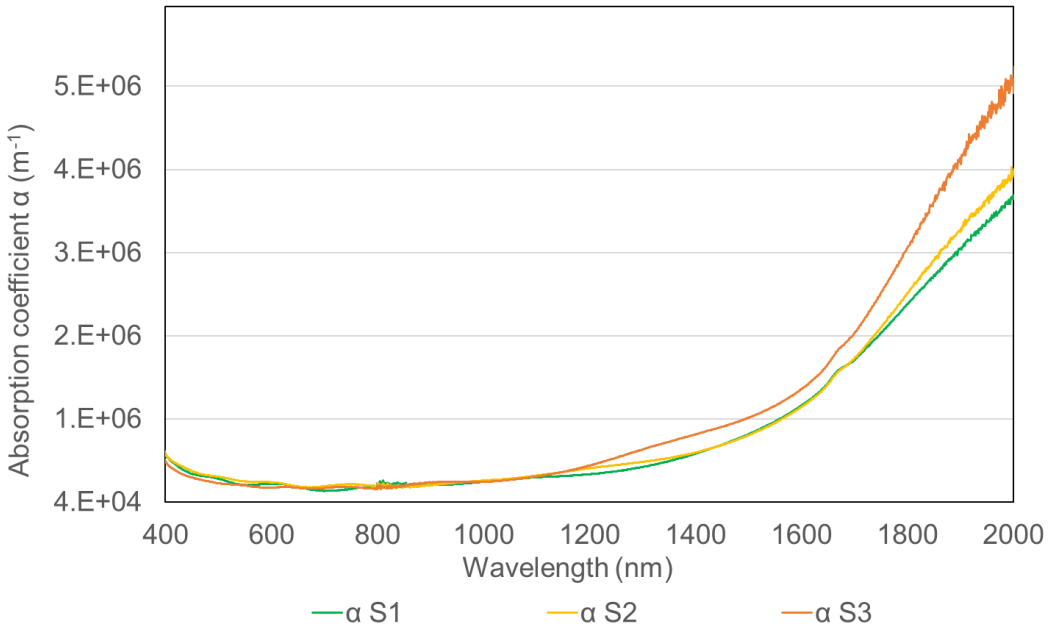

Figure 36: Optical absorption coefficient for recipe variation series

6.2.2 Morphology

It is observed that there is a definite change in the size of the grain as the concentration of HF and water is increased. The grains seem to get slightly bigger with increase in water and sharper with an increase in HF concentration. The largest grain size is seen for the sample with water/TTC= 8.1, which could also be a thickness effect as this is the thickest sample. The growth rate increases with increase in water concentration. The grain remains pyramidal

and a change in grain size is observed with increasing water concentration which can be visualized in Table 6. The top average surface grain size was calculated from the SEM images which can be found in the samples shown in Figures 37a, 37b, 37c using imageJ software and are tabulated in Table 6.

It can be observed that the gran size seems to initially increase with increase in water concentration but levels off at 306 nm. Beyond this it drops slightly to 289.6 nm. The sample with the lowest water content seems to have a more homogeneous grain size than the other samples.

The change in grain shape is visible for the different samples. In samples S1 and S2 there seems to be a dominance of pyramidal features with a point or dimple on top which gradually changes to a dominance of prismatic, twinned prismatic features, asymmetric prismatic features in samples S3 and S4. An XRD analysis of these samples would reveal more information on change in preferred orientation. This was not done in this thesis.

Further comparison of the grain size with the electrical properties will be done in the following section.

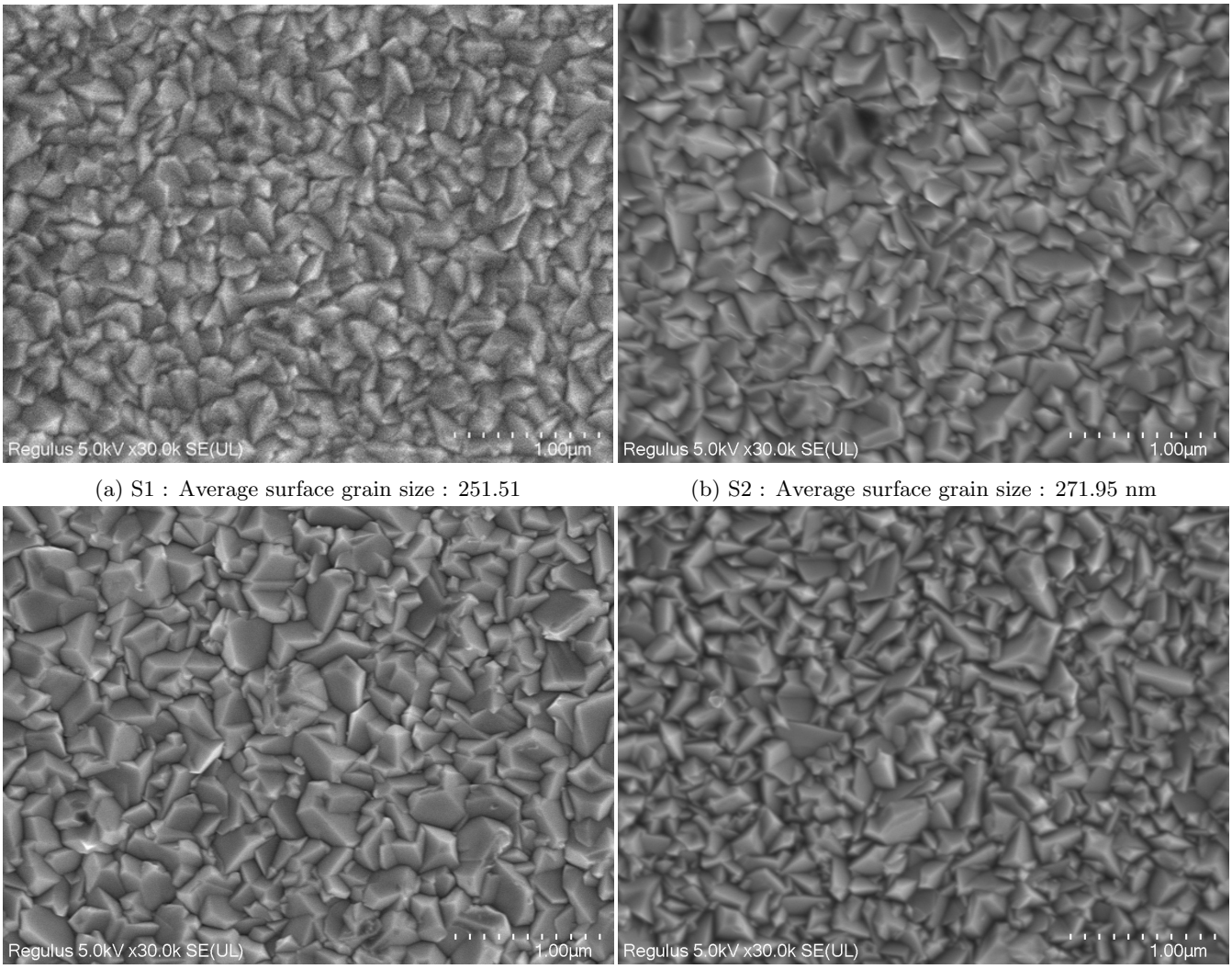

(a) S1 : Average surface grain size : 251.51

(b) S2 : Average surface grain size : 271.95 nm

(c) S3 : Average surface grain size : 306.6 nm

(d) S4 : Average surface grain size : 289.6

Figure 37: FTO deposited on Al foil with different gas molar ratios during the APCVD process.

6.2.3 Electrical properties

The mobility for all the samples is similar until HF/TTC = 0.5 after which it drops abruptly. As HF (water and methanol) concentration increases there is a rise in charge carrier concentration. The increase in charge concen-

tration is due to increase in both HF and methanol concentration as previous studies show that reducing nature of methanol contributes to the improvement in charge carrier concentration [12]. This is accompanied by a slight decrease in resistivity which can be seen in Figure 38. This increase in charge carrier concentration with increase in HF dosage also concurs with a drop in transmittance due to increased free carrier absorption. There seems to be a dopant limit (HF/TTC = 0.4) , beyond which the mobility drops despite resistivity falling due to increased charge carrier density. Despite the large grain size of sample with HF/TTC = 0.6, the mobility drops drastically at this point, which is possibly due to ionized impurity scattering. Large grain size in this case still does not promote mobility as the mobility for these carrier concentrations are limited by ionized impurity scattering [4]. This is also similar to the trend we observed in the previous experiment with HF in Section 6.1.3.

Increasing the HF/TTC molar ratio beyond 0.4 brings a very slight reduction in mobility as some of the fluorine atoms act as ionized scattering centers against mobile electrons. The other fluorine atoms are accumulated at the grain boundaries, causing grain boundary scattering [4].

Increasing dopant concentration significantly reduces the resistivity of the film, however, it reduces the transmittance due to increased IR reflectivity and free carrier absorption [12]. Furthermore, there is an optimum doping level above which the carrier transport is also reduced due to ionized impurity scattering. Thus there is a trade-off between the optical and electrical properties of the film and hence it is very important to identify the optimal doping limit of the FTO to have the best electrical performance while not compromising on the optical properties of the film [12].

It can also be seen that despite an increase in conductivity the mobility falls for dopant concentrations over HF/TTC 0.4. The thickness, morphology, and optical properties are affected by increase in water/TTC and HF/TTC.

The effect of varying HF/TTC on the electrical and optical properties is clear. There is a degradation of optical properties beyond a HF/TTC dopant limit of 0.4. The electrical properties also degrade beyond this limit which prompts us to believe that HF/TTC = 0.4 is the optimum dopant limit. Addition of HF also seems to make the grains sharper.

The effect of water on growth rate and morphology can be clearly visualized in this set of experiments as there is an increase in grain size with an increase in water/TTC ratio. There is still a limitation as the methanol and water could not be varied independently and the HF variations simultaneously did not prompt definite conclusions regarding the effect of water on the electrical and optical properties of the coating. Hence water was varied (along with methanol due to the limitation of the experimental setup) in the next set of experiments.

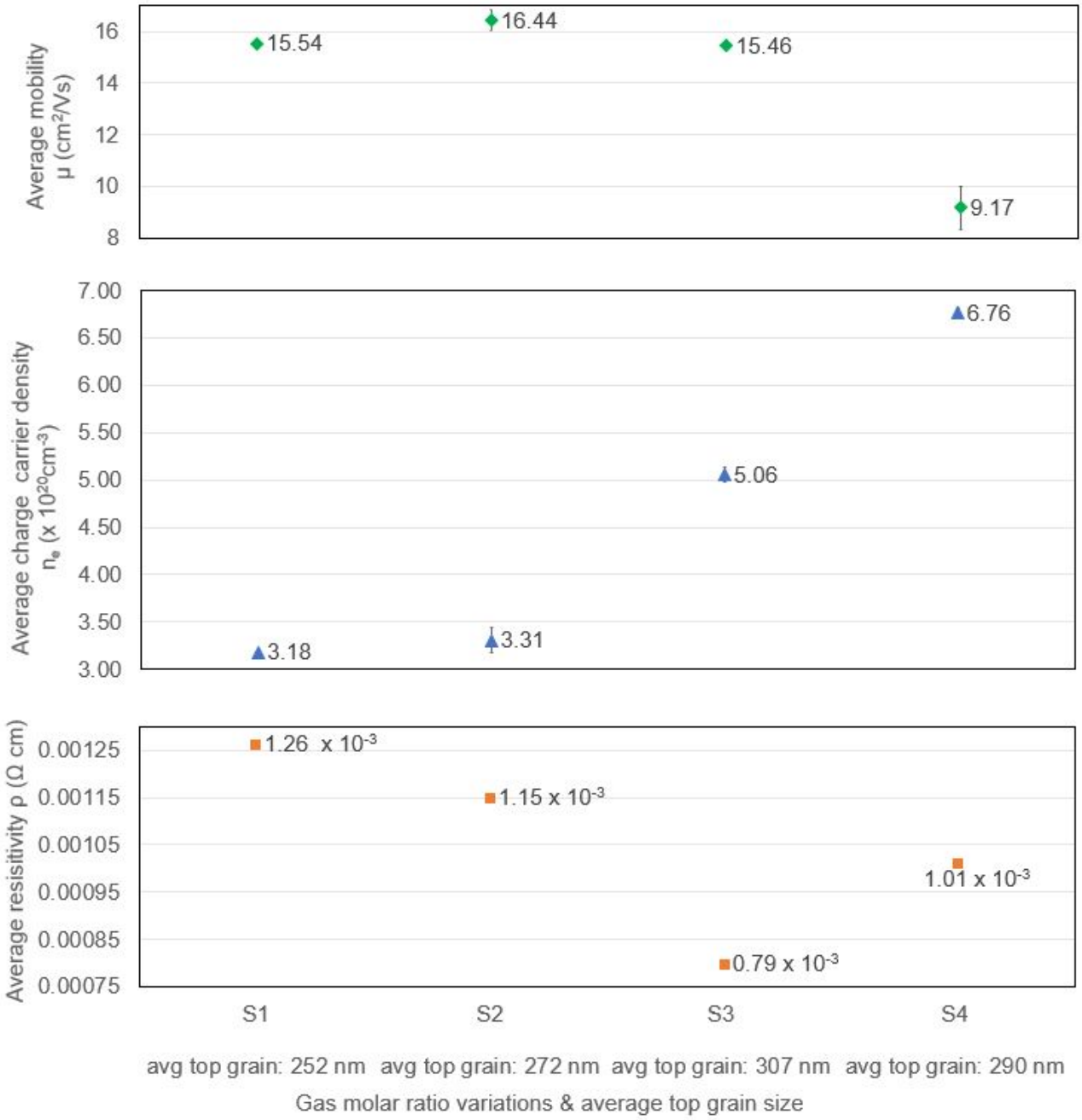

Figure 38: Effect of gas molar ratio variations on electrical properties

6.3 Effect of water and methanol

The motive of this experiment was to study the effect of water on the deposited FTO and analyze if it was possible to achieve control over growth rate and grow grains of larger size while improving the opto-electrical property of the FTO by varying the water concentration. Previous studies done by Archer in [12], showed that increasing water concentration led to an increase in grain size and an improvement in mobility and transmission.

For this experiment, the effect of increasing water concentration on the morphology of the grain was studied. Fluorine-doped tin oxide was deposited by keeping the HF flow constant and varying the water. Due to the pre-mixing of methanol with water used in the production APCVD machine at HyET, there is little possibility of variation in water concentration independent of methanol. As a result, the methanol concentration also increased on increasing water concentration. The experimental conditions, details of recipe variations can be found in Table 7.

Deposition parameter	constant recipe values
Substrate temperature (°C)	500
Exhaust pressure [Pa]	20
TTC HF CEM temperature (°C)	150
HF temperature (°C)	70
N_2 flow (TTC,HF) (ln/min)	10
Water, methanol, HF CEM temperature (°C)	60
N_2 flow (Water/methanol) (ln/min)	10
Deposition speed (m/min)	0.6
HF/TTC	0.3
Deposition parameter	Varying recipe values
H_2O/TTC	4.8
CH_3OH/TTC	0.0013
H_2O/TTC	19.7
CH_3OH/TTC	0.005

Table 7: Recipe parameters for effect of water

This series of experiment were carried out for H_2O/TTC = 4.8 & 19.7. The HF/TTC ratio was held constant at a low value of 0.3 in order to see if it affected the transmission in the near-IR region. The rest of the experimental values such as temperatures and HF flow rates were kept constant and only the flow rate of water/methanol mixture was changed. Flow rate of the carrier gas, N_2 was also kept constant at 10 ln/min.

6.3.1 Optical properties

The impact of increasing water concentration on optical properties can be seen in Figure 39. The transmittance of samples with the lowest and the highest water concentration are similar despite their thickness and slight carrier density variation. There is a slight shift in the transmittance at higher wavelengths, which could be explained by the free charge carrier density reduction. The electrical properties of the film can be found in section 6.3.3. The coating with higher concentration of water, S2 despite the higher thickness, gives larger transmittance. The optical absorption coefficient is plotted as a function of wavelength in Figure 40. The sample with the highest absorption in the near IR region is probably the sample with the highest free carrier density which can be seen from the electrical properties in 6.3.3.

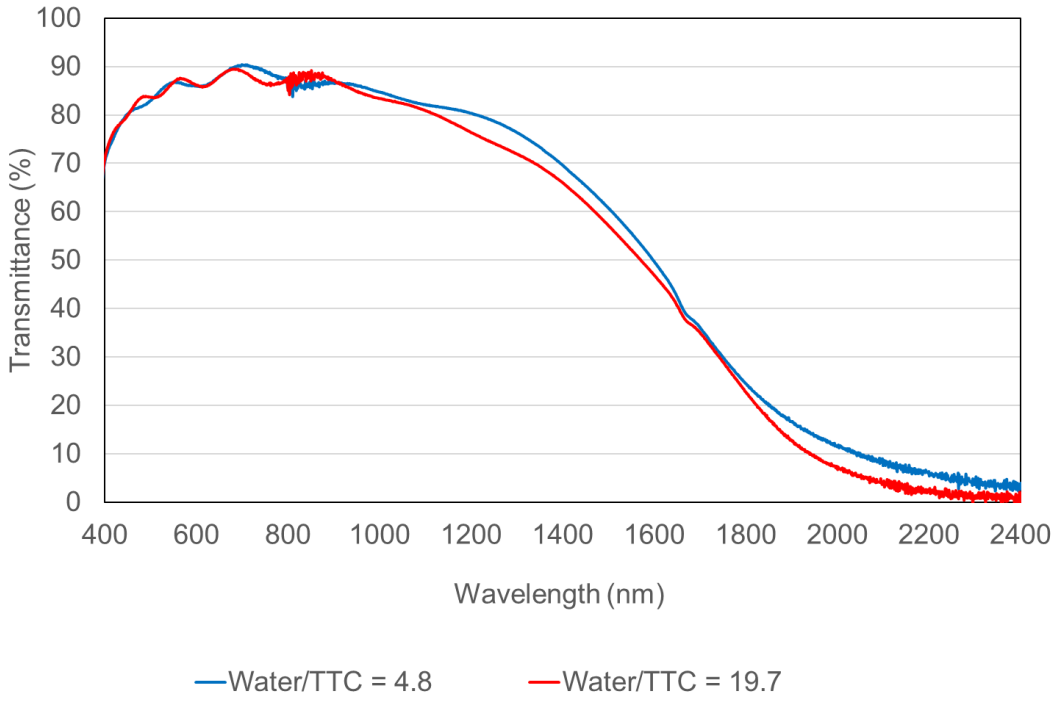

Figure 39: Transmittance [%] as a function of wavelength (nm) for different water concentrations

There are fringes present in the optical spectra between 400 and 1000 nm due to a small absorption and multiple internal reflections within the film. Assuming small absorption in this region, fringes depend on refractive indices of the substrate and film and thickness of the coating. The region of interest is considered from 400 nm as the signal below this is weak due to absorption by the glue.

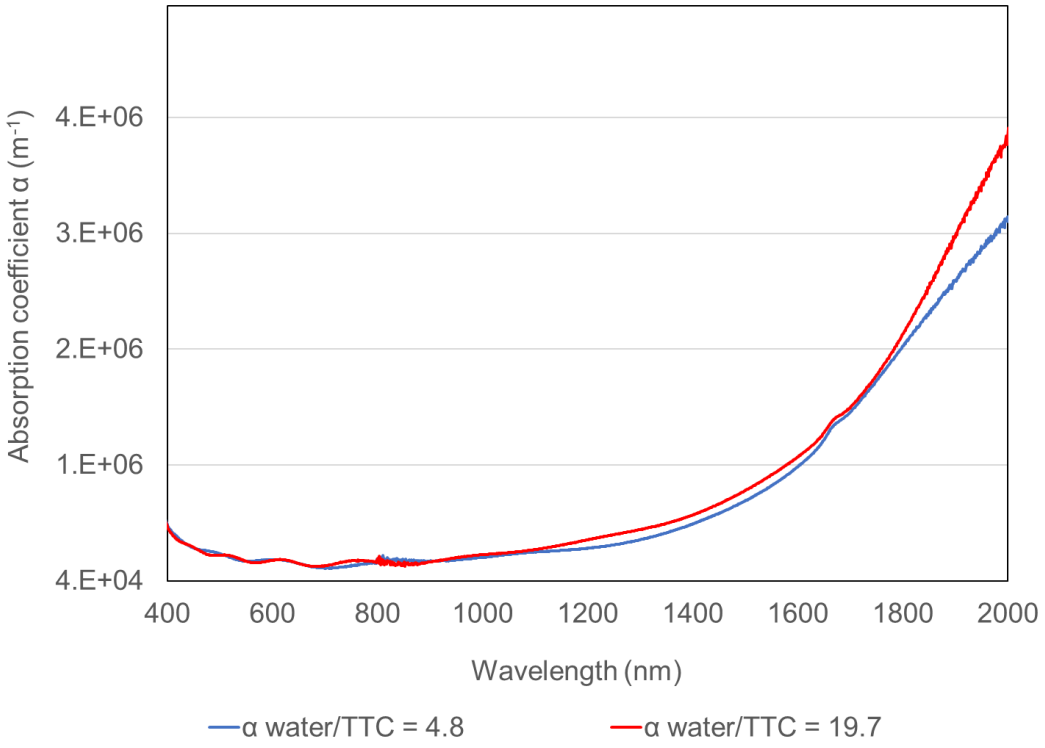

Figure 40: Optical absorption $[m^{-}1]$ as a function of wavelength (nm) for different water concentrations

The optical properties of the film show only a very subtle change in properties.

6.3.2 Morphology and growth rate

The SEM analysis shows interesting results concerning the grain size of the coating when the water concentration is increased. As the water to TTC ratio is increased, average surface grain size increases. This can be seen from the surface grain size estimated from the SEM images below in Figures 42a and 41a. The average top surface grain size was calculated using imageJ software. The values are listed in Table 8. In Figure 42a, the most commonly observed morphology are pyramidal structures with a dimple on top, triangular pyramidal shaped crystallites and prismatic features. In Figure 41a, the most commonly observed morphology are pyramidal structures and prismatic features. The XRD analysis of the sample with the highest water content can be found in Appendix B. According to the results of the analysis, the predominant crystal orientations were (101), (110) followed by (200) and (211). The XRD preferred orientation changed from dominant (200) (XRD data for water/TTC = 6.5) to (101) and (110) for larger water concentrations. This is in agreement with literature [8] and is detailed in Appendix B.

From the SEM image, the increase in nucleation layer thickness can also be visualized. For the sample with the highest water concentration, the thickness of the nucleation layer is 205 nm while for the sample with the lowest water concentration, the nucleation layer is around 126 nm, this is in agreement with the literature study that there is an increase in growth rate with increase in water concentration [6][12].

Parameter & values of water/TTC	S1 4.8	S2 19.7
Thickness of coating [nm]	450	681
Average surface grain size [nm]	343.9	457.4
Standard deviation in average surface grain size [nm]	84	81
Web speed [m/min]	0.6	0.6
Average total transmittance between 400-1000 [%]	85.59	83.29
mean free path length of electron (λ_{mfp}) [31] [nm]	13.59	18.06
RMS roughness (4x4 μm) [nm]	29.15	33.57
Average roughness (4x4 μm) [nm]	22.95	26.89
Max P-V (4x4 μm) (nm)	261.9	270.9
Skewness (4x4 μm)	-0.17	0.00799
Kurtosis (4x4 μm)	3.22	3.15
RMS roughness (16x16 μm) [nm]	-	56.09
Average roughness (16x16 μm) [nm]	-	41.61
Max P-V (16x16 μm) (nm)	-	626.6
Skewness (16x16 μm)	-	0.9277
Kurtosis (16x16 μm)	-	6.526

Table 8: Measured values for different water/TTC ratios

Both the experiments were performed at the same process settings apart from the variation in water/TTC concentration. The web speed was kept constant at 0.6 m/min and the temperature of the substrate was set to 500 °C. The water concentration was increased in two steps. (The water concentration cannot be changed independently from methanol due to the premixing in the HyET APCVD machine).

Furthermore, for the same deposition speed of 0.6 m/min the average thickness estimated across the width for the sample with higher water content (water/TTC = 19.7), is higher than the sample with lower water concentration (water/TTC = 4.8), by a factor of 1.5. This observation also concurs with literature that the growth rate increases with increase in water concentration [6],[12].

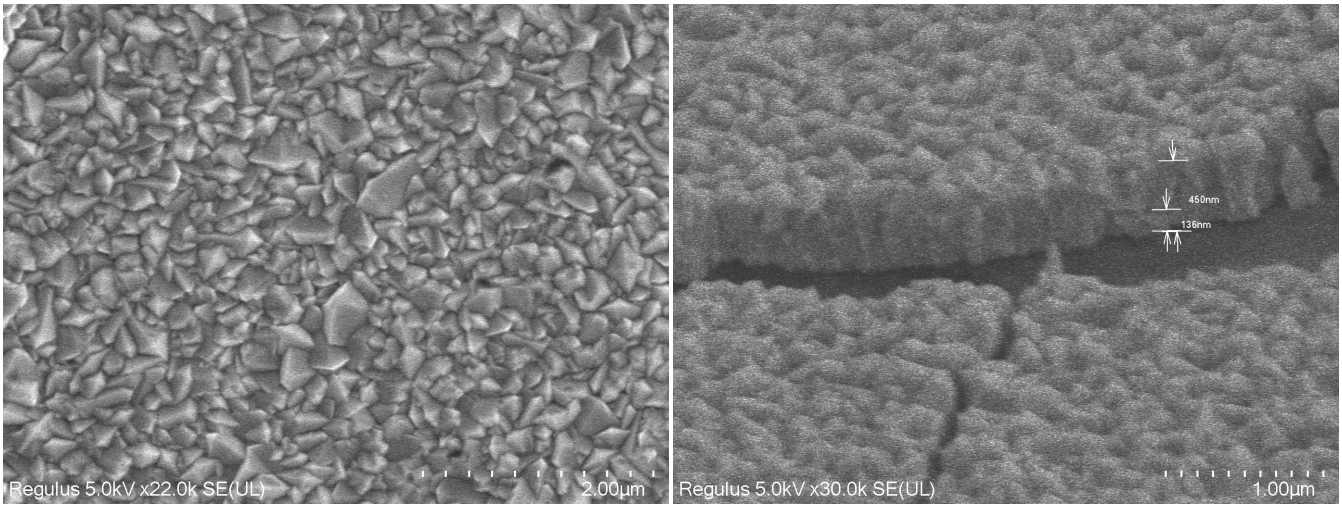

(a) Top - view SEM of H_2O/TTC=4.8

(b) Cross - SEM of H_2O/TTC=4.8

Figure 41: a) Top - view SEM of H_2O/TTC=4.8, b) Cross - SEM of H_2O/TTC=4.8

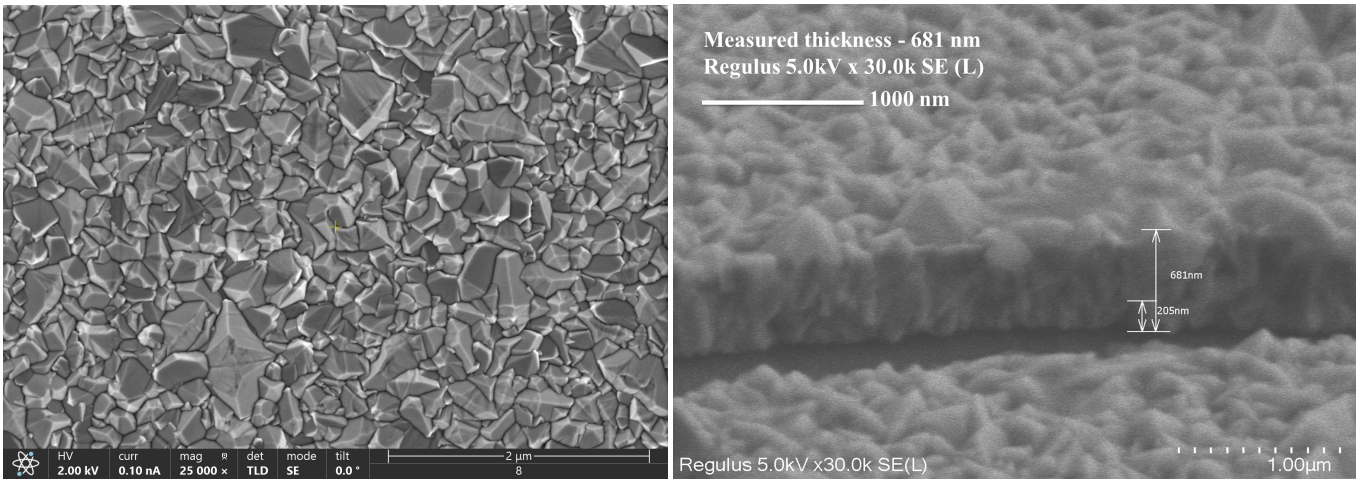

(a) A) Top - view SEM of H_2O/TTC=19.7

(b) Cross - SEM of H_2O/TTC=19.7

Figure 42: a) Top - view SEM of H_2O/TTC=19.7, b) Cross - SEM of H_2O/TTC=19.7

The RMS roughness data has been extracted from the AFM images in Figures 43, 44. It can be noted that the observed the sample with highest water concentration has the sharpest features and the largest grains with the highest roughness and the greatest distance between the highest peak and the lowest valley.

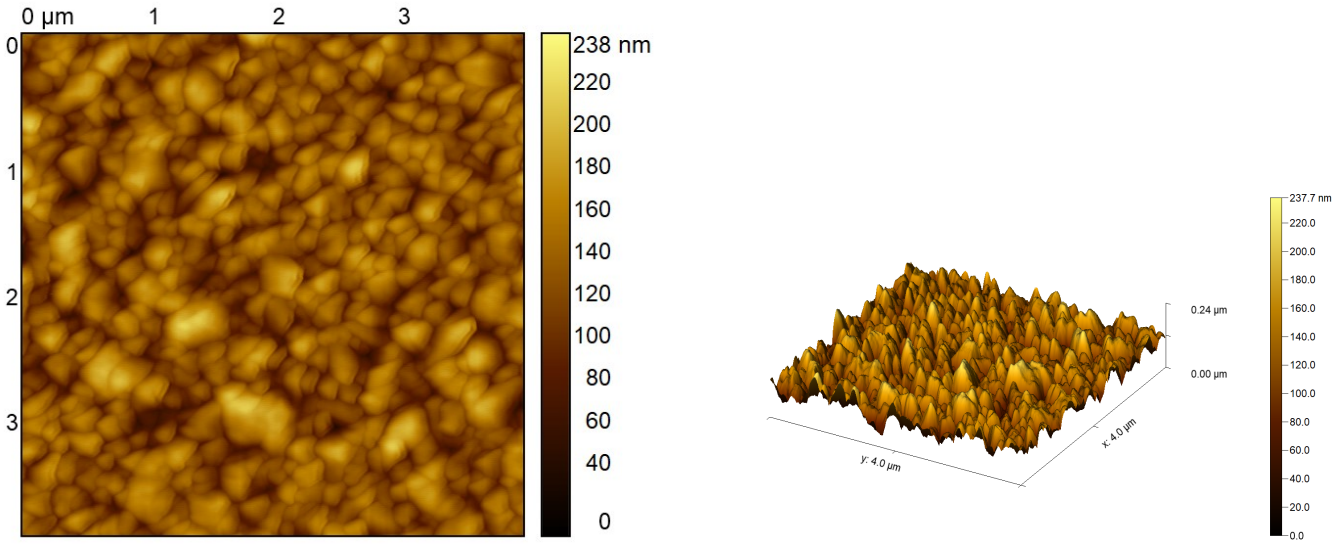

(a) 2 D AFM image of H_2O/TTC=4.8 (4x4 μm)

(b) 3D AFM image of H_2O/TTC=4.8 (4x4 μm)

Figure 43: a) 2 D AFM image of H_2O/TTC=4.8 (4x4 μm), b) 3D AFM image of H_2O/TTC=4.8 (4x4 μm)

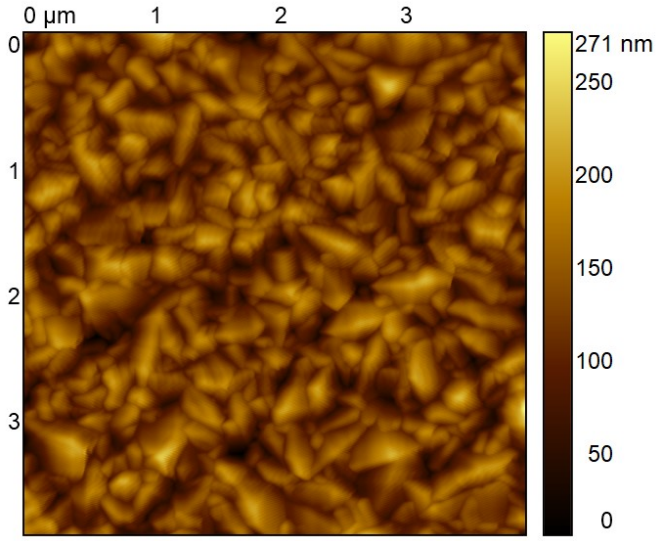

(a) 2 D AFM image of H_2O/TTC=19.7 (4x4 μm)

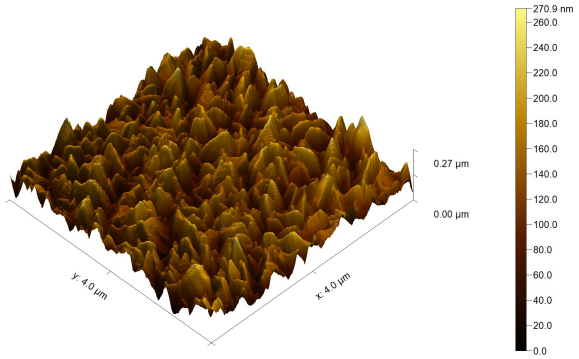

(b) 3D AFM image of H_2O/TTC=19.7 (4x4 μm)

Figure 44: a) 2 D AFM image of H_2O/TTC=19.7 (4x4 μm), b) 3D AFM image of H_2O/TTC=19.7 (4x4 μm)

From the AFM data in Table 8, we can see that the thickest sample has the highest RMS roughness. This sample is expected to have the largest scattering within the TCO-silicon interface. We expect a high haze value for the sample with the highest roughness. Figures 43 and 44 show a clear difference in the grain size, RMS roughness, and the sharpness of the peaks visually. The sample with higher water content appears to have sharper features and is more clearly defined than the sample with lower water content. The Kurtosis of the sample with highest water content indicates a surface with the sharp features in the morphology. Sharp features have led to shunting of devices in the past [32], [33].

This could result in cracking of the TCO due to increased compressive strain in this layer, contributing to shunting of devices after subsequent deposition of pin layers. In one sample it was observed that the TCO had fallen out and aluminum was detected in EDX. This is detailed in C. More samples of the same material need to be analyzed under the microscope to gain statistical evidence for this hypothesis.

6.3.3 Electrical properties

When the samples with different water/TTC concentration are compared in terms of electrical properties from Figure 45, it can be seen that the sample with the highest water concentration has a slightly lower carrier concentration which could lead to an extension of the transmission window to the near-IR range. But this was not observed in the samples. There is only a subtle change in the optical properties. They remain very similar. The concentration of the doping gas was kept constant in this set of experiments, but a variation in the HF flow due to exhaust pressure variations or a fluctuation in the MFC could explain this difference in observed carrier densities.

With increase in water concentration, there is a huge increase in mobility and a slight decrease in resistivity. Conductivity is improved by the increase in mobility. This increase in mobility could be due to the reduction in scattering across the grain boundaries due to increased grain size.

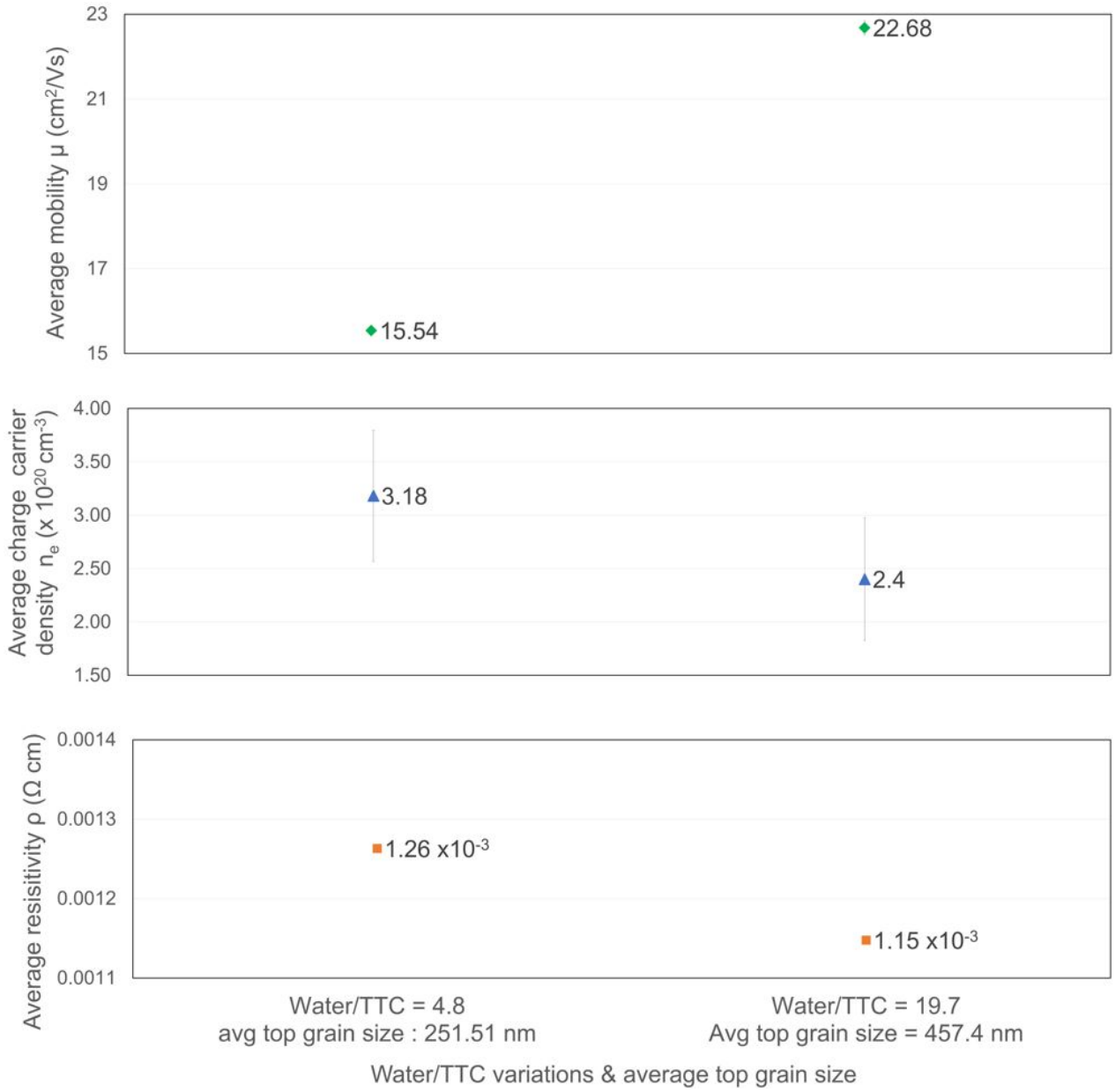

Figure 45: Mobility, charge carrier concentration, and resistivity as a function of average surface grain size for different water concentrations

The total mobility is affected by grain boundary scattering only if the grain size is comparable to the mean free path of the charge carriers (L$\sim\lambda_{mfp}$). The mean free path can be calculated using a highly degenerate electron gas model [31] given by,

$$\lambda_{mfp} = (3\pi^2)^{1/3}(h\mu/e)n^{1/3} \tag{14}$$

From the Table 8, it can be observed that the sample with higher water content has a longer λ_{mfp}, but since the mean free path of the carriers is much smaller than the observed grain size of the films for both the cases, grain boundary scattering is not the dominant mechanism. Hence the scattering within the grains (due to ionized and neutral impurities) could be the cause of reduction in mobility. The ionized impurity plays a major role in scattering and lowers the mobility of the carriers.

The increase in mobility for the sample with higher water (and methanol) concentration can be explained by two reasons. It is likely that the sample S2 with higher methanol has higher mobility due to the increase in the

methanol flow. Since an increase in methanol results in an increase in desorption of HCl from the surface of the substrate [6], increasing the number of growth sites for water. From literature review, it was found that either the elimination of the electron traps formed by chlorine in the grain boundary or the formation of very thin grain boundaries (normally assumed to be composed of chlorine containing substance) as a consequence of chloro methane leaving the surface due to the reaction of HCl with methanol could be responsible for the increase in mobility.

Thus on increasing water concentration (with reduced dopant level) it was demonstrated that higher mobilities could be achieved and the transmission could be extended to the near-IR region. Increase in water concentration also led to an increase in growth rate and the observed dominant morphology shifted from [200] orientation to [110] orientation. This is also in accordance with literature [8]. According to [29] shunting in devices was increased if the pre-dominant crystal orientation tended towards (200). So this device could have lower probablity of shunts since the preferred orientation seems to be dominantly (101) and (110) planes.

Despite the reduction in HF/TTC to 0.3, the resistivity was low and the mobility was higher, hence conductivity was improved along with an extension of the transmission window into the near-IR region due to reduction in free carrier absorption. The high surface roughness features indicate that the haze is higher for the coating with increasing water concentration. Thus, improving the light scattering properties of the film at the TCO-Si interface.

The limitation in these set of experiments was the experimental setup. The methanol, water concentration could not be varied independent of each other and due to the limited availability of resource, time on the production APCVD machine, all the variations could not be done. As a result the LAC was used for the experiments to vary methanol and water independently and to demonstrate the capacity of the research tool for extensive research. This is explained in the following section.

7 Results and discussions on the experiments on the LAC : Effect of methanol on morphological properties

From extensive literature study it was observed that nucleation during the formation of SnO_2 crystals can be controlled by means of adding methanol to the gas mixture needed for growing the SnO_2 film. The aim of this experiment was to understand the role of methanol in the APCVD process in the production APCVD machine. One of the several limitations of the machine was the premixed methanol/water concentration which made it difficult to vary the concentration of the water/methanol system independent of each other.

Additionally, performing experiments on the production APCVD machine leads to a lot of material and capital consumption. At HyET Solar, there is a need to improve the current APCVD system to learn lessons for the upscaled production capacity. As a result, a lab-scale research tool was designed in order to perform experiments to investigate the deposited material in different stages of growth and translating the lessons learnt from this to the large scale APCVD machine.

7.1 Experimental methodology

These were the first depositions done on the lab-scale APCVD tool for the deposition of undoped tin oxide. For the first deposition, $SnCl_4$ and H_2O were used as the precursors. The deposition temperature is 500 °C. LabVIEW software was used to control the deposition.

The top surface of the crystals can be seen from Figure 46a. The crystals have pyramidal features and appear to be fairly homogeneous in size. The thickness of the deposited layer is around 1770 nm which can be visualized in 46a. The thickness is the result of two passes under the injector. The thickness due to one deposition is therefore around 885 nm.

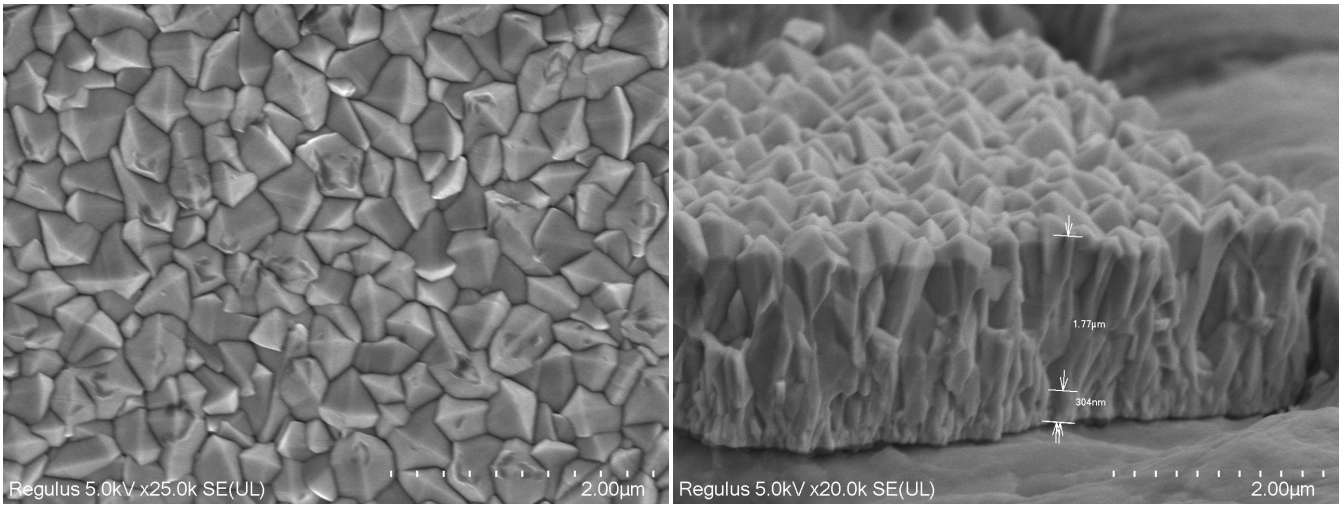

(a) Top view SEM Sample 1 : Tin oxide without methanol deposited using the LAC (double pass under the injector)

(b) Cross-SEM Sample 1 : Tin oxide without methanol deposited using the LAC

The second deposition was made with the addition of methanol and the resulting film morphology was observed.

Top view SEM analysis performed on FTO films deposited with and without methanol show a significant change in film morphology. Upon addition of methanol, the grain size is visibly reduced and there is increase in compactness, while the crystals also appear to be more homogeneous in size. This can be visualized in Figure 48a. It is clear from the SEM images that with methanol addition, the grains become much smaller but they retain their pyramidal shape and they become more homogeneous in size. Since the thickness of the sample without methanol is higher, the observed large grain size could also be an effect of thickness. But it is generally understood from literature and Figure 46b on the initial film formation in the LAC, that the growth rate is increased on reduction / absence of methanol

[6]. The nucleation stage is around 90 nm thick as can be seen in Figure 48a. This demonstrates the retardation in the growth rate of the film on addition of methanol. The film after the addition of methanol is denser and the grains are closely packed and more homogeneous in size in the film with methanol than the film without methanol addition.

From the initial literature review, it was understood that the final film morphology depends on the initial film morphology which in turn depends on the nucleation. In Figure 46a, it can be seen that the initial layer formation in the undoped tin oxide with TTC and water is around 304 nm, which indicates fast growth of the grains in the early stage of film formation. The subsequent two layers deposited on top of each other lead to fast growth of large columnar grains.

The sample in Figure 47a represents the initial film formation stage of undoped tin oxide (without methanol), which has an average thickness of around 224 nm, while the sample deposited with methanol represents the final film with methanol and has a thickness of around 289 nm in Figure 47b at a substrate speed of 0.24 m/min below the injector for a single pass. The comparable film thickness for the initial film formation (without methanol) and the complete film (with methanol) shows the impact of growth rate on the methanol concentration, and shows that there is an increase of growth rate and hence grain size and thickness in absence of methanol.

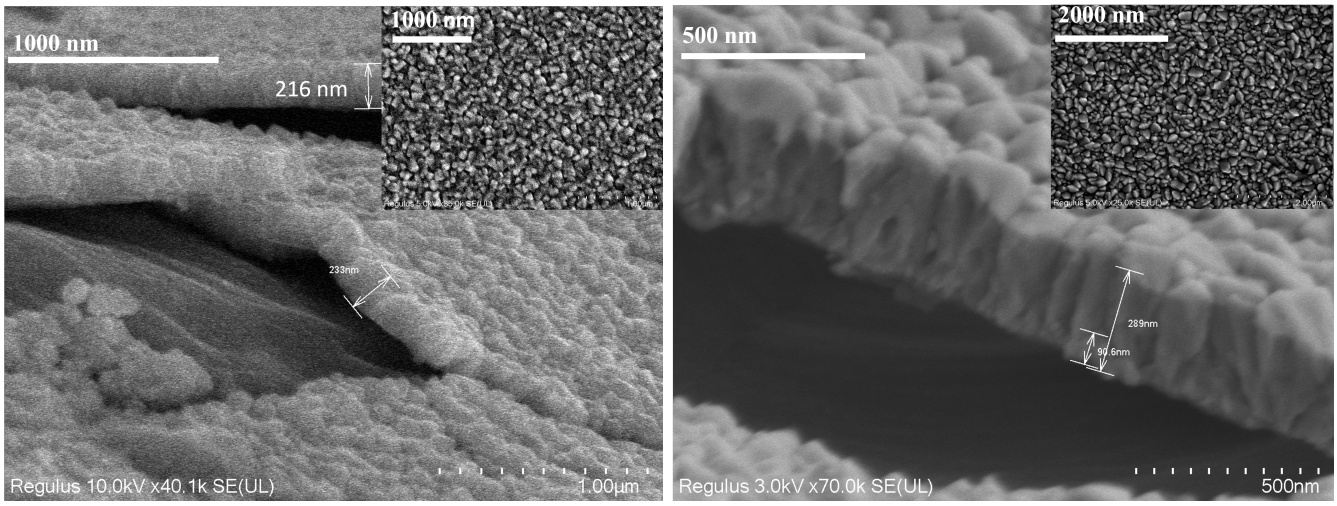

(a) Initial film formation for undoped tin oxide without methanol deposited using the LAC

(b) Final film stage for tin oxide with methanol deposited using the LAC

From the cross-SEM measurements in Figure 48b for a single pass under the injector, it can be confirmed that the thickness of the deposited material varies by a factor of 3 in case of the sample with and without methanol addition. In this series of experiments, the process parameters were kept constant except for the introduction of methanol in sample 2. The nucleation layer (around 90 nm) seems to be much smaller than the nucleation layer (around 304 nm) for films with just water and $SnCl_4$. The deposition rate visibly reduces with addition of methanol, which concurs with what is observed in literature [6],[13],[19]. Furthermore, the average grain surface size estimated using imageJ was found to be a factor of 2.4 smaller for the sample containing methanol compared to the sample containing no methanol. This further adds to the conclusion that addition of methanol (due to its competing nature with water for surface nucleation sites) leads to densification of layers and retards the growth rate [13],[6].

As stated in [17] according to heterogeneous nucleation theory, under certain conditions, after nucleation there is a critical radius r* only beyond which the the nuclei grow larger. According to [17], if methanol is considered as a surfactant in the deposition process, it lowers the surface energies of the tin oxide. This ensures that the nucleation of all surfaces becomes easier. There is a reduction in critical radii. This promotes similar growth rates for all crystals. Thus the films deposited with methanol have more homogeneous distribution of grain size [17].

(a) Top view SEM Sample 2 : Tin oxide with methanol deposited using the LAC (single pass under the injector)

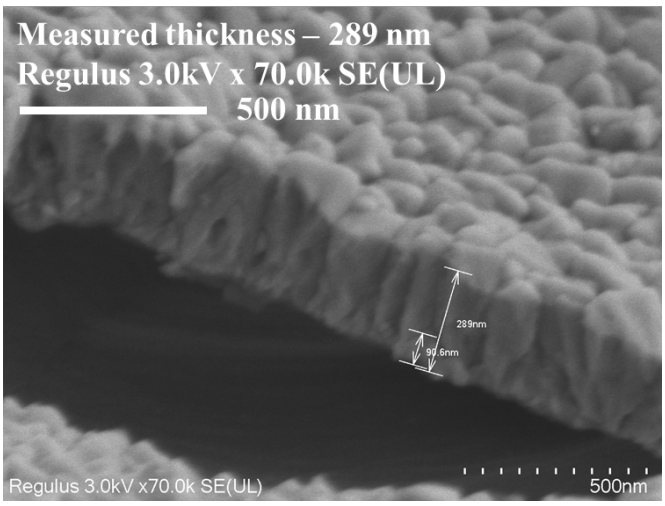

(b) Cross-SEM Sample 2 : Tin oxide with methanol deposited using the LAC

Parameter & values of methanol/TTC	0	0.01
Thickness of coating (single pass) [nm]	224	289
Web speed [m/min]	0.36	0.24

Table 9: Thickness and webspeed of sample with and without methanol

This observation is in agreement with the literature study, as it is found that the grain size of the TCOs is certainly affected by differences in methanol concentration. Larger grains can be grown at zero or lower content of methanol [13],[6],[19],[12].

The highly dense films with methanol are visualized in Figure 49 when compared to a film with no methanol. The grains appear farther apart and a large number of irregular grains and inhomogenity can be found in the film deposited without methanol than in the film deposited with methanol, where grains appear closer together, which can be seen in Figure 50; the measured values are tabulated in Table 10.

It can also be seen that the RMS roughness of the sample with methanol (deposited on the LAC) is comparable to the FTO samples deposited in the APCVD production machine adding to the belief that despite the reduced thickness the RMS roughness of the film with methanol is comparable to the RMS of films with twice the thickness. Thus addition of methanol seems to make the surface morphology rougher despite the reduction in grain size. This is in agreement with literature. Kim et al, found that increase in methanol increased the surface roughness of the film [8].

Parameter & values of methanol/TTC	0	0.01
Water/TTC	6.5	6.5
Thickness of coating (nm)	1770 (two passes)	289 (single pass)
Average surface grain size (nm)	488.4	191.65
Standard deviation in average surface grain size [nm]	84.14	43.95
RMS roughness (16x16 μm) (nm)	61.89	22.36
Average roughness (16x16 μm) (nm)	50.05	17.79
Max P-V (16x16 μm) (nm)	462.4	232.6
Skewness (16x16 μm)	-0.2132	-0.00116
Kurtosis (16x16 μm)	2.7861	3.1382
Average total transmittance between 400-1000 (%)	66	-

Table 10: Measured values of sample with and without methanol deposited in the LAC

AFM analysis was done for a few samples selected from our experiments and it was observed that the thickest samples have the highest roughness. This has been plotted in Figure 51. It was also observed that the samples which were deposited on the substrate with pre-treatment (random micro-texturing through etching) had a slightly elevated RMS roughness than the samples with no pre-treatment. This has been investigated in detail in appendix A.1.

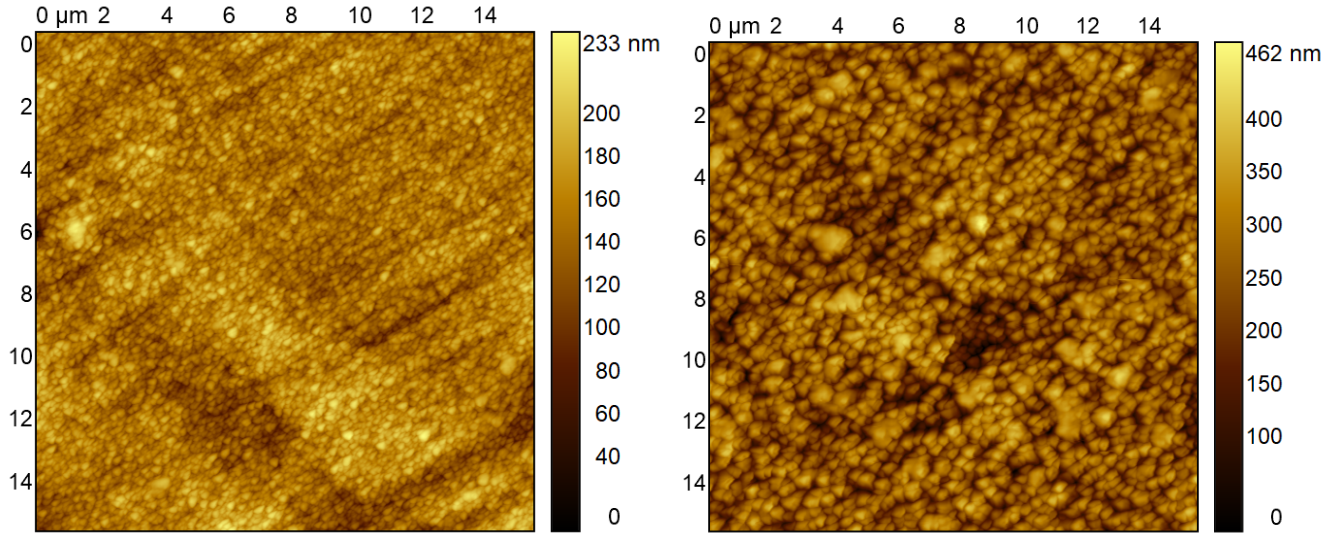

(a) AFM images of methanol/TTC=0.01

(b) AFM images of methanol/TTC=0

Figure 49: AFM images of a) methanol/TTC=0.01, b) methanol/TTC=0

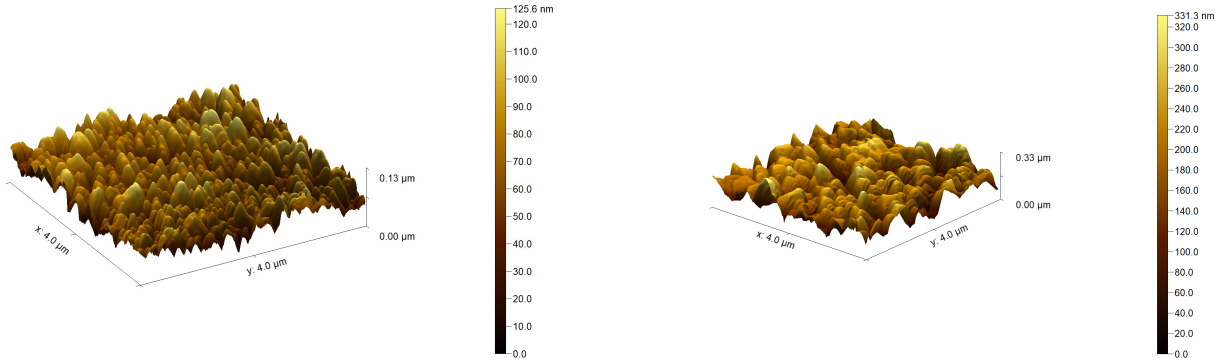

(a) AFM images ofmethanol/TTC=0.01

(b) AFM images of methanol/TTC=0

Figure 50: AFM images of a) methanol/TTC=0.01, b) Cross - SEM of methanol/TTC=0

7.2 Electrical properties of the samples without methanol deposited on the LAC

Figure 11 shows the measured carrier concentration, resistivity and mobility for the deposition of undoped tin oxide without methanol in the LAC (thickness 1770 nm). Three samples were chosen in different portions of the foil and after preparation of the sample, Hall effect measurements were carried out. The inhomogeneous distribution of charge carriers in our samples can explain the observed electron concentration trend. Unintentional doping by chlorine or oxygen vacancies can be the cause.

Electrical property	value
Average charge carrier concentration,n_e (cm^-3)	3.28 x 10^{20}
standard deviation (cm^-3)	0.47
Average resistivity, ρ (Ωcm)	1.43 x 10^-3
standard deviation (Ωcm)	8.94 x 10^-7
Average mobility, μ (cm^2/Vs)	13.46
standard deviation (cm^2/Vs)	1.71

Table 11: Average measured values of sample without methanol deposited in the LAC

The resistivity is virtually identical for all samples. There is a scatter in the mobility values across the samples. Mobility can be increased by improving crystallinity which can result in reducing scattering by neutral and ionized impurities and defects. Furthermore, reducing grain boundary scattering can be done by increasing crystal size or grain boundary passivation which can also help in improving the mobility. The low mobility values could be due to scattering due to ionized impurities as the fairly large grain size rules out scattering due to grain boundaries as the dominant scattering mechanism. The largest λ_{mfp} estimated by the degenerate electron gas model given in [31], is 13.07 nm, which is an order of magnitude smaller than the average grain size.

The large number of free charge carriers in our undoped samples can be attributed to chlorine atoms which replace oxygen sites in the lattice contributing to an increase in carrier density. A decrease in mobility can also be caused by formation of electron traps by chlorine atoms if they are located at positions other than the oxygen site [13].

Through this series of experiments on the LAC, the functionality of the LAC has been demonstrated and the potential it has for future experiments can be inferred. From the study of the undoped tin oxide films with methanol addition and with no methanol deposited in the LAC, the change in morphology on methanol addition has been clearly visualized. With an increase in Methanol dosage, the nucleation density is increased, the growth rate is reduced and grains become more compact and homogeneous in size. The surface is also rougher. These observations are in agreement with literature. In the absence of Methanol, growth rate is faster, the grains are larger and more non-homogeneous in size.

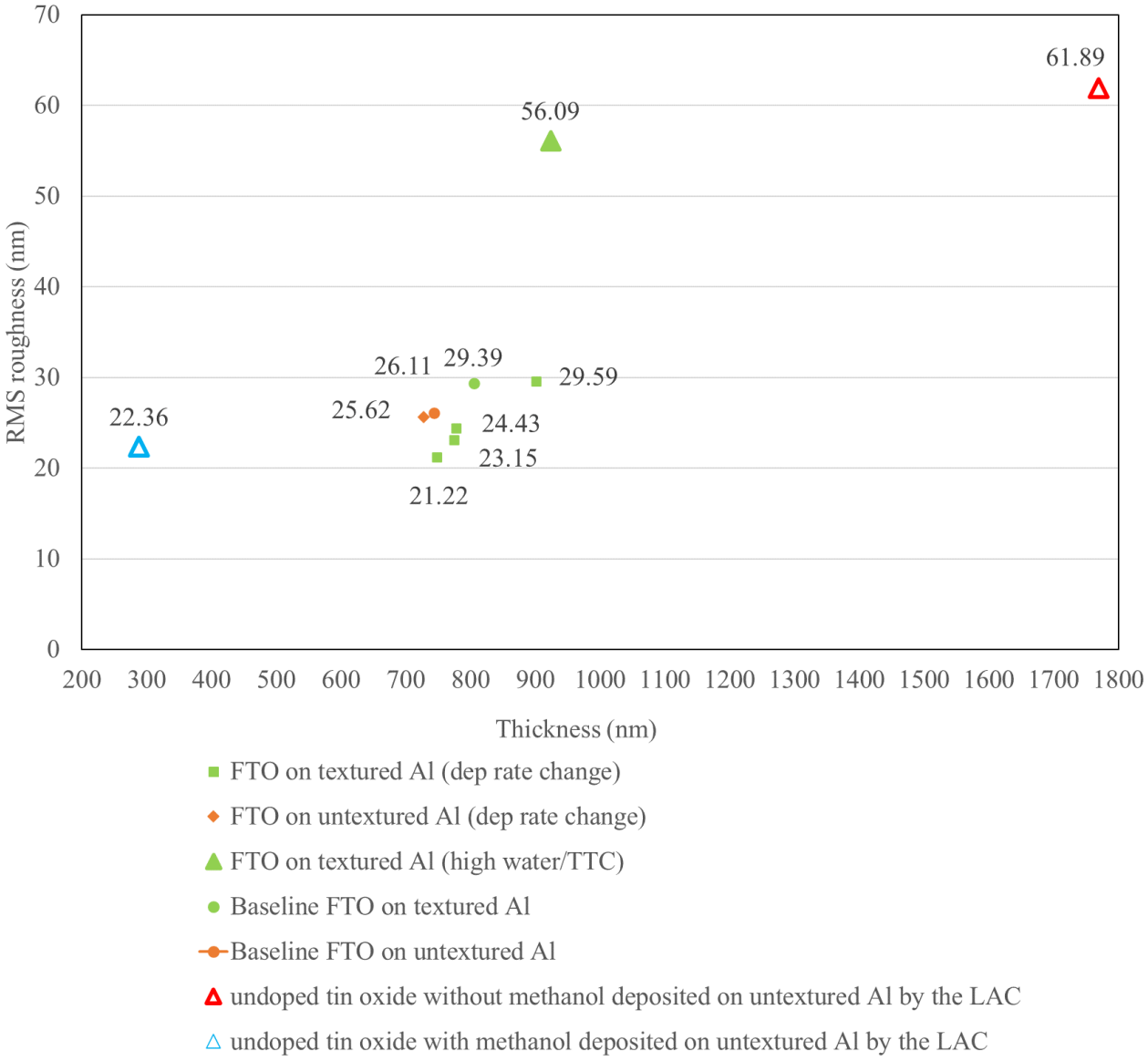

Figure 51: RMS roughness [nm] as a function of thickness (nm)

The effect of increasing thickness on the RMS roughness of the deposited films can be observed in Figure 51. The films with higher roughness are predicted to have a higher haze due to the larger number of grains, which act as refraction sites.

8 Conclusion

From the experiment on scaling up gas flow rates and deposition speed, a relation can be seen from the estimated grain size, measured optical, and electrical properties. There is minimal variation in the morphological, optical, and electrical properties at higher webspeeds and gas flow rates which builds confidence in moving to higher webspeed and gas flow rates to increase the throughput. Although not discussed in this report in detail, fabricating FTO at higher webspeeds is essential when moving towards wider Al foil widths in R2R processing, which is a crucial part of the current upscaling activities at HyET Solar.

At higher deposition speeds and gas flow rates, the morphological, optical and electrical properties are comparable and this recipe has been made the new baseline recipe for the TCO deposition process at HyET solar. To validate this recipe completely, the TCO should be used for complete device fabrication and then this device should be subject to reliability and lifetime tests.

Thus the effect of increasing deposition speed and gas flow rates on opto-electrical and morphological properties of the deposited FTO were analysed and found to be comparable. This answers the first research question.

To answer the second research question on finding effect of change in growth rate, extensive literature was reviewed and the importance of substrate temperature has been realized during initial literature study. The deposition rate changes by a factor of two for a 50 °C change in temperature. High temperature helps in annealing out defects in the films and increases deposition rate as the result of decreasing activation energy, this helps in improving the growth rate. The temperature also influences the crystal orientation which changes to (200) as the dominant orientation at high temperature.

To answer the third research question on improving opto-electrical properties by varying process gas molar ratios, It was attempted to find the optimum dopant concentration by varying HF/TTC ratio. It was observed that the decrease of transmittance in the infrared wavelength around a typical wavelength of 1500 nm is connected to the plasma edge λ_p. Above λ_p the FTO reflects all radiation. Below λ_p it is (partially) transparent. From simple Drude theory, treating the free electrons as a free electron gas, it can be shown that λ_p is proportional to 1/sqrt(n_e). This is the reason why the HF containing samples with their larger carrier density have a smaller value of λ_p than those without HF. In more detail, even within the HF containing group of samples, the ones with slightly higher values of n_e can be seen to have slightly lower λ_p than those with lower n_e. Thus the sample with HF/TTC =0.4 in Figure 31 has the transmission curves that appear to be shifted slightly to higher wavelengths. This sensitivity of electrical properties to an optical measurement can be used to make a rough estimate of the charge carrier density of the sample.

From the experiments on HF variation, HF/TTC = 0.4 was found as an optimum beyond which there is a degradation in opto-electrical properties of the film.

By varying the water (water-methanol) concentration, it has been demonstrated that we can we achieve control over growth rate, achieve larger grain size (around 457.4 nm), high mobility (around 22 cm^2/Vs), and extend the transmission range by lowering dopant concentration.

From the experiment on trying to achieve larger grains by varying water concentration, it has been observed that the grain size of the TCO crystal increases with water concentration. At lower water concentration the size of the grain was around 343.9 nm which increased to 457.4 nm as the water concentration was increased. The clear increase in growth rate can be visualized as the thickness increases from 450 to 681 nm at the same deposition speed. In our set of experiments we have been limited by the experimental set up such that we were only able to increase the water concentration by increasing methanol simultaneously, which could have influenced our experiment as methanol competes with water for reactive surface sites, thus lowering deposition rate. This counters the role of water which increases deposition rate. But since the concentration of methanol was quite low in our experiment, the influence of water on the deposited material properties can be analysed.

From the AFM images, for the samples deposited on the production APCVD machine, we observe that the sample with the highest water content has the largest grain size and roughness. The observed surface morphology from SEM and AFM also concur with the optical and electrical measurements. The large pyramidal grains with rough features have the highest direct transmittance and are expected to also have high value of haze. They are hence expected

to facilitate better light trapping and increase the average path length of the photons within the silicon layer stack. These large grains also have an extended transmission window into the near-IR region, but more statistical evidence is needed to confirm this. This is due to the lowest number of charge carriers in this film compared to any other sample in our series of experiments. The increase in mobility and extension of the transmission window into the near-IR range (due to reduced charge carriers) can be explained by desorption of chlorine by methanol, reducing the carrier density on one hand while also reducing the contribution of chlorine to scattering effects (boosting mobility) [6].

From our analysis on the electrical properties of the deposited FTO, we observe that the mobility is dominantly limited by the grain boundary scattering if the grain size is comparable to the mean free path of the electrons. All of our samples had a larger grain size which was an order of magnitude larger than the mean free path. This large grain size makes the influence of grain boundaries insignificant. The mobility was thus found to be limited dominantly due to ionized impurities for two cases. The first case is for films containing only oxygen vacancies (LAC samples with no dopant or methanol) in Figure 11, which are double ionized and give the largest scattering contribution. This is the case for the undoped tin oxide films deposited by the LAC. The other case is where single ionized donors provide scattering (fluorine or chlorine), which occurs when the doping limit of fluorine is exceeded. From our series of experiments on HF variation, HF/TTC = 0.4 was found to be the dopant limit beyond which the mobility degraded due to scattering by excess fluorine donors. In our samples lowering of mobility due to inactive dopants is not a cause as in our process with high temperature of around 500 °C, all of the fluorine atoms are thermally activated.

To answer the final research question which was to study the effect of methanol on nucleation and growth rate, two depositions were made on the LAC, one with and one without methanol. In the samples deposited by LAC, a clear variation in surface morphology can be seen by the addition of methanol. The film with no methanol grows 3 times faster than the film with methanol (for a single pass under the injector). This result underlines that variations in LAC regarding methanol concentrations in particular can be readily done, while this is practically harder to do on the production APCVD machine where the methanol concentration is fixed.

From the AFM images we observed that the sample with methanol has sharply defined features, is denser (high nucleation density) and more homogeneous in size with a high RMS roughness for low thickness. Methanol added in the right amount can help in influencing the nucleation rate and control the initial film formation, help in lowering the defect density in the crystal (pinholes/voids) and avoiding irregularities in grain size. The undoped samples with water have a higher carrier density due to the presence of oxygen vacancies and unintentional doping due to chlorine. The mobility of these samples is reduced due to scattering which rises with the presence of chlorine. Chlorine desorption due to methanol may reduce this effect [6].

The operation of the LAC has been demonstrated and a few experimental depositions have been made which are explained in this thesis. With the LAC it is possible to work with different concentration of process gases and this can be adjusted easier than in the production APCVD machine. This also saves a lot of material, time and cost. The potential of LAC in future experiments for TCO deposition is thus obvious. The LAC can be used as a research tool to further optimize recipe settings and fine tune process parameters which can then be translated to the production APCVD machine.

To raise mobility levels, larger crystallites or lower impurity levels must be achieved. In this series of experiments, larger grain size has been achieved and the target values of mobility greater than 20 cm^2/Vs, as well as pushing of transmittance window slightly to the infrared region has been done.

The electrical and optical properties of the deposited FTO are mainly determined by the process parameters such as temperature, grain size, and growth rate determined by precursor ratios, thickness as determined by extraction pressure and deposition rate. The growth rate of tin oxide is influenced by the temperature and methanol concentration. The temperature increases the growth rate of the layer while addition of methanol retards the growth rate. HF concentration seems to have a little effect on the growth rate.

In the Hall effect measurements a scatter in the charge carrier density can be observed even in samples of the same HF/TTC ratio. This could be an effect of the pressure variations in the exhaust or the fluctuation in the MFC or an artifact in the preparation of samples for Hall measurements. This needs to be investigated further.

9 Summary

This research highlights the importance of optimization of the transparent conductive oxide layer. There is a need to go to higher gas flow rates and web speed in order to increase the throughput in an R2R process. This section will contain the summary of the research done so far.

It was demonstrated that there is a possibility to go to higher web speeds and deposition rates while preserving the opto-electrical and morphological properties of the TCO. From the experiments on HF variation, HF/TTC = 0.4 was found as an optimum beyond which there is a degradation in opto-electrical properties of the film.

Properties of transparent conductive oxide (TCO) films deposited by chemical vapor deposition (CVD) highly depend on their morphology. Since early film formation is an important factor, the effect of methanol on nucleation and morphology was studied.

For the samples deposited on the LAC and the APCVD machine, film growth was investigated under the SEM. An AFM image was taken to demonstrate the increase in lateral and spatial resolution. Together with SEM, AFM was used to study the effect on morphology of the TCO on variation of HF, methanol, water concentration in CVD films deposited using tin tetra chloride as the metal precursor and water as the oxygen source. Differences in density, grain shape is observed in the case when methanol is added to the deposition process.

Addition of methanol leads to slower film growth but increases the nucleation density resulting in less porous and smaller grains in the film. This can be summarized in Figure 52. Addition of water increases the growth rate and leads to larger grains, improving optical and electrical properties. But there is a possibility of introducing shunts in the device due to high possibility of pinholes and defects due to fast growth rate. Further optical absorption coefficient and transmittance measurements were done along with Hall effect measurements to determine the improvement/degradation in the opto-electrical properties of the deposited TCO.

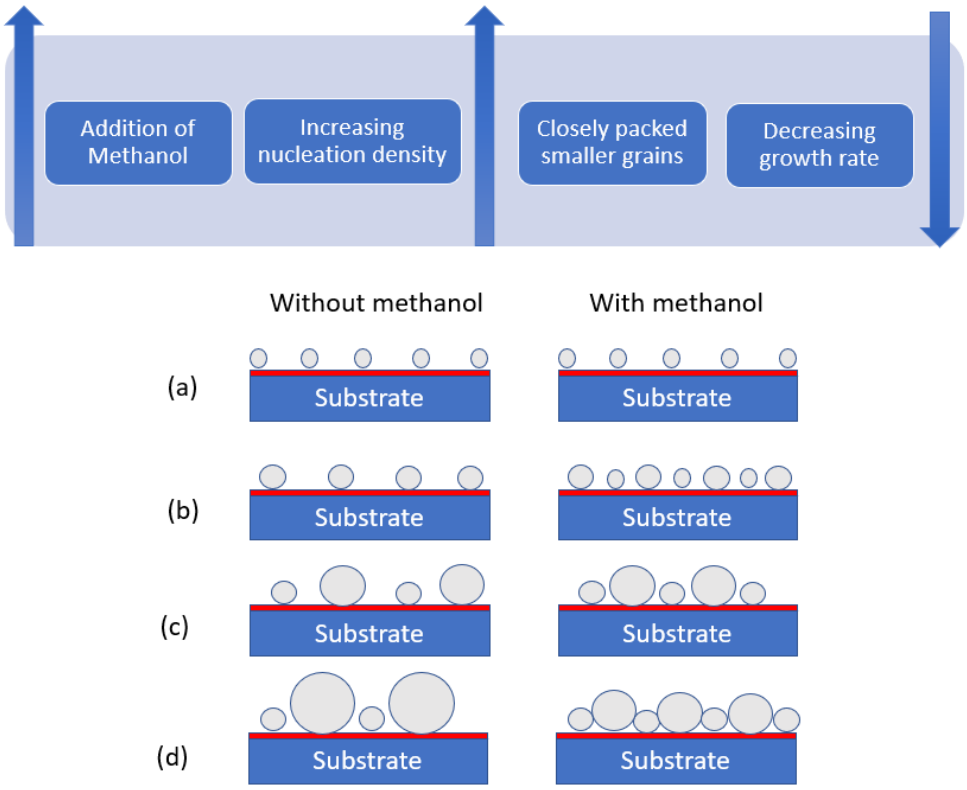

Figure 52: Effect of methanol on density and growth rate [13, 6]

10 Recommendations

The dominance of a certain type of scattering is highly dependent on the carrier density. From the experiments and calculations performed, it can be observed that the mean free path length of the electrons are an order of magnitude lower than the observed grain size. For thicker samples with high charge carrier density of the range 2 x 10^{20} $cm^{-}3$ and above, grain boundary scattering is not the dominant mechanism. This has led to the conclusion that the mobility is limited majorly due to ionized impurity scattering. Further post deposition annealing can help in grains merging with other grains reducing grain boundaries and further hydrogen treatment can lead to defect passivation at the grain boundaries and help improve mobility. This is a step towards future work on the TCOs. This is already done at HyET during the deposition of the pin layers on top of the TCO. The mobility after (different) high temperature post-deposition annealing and defect passivation by treatment in presence of hydrogen can be explored to further improve the mobility of the TCO and this can be investigated extensively to quantify the mobility values of the resultant TCO.

Extensive literature study has also made it clear that the initial film morphology influences the final film morphology. The initial film morphology in this case is influenced by the aluminum substrate. Aluminum substrate has some inherent roughness due to the production process of aluminum (for example deep grooves due to milling which appear as milling tracks) which when subject to further pre-treatment (random micro texturing of the foil surface) leads to enhanced roughness due to the micro-textures caused by pre-treatment. The pre-treatment also exposed some Fe-Si alloys on the surface of the TCO. The quality of the TCO that grows is partially determined by the substrate on which it is deposited. So it is important to make sure there is quality control of the Aluminum substrate that is used for deposition (lesser surface contamination OF Fe-Si/ other alloying particles). Furthermore, the pre-treatment has to be fine tuned so it does not expose the Fe-Si particles which are a part of the alloy to the surface of the aluminum foil, which would in principle help in further investigating the quality of TCO deposited, without hindering the investigation.

The first injector deposits the initial nucleation layer and the second injector deposits the layer on top of the nucleation layer. Thus the reaction mechanism is not identical to the initial nucleation layer on the aluminum substrate as the grains are formed on existing SnO_2 crystals instead of bare aluminum foil. This could be a possible investigation path to understand how this influences the growth of the grains. This research could be done in the LAC

Since addition of methanol leads to less porous film, the methanol could be higher in injector 1 to improve nucleation density, reducing the possibility of pin holes and defects in the film and then reduced in injector 2 to promote larger grain size. This could be an interesting topic for future investigation.

For any given substrate temperature, crystallization / grain size increases with increasing post-deposition annealing temperature. With this in mind it is proposed to introduce more water to bring down the substrate temperature while still preserving high growth rate and improving the opto-electrical properties and reducing wrinkle formation. This can be studied with the help of XRD.

To raise mobility levels, larger crystallites or lower impurity levels must be achieved. In this series of experiments large crystallite size has been explored. Another probable route would be to reduce impurity levels to improve the mobility.

A Appendix

A.1 Haze measurements

Texture plays a crucial role in the light scattering and therefore the haze. To observe the change in light scattering due to texturing, the samples were analysed in transmission mode in UV-VIS spectroscopy and haze was determined. Surface morphology was analysed using AFM and SEM images. Two depositions were made, one on pre-treated aluminum foil and the other on untreated aluminum foil. These set of samples were subject to identical process conditions such as temperature (500 °C), web speed (0.6 m/min) and gas flow rates. The only difference was the substrate. The variation in their optical property might give some insight into the light scattering effect of these samples. TCO was deposited on textured aluminum (8011A alloy) (pre-treated) and TCO was deposited on untreated bare aluminium (1050 alloy), after which these samples were transferred onto PEN (this transfer process is detailed in section 4.1) and the aluminum was etched away then the optical properties of the samples were compared.

In order to characterize the optical properties of the samples, total transmittance and diffuse transmittance were measured by UV-VIS NIR spectroscopy. The diffuse transmittance is a measure of transmittance whereby light passing directly through the sample is not collected. Using these two measurements, the haze factor was determined to study the light scattering capability of the film.

A.1.1 Methodology

A CARY 5 spectrophotometer was used for total transmission and haze measurements between 200 and 2500 nm wavelength. The haze (H_T) was measured in transmission by measuring the diffuse (T_{diff}) and total (T_{tot}) transmitted electromagnetic waves. We consider the region from 400 nm since the signal below this wavelength is too weak due to absorption by glue. For reference the haze measurement for Asahi TCO (FTO deposited by APCVD) on glass can be found in Figure 54. This has been adapted from literature.

The total transmittance is defined by the sum of the specular (non-scattered) transmittance and the diffuse (scattered) transmittance. The haze can be expressed by:

$$H_T(\lambda) = T_{diff}(\lambda)/T_{tot}(\lambda) \tag{15}$$

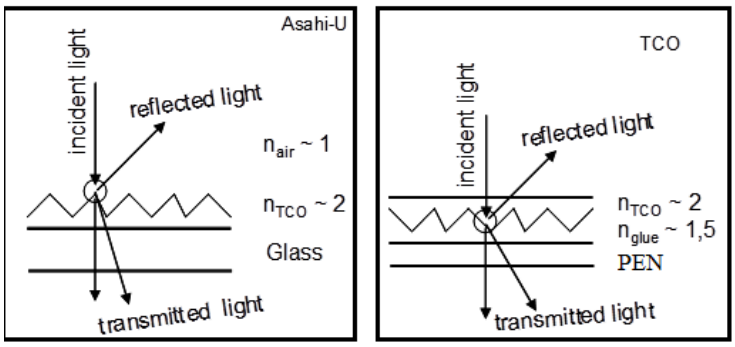

Figure 53: On the left is the Asahi TCO and on the right is the Scheme of TCO sample deposited at HyET. Figure has been adapted from [11]

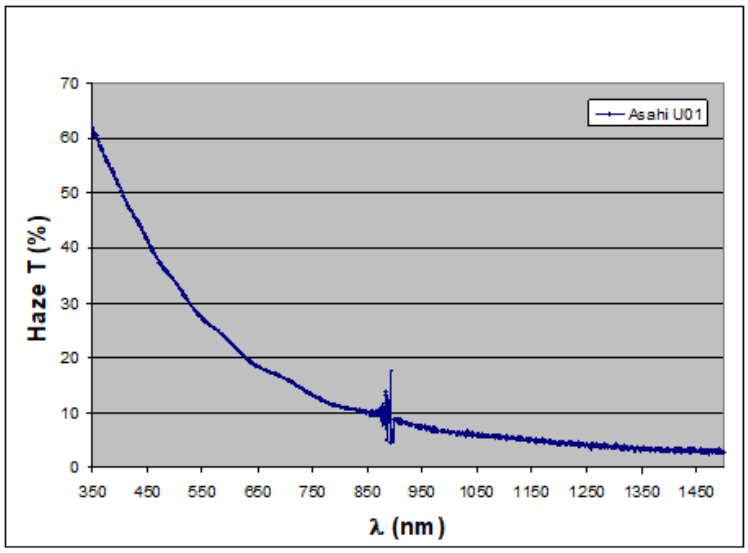

Figure 54: The measured haze of air/Asahi-U-TCO/glass. This figure has been adapted from [11]

A.1.2 Results

A schematic overview of the samples is given in Figure 53.
The measurement of the haze is given in Figure 55. There was a slight difference in haze between the TCO samples. The haze is low in comparison to a reference TCO sample on glass (in Figure 54) due to the smaller refractive index difference at the TCO / glue interface n_{TCO}-$nglue$ (2-1.5) as compared to the air / TCO interface n_{air}-n_{TCO} (1-2) of the reference (Asahi-U).

The haze of FTO deposited on textured Al substrate is higher than the haze of FTO deposited on untreated Al substrate.

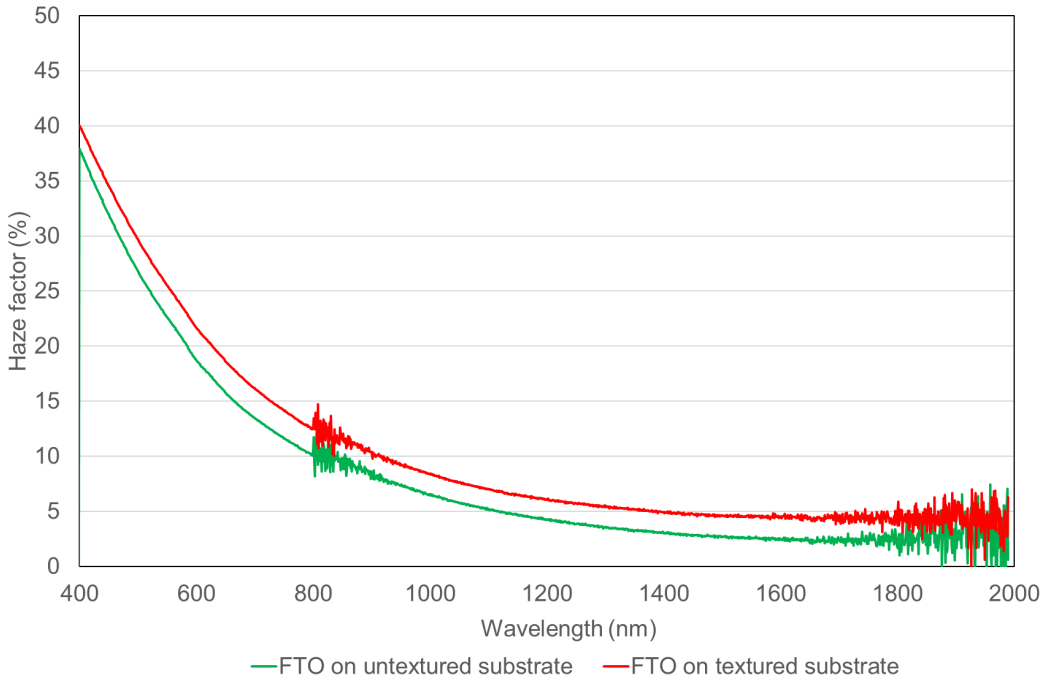

Figure 55: Haze factor for TCO deposited on textured (treated substrate) and Bare/untextured (untreated substrate) Al substrate surface

Furthermore, AFM measurements were carried out on these samples to see the morphology of the coating with higher haze. All the data regarding the AFM measurements have been tabulated in Table A.1.2.

Parameter & values of	Textured/ treated Al substrate	Untreated Bare Al substrate
Thickness of coating (single pass) (nm)	694.38	743.27
RMS roughness (16x16 μm) (nm)	27.89	26.11
Average roughness (16x16 μm) (nm)	20.96	20.5
Max P-V (16x16 μm) (nm)	390.7	272.2
Skewness (16x16 μm)	0.2613	-0.01165
Kurtosis (16x16 μm)	4.25	3.7222
Average total transmittance between 400-900 [%]	83	80.3

Table 12: Measured value for sample deposited on treated and untreated aluminum substrate

From the AFM measurements in Figure 56, we can see a clear difference in the observed surface morphology of the samples with and without substrate texturing. FTO deposited on Al substrate with pre-treatment seem to have several smaller projections on the grain surface which can act as refraction sites, increasing haze.

In the sample with substrate texturing, numerous fragmentary small pieces were observed on the grain surface, which could be relatively small grains with inhibited growth on the surface, due to the impurities that interrupt the continuous growth of the crystal.

FTO deposited on the Al foil with pre-treatment seems to have large sausage like projections, (these projections which are precipitants exposed by pre-treatment, are covered uniformly by the TCO) compared to the samples without any pre-treatment which seem more homogeneous and seem to have no precipitants. This can be visualized in the SEM images which can be found in Figure 57.

It should be noted that the aluminum substrates which were used for the TCO depositions were of different alloys

of aluminium which have different surface roughness parameters.

The average surface roughness seems the same for both the FTO samples but the RMS roughness is higher for the sample which was deposited on a pre-treated aluminum substrate despite lower thickness of the FTO deposited, around 50nm thinner.

Previously, we observed sensitivity of RMS roughness to the slightest change in the thickness. Despite higher thickness, FTO deposited on untreated Al substrate has lower RMS roughness than the RMS roughness of FTO deposited on pre-treated Al substrate (which is 50 nm thinner). This could be due to the micro textures created on the aluminum for random texturing. As expected the coating with the highest haze was the sample with higher surface roughness (which seemed to have inhomogeneous features) as it has higher number of grains which probably function as refraction sites [34].

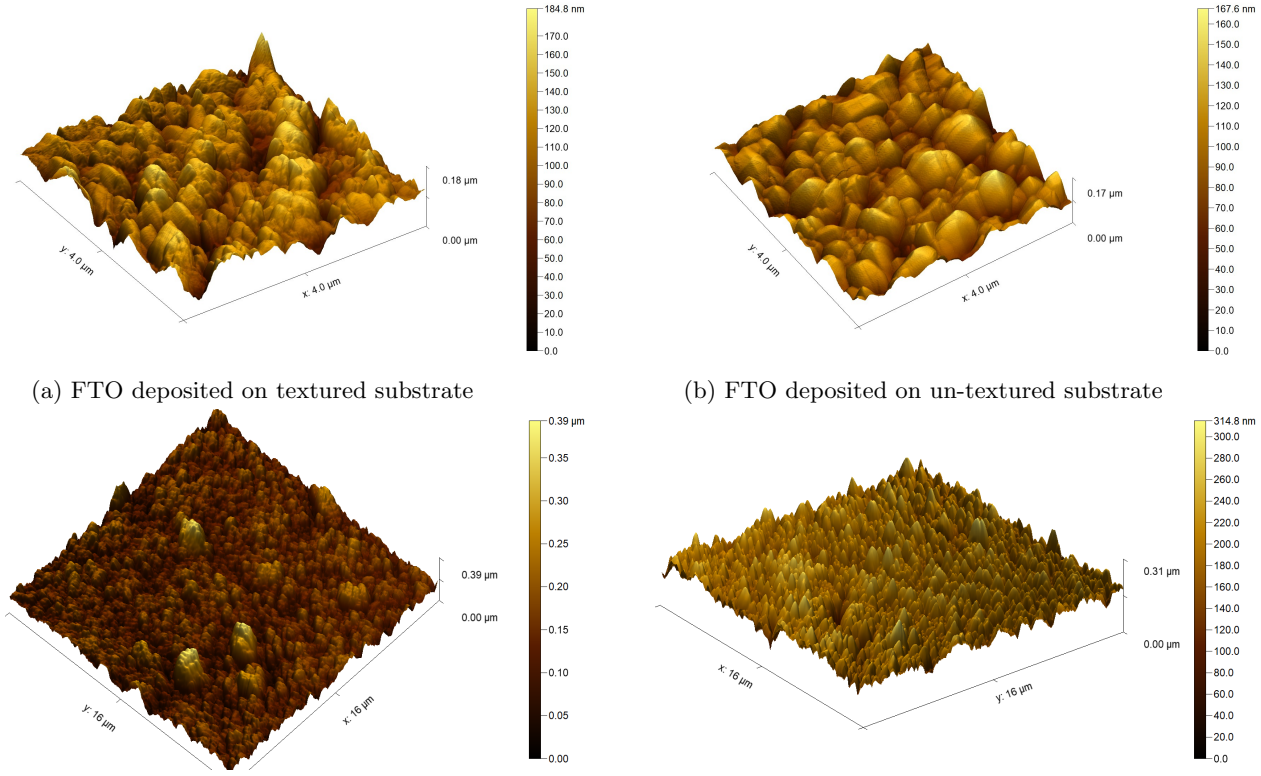

(a) FTO deposited on textured substrate

(b) FTO deposited on un-textured substrate

(c) FTO deposited on textured substrate

(d) FTO deposited on un-textured substrate

Figure 56: AFM images of FTO deposited on textured and untextured substrate

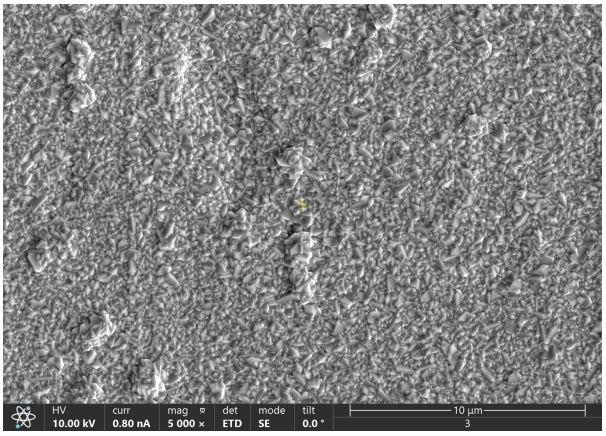

(a) FTO deposited on textured substrate

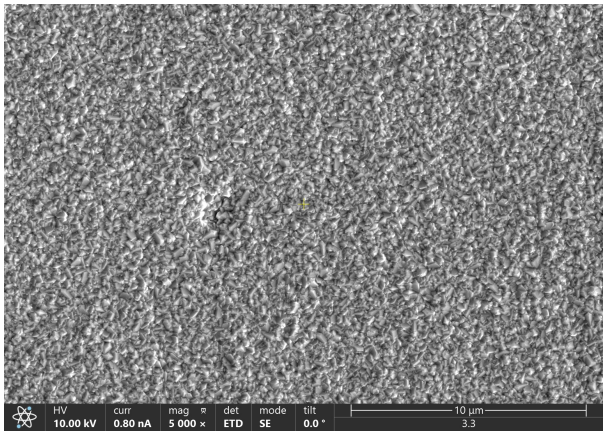

(b) FTO deposited on un-textured substrate

Figure 57: SEM images of FTO deposited on textured and untextured substrate

Thus with texturing of the substrate on which FTO is deposited, along with inherent nano-textures of the FTO, can enhance light scattering improving photocurrent when the TCO is applied as a front electrode in Si based thin film solar cells.

B XRD measurements

X-ray diffraction analysis (XRD) is a non-destructive analysis that can be used to determine the crystallographic structure of a material. X-rays are incident on the material and then the scattering angles and intensities of the X-rays that leave the material are measured [20].

XRD anlaysis was done on two distinct samples to note the change in crystallite orientation. The sample with highest water concentration and the new baseline recipe were chosen for this purpose. The thickness and roughness parameters are tabulated in Table 13.

The sample with the highest water concentration H_2O/TTC was analysed here and can be found in Figure 58. The Al-TCO stack was laminated on glass. The Aluminum side of the stack was laminated (similar to the PEN lamination process detailed in Section 4.1) and the TCO was exposed. Lamination of Aluminum side on glass substrate was done to improve the measurement to avoid the curling of the foil with TCO deposited on top (due to compressive strain by TCO), since XRD is a sensitive measurement technique. The diffraction peaks in all XRD spectra correspond to Al from the temporary substrate and the SnO_2 deposited. Dominant SnO_2 peaks are those from (101), (110), (200) and (211) planes corresponding to 2 θ values of 36.317, 26.489, 38.368 and 51.520 respectively. The molar ratios for the process gases in this experiment are HF/TTC = 0.3, water/TTC = 19.7 and methanol/TTC = 0.005.

It was observed that the most prominent peaks for the sample with highest water concentration was (101). The corresponding crystal orientations in the order of their dominance can be found in Figure 59. Here one corresponds to (101) which corresponds to pyramidal features with a dimple on top. From [18], it is known that the (101) orientation compares to pyramidal structures with blank faces (a dimple on top). The second most prominent peak is (110) which according to Matsui et al, are triangular pyramidal shaped crystallites [18]. These crystallites tend to have the lowest surface energy and hence are dominant. The next most dominant crystal orientation from the XRD are (200) (with prismatic features) and (211). According to [18] the orientation (200) has the fastest growth speed.

The molar ratios for the process gases for the baseline recipe are HF/TTC = 0.4, water/TTC = 6.5 and methanol/TTC = 0.0018. From Figure 58, the most prominent peaks for the baseline recipe is (200) followed by (110). (101) peak seems to be suppressed, but this could be an artifact of the measurement as the corresponding crystal feature (pyramidal with dimple on the cheek) can be observed in the SEM images in Figure 61 [18]. Here one corresponds

to the prismatic features observed when the crystal orientation has a dominant (200) peak. Two corresponds to the triangular pyramidal structure corresponding to crystal orientation (101) while three corresponds to the pyramidal structure with the dimple on top, this is the most commonly observed morphology in the baseline recipe.

Apart from the suppressed (101) peak the other dominant peaks observed concurs with the crystal orientations observed at high temperature depositions around 500 °C in literature [20], [13]. According to [33] and [32],it was observed in the past that the preferred crystal orientation had an impact over the stress in the TCO-Si part. If the dominant crystal orientation is (200) instead of (211), then the stress in the layers lead to delamination at TCO-Si interface or cracks in the TCO [33], [32]. According to Schlatmann in [33], large mechanical strain in the TCO layer leads to larger interfacial sheer stress on TCO-Si interface on etching of the Al substrate. This was also what was observed in literature [35].

From SEM analysis done on this TCO, several cracks were observed in Figure 60. This could be due to the absence of plastic stretching of Al (which is done to release some of the compressive strain in the TCO). From the XRD data, we can observe that there is a change in preferred crystallite orientation from (200) in the case of the sample with water/TTC = 6.5 to (101) in the case of sample with water/TTC = 19.7. This is in agreement with what is observed in literature [8]. An increase in water concentration would thus help shift the crystalline orientation from (200) to a more favourable (211) reducing interfacial stress due to crystallite orientation in TCO layers.

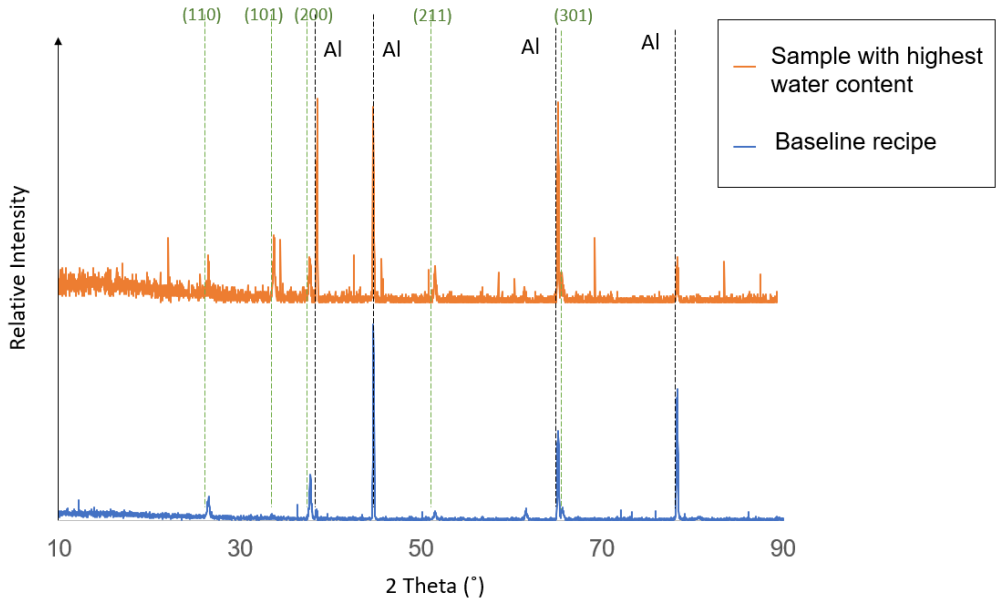

Figure 58: XRD analysis of sample with highest water concentration and baseline recipe

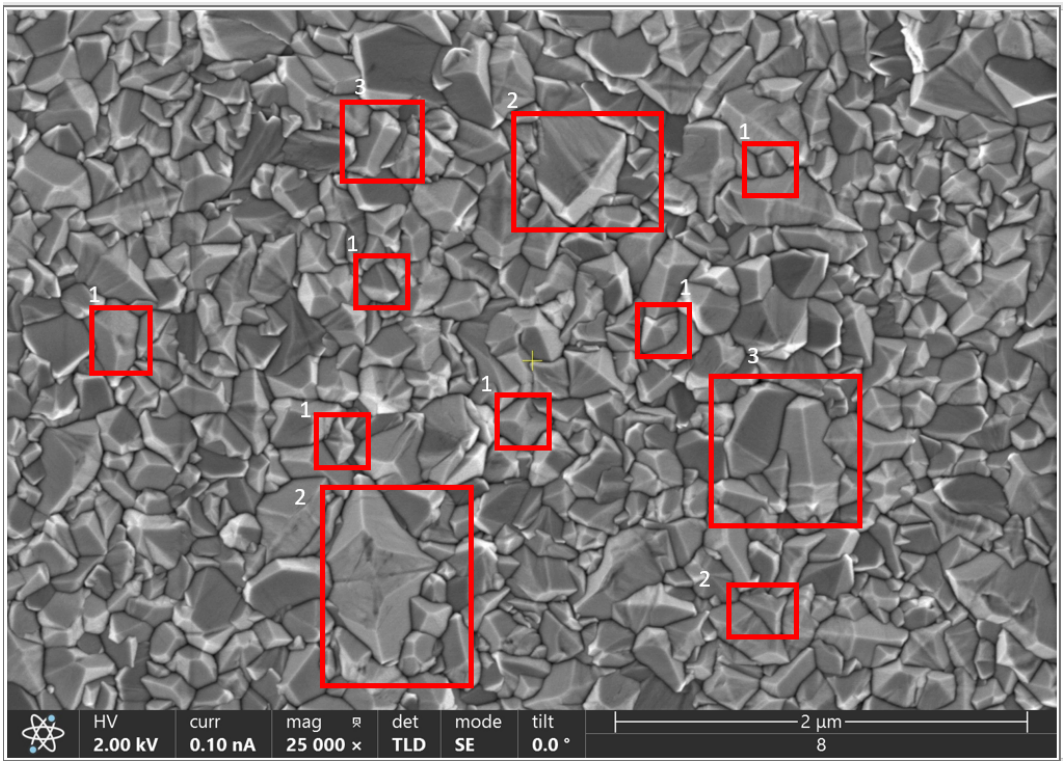

Figure 59: SEM image of the sample with highest water concentration

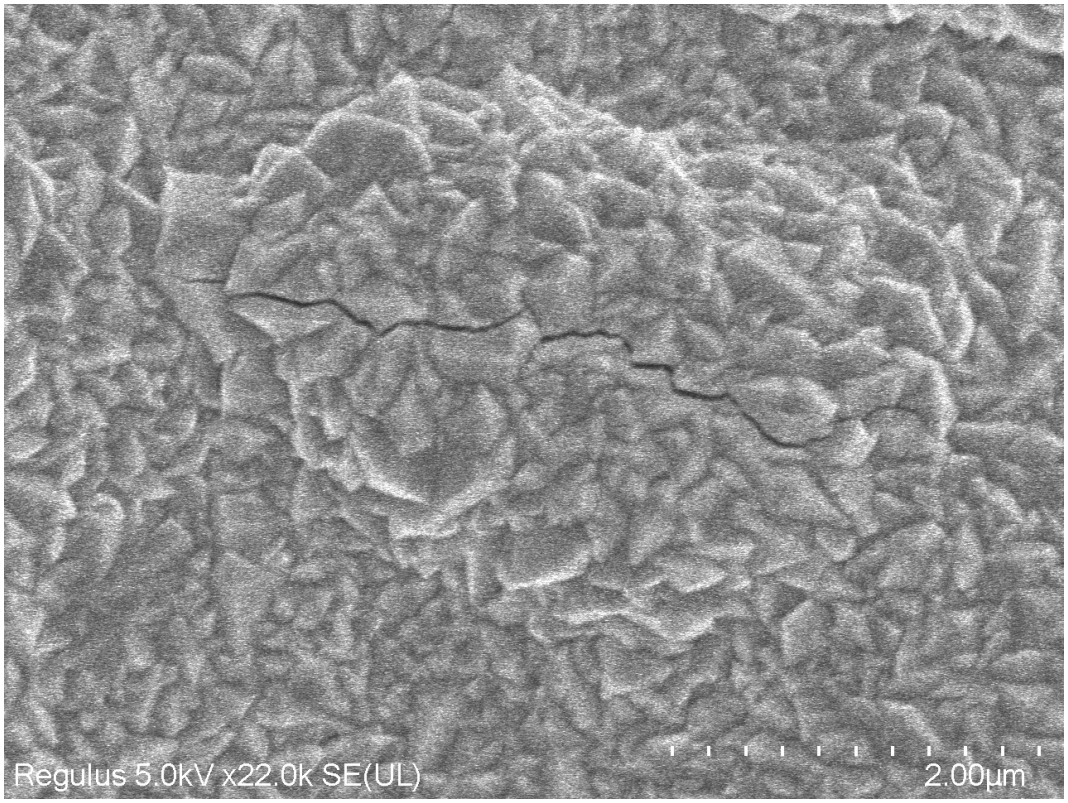

Figure 60: Cracks observed in baseline TCO

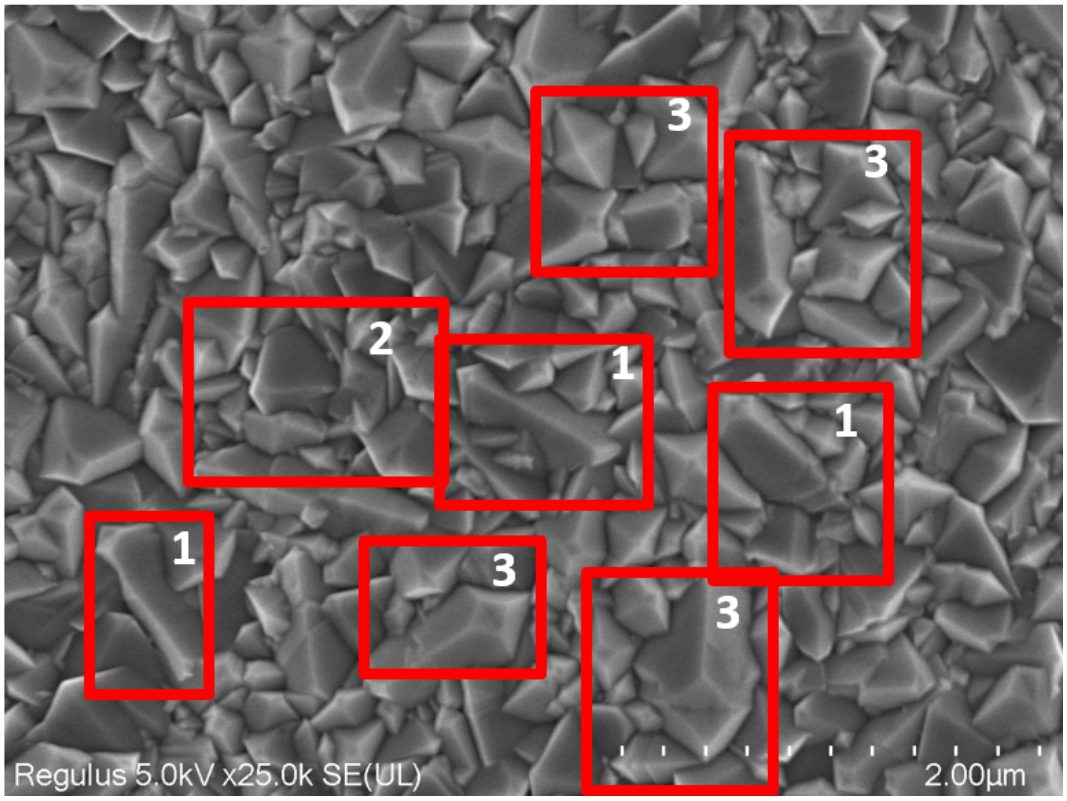

Figure 61: SEM image of the sample with baseline recipe

Parameter & measured values of	Baseline recipe	High water concentration recipe
Web speed (m/min)	0.9	0.6
Thickness of coating (nm)	747.67	776.73
RMS roughness (16x16 μm) (nm)	21.22	56.09
Max (P-V) (16x16 μm) (nm)	183.9	626
Kurtosis (16x16 μm)	3	6.526

Table 13: Measured AFM values

C Analysis of quality of deposited TCO

Initially to analyze the quality of the baseline FTO being produced, when detailed top view analysis of the TCO was done, by means of SEM, many large particles and "dark spots" were observed in Figure 62 and 63. Later an EDX and FIB analysis showed the presence of different elements under these particles and dark spots.

Several "dark spots" were observed on top of the TCO which were initially thought to be shallow valleys (grains were visible below these dark spots). These spots seemed to be centred around irregularly large grain structure. An EDX analysis showed the presence of carbon, on these dark spots thus taking the blame off the APCVD process. The dark spots were surface contamination of the top of the TCO with carbon. This carbon can easily be some random surface contamination that can be present on any air-exposed sample of TCO analyzed by SEM. So it is important that the SEM user is aware of how the carbon on top of the TCO looks like in order to avoid the time spent on analysis of these features.

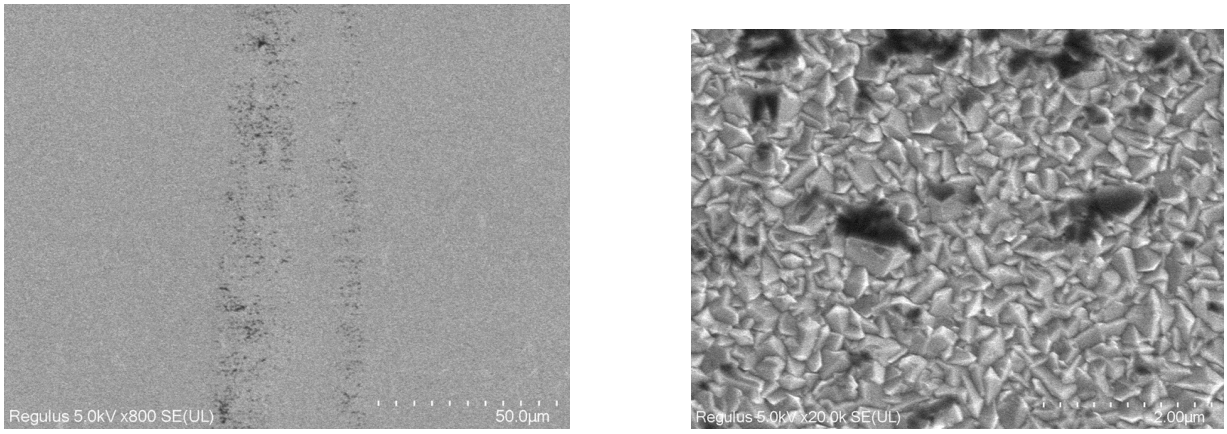

(a) A (b) B

Figure 62: A) Top-SEM of FTO deposited on top of Al using APCVD, B) Carbon detected on dark spots

In the pre-treated foil, several particle clusters were found. The TCO seems to grow uniformly over these particles, covering them completely. A FIB-SEM analysis revealed the presence of Fe and Si particles beneath these particle clusters in Figure 63.

In focused ion beam-scanning electron microscope (FIB-SEM) the ion-beam is added to cut into the material while the SEM carries out high-resolution imaging. A 3D stack of data of the sample can be built by cutting layer-by-layer at the nano-metre scale.

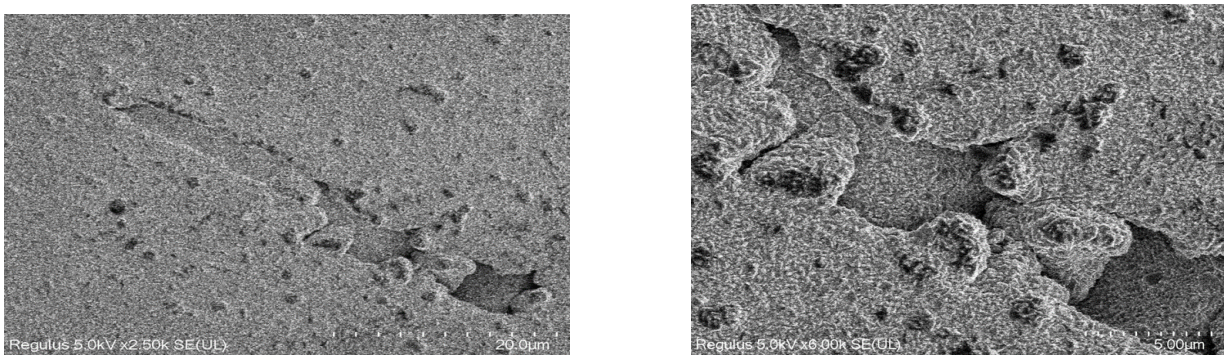

(a) An overview of deposited FTO (b) particle cluster observed on deposited FTO on Al foil

Figure 63: Top-SEM of FTO deposited on top of Al using APCVD

It can be seen that the APCVD process is blameless in this aspect as the growth of the TCO crystals grow over the Fe and Si Alloy particles. Further, an EDX analysis over the FIB area showed the presence of Fe and Si in the bumps.

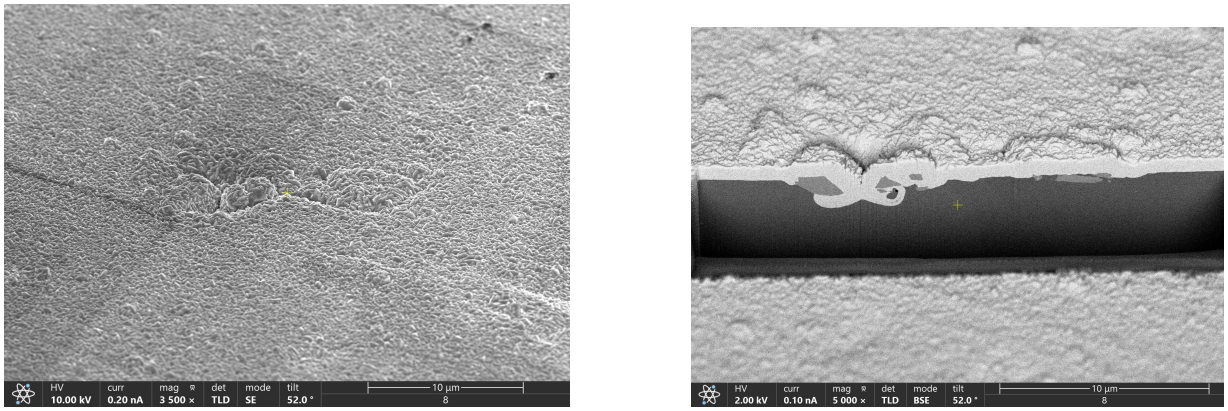

(a) An overview of deposited FTO

(b) particle cluster observed on deposited FTO

Figure 64: FIB-SEM analyis of particle coverage over FTO

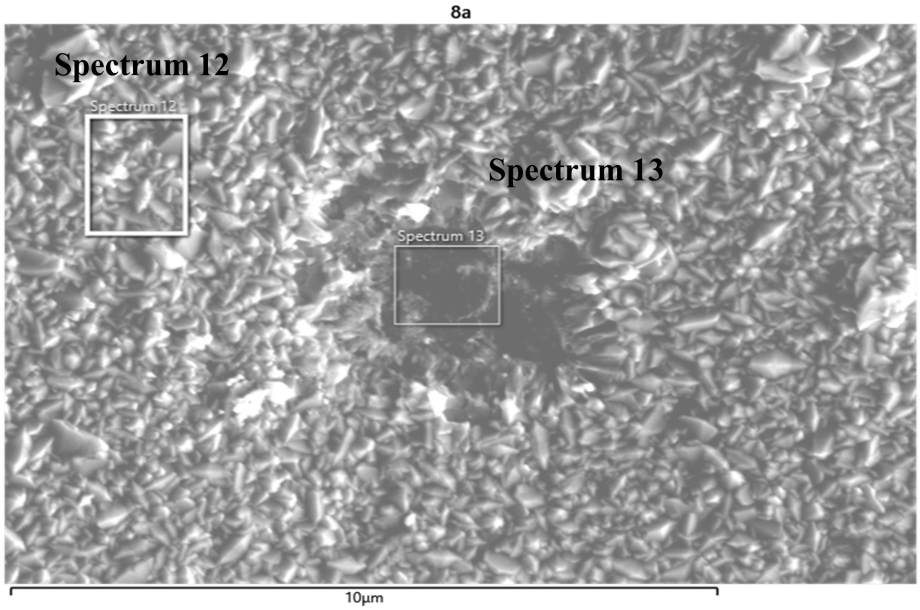

Figure 65: SEM image of fallen out piece of TCO exposing Fe particles beneath

A SEM analysis in Figure 65 of the top surface of the TCO revealed some defects on the surface of the TCO layer. There appeared to be a crater on the surface of the TCO. An EDX analysis of this portion revealed the presence of Fe and Si and a reduced amount of Sn. This can be seen in Figure 67. A reference EDX was taken on a visually defect-free area of TCO which can be seen in Figure 66 to compare with the EDX taken in 67. The presence of a small amount of Sn indicates that there was tin oxide deposited over the portion where Fe and Si has been detected in the EDX. It can be visually seen that there is accumulation of material at the breaklines due to buckling. It is likely that this due to the presence of compressive strain on cooling. There is a large difference in thermal expansion coefficient between the Al substrate and the TCO film, due to thermal stress which might have led to the cracking of the film which releases the compressive strain of the TCO [29]. In the production process, the TCO goes into the stretching unit to release the compressive strain. But these were experimental rolls which did not go through the stretching unit, it is very likely that this resulted in the cracking of the TCO. This analysis has to be repeated after stretching process, to check the quality of the TCO after stretching. The experimental rolls should thus be subject to stretching process before making lab-scale modules, as there could be crack formation and de-lamination (due to large difference in shrink rate between film and substrate) of the TCO-Si interface in the absence of stretching.

From previous analysis of TCO samples, it is clear that APCVD deposits conformally over the surface of the substrate. From past data analysis it is highly likely that the Fe-Si alloy that is usually present in the depth of the

aluminum foil, got further exposed to the surface of the Aluminum due to pre-treatment of the foil (etching with NaOH) and consequent ultrasonification. The deposition is conformal over the substrate surface. The portion of TCO deposited over the Fe-Si alloy could have fallen out later possibly due to bad adhesion due to excessive stress build-up between the layers (of Fe-Si and TCO) which leads to cracking or delamination of the film. It is crucial that the TCO should be free from defects as the presence of defects of this nature could cause shunt paths in the device after deposition of subsequent layers.

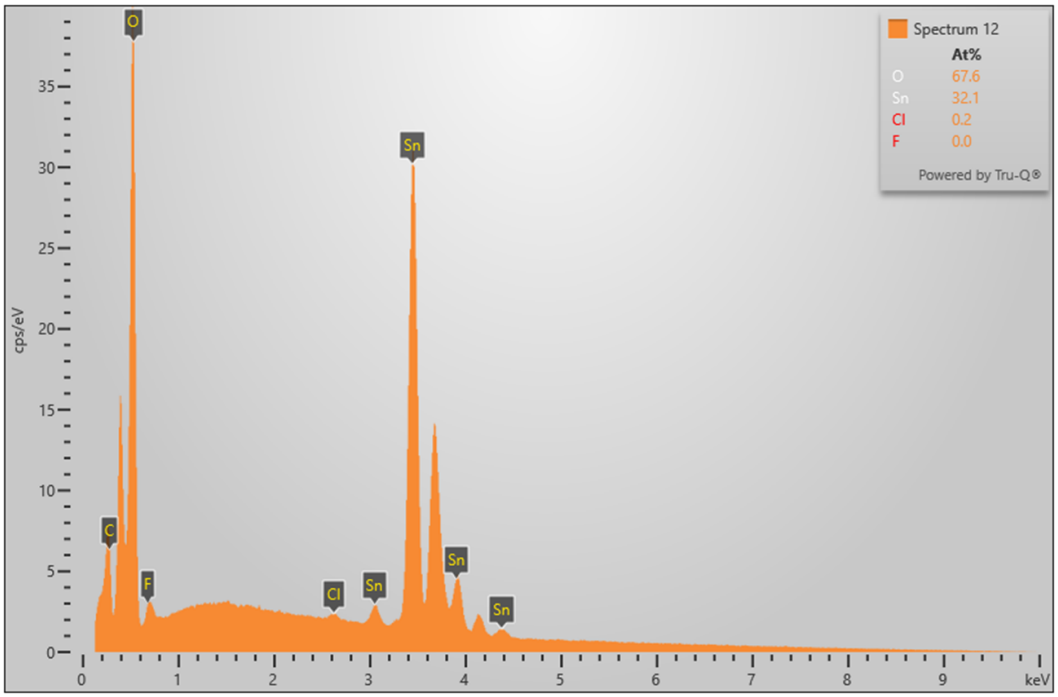

Figure 66: EDX analysis of spectrum 12 (Reference spectrum)

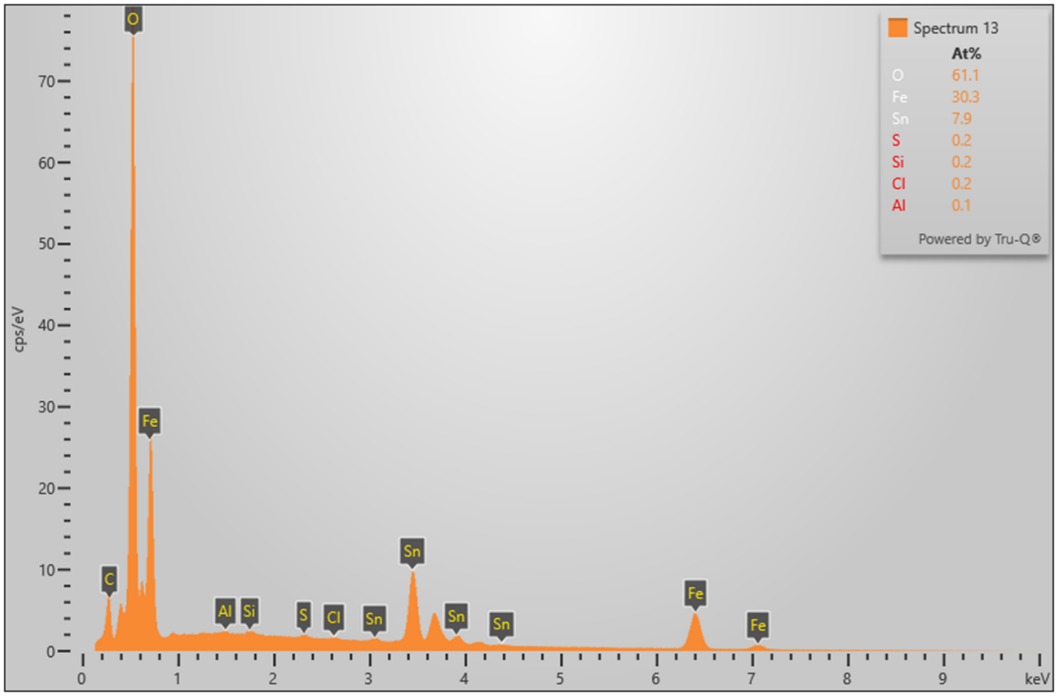

Figure 67: EDX analysis of spectrum 13 (spectrum from fallen out piece of TCO)

Finally, a leaktest was done as explained in section 4.5 to detect the presence of pin holes and defects and the average value recorded over 3 10x10 samples was 24 seconds. For the baseline material the leak test time was around 34 seconds. This confirms the presence of a larger number of pin-holes and defects in the sample with the largest water content. This is probable due to higher growth rate, reduced nucleation density than the sample with the baseline recipe.

D Mounting of the injector : Safety model for LAC

The vapor flow pattern between the injector and the substrate layer is one of the most crucial process factors affecting the deposition width. The injector design, injector functioning, and injector positioning all have an impact on the laminar vapor flow, which is powered by forced convection. The out-diffusion of gases through the narrow slits on the top, bottom, and side openings of the injector is crucial for safe operation of the tool. Depending on the distance between the injector and the vacuum table, the gas may enter from or escape to the exterior domain.

Figure 68 shows the side opening which is a 1 mm high gap between the side of the injector and the vacuum table. Fluid can both flow into or out of the domain, however, only perpendicular to the opening. Through this side opening gas may enter from or escape to the exterior domain. The injector-substrate height is an important factor that influences the flow pattern and it also affects the leak rate of the hazardous gases to the atmosphere.

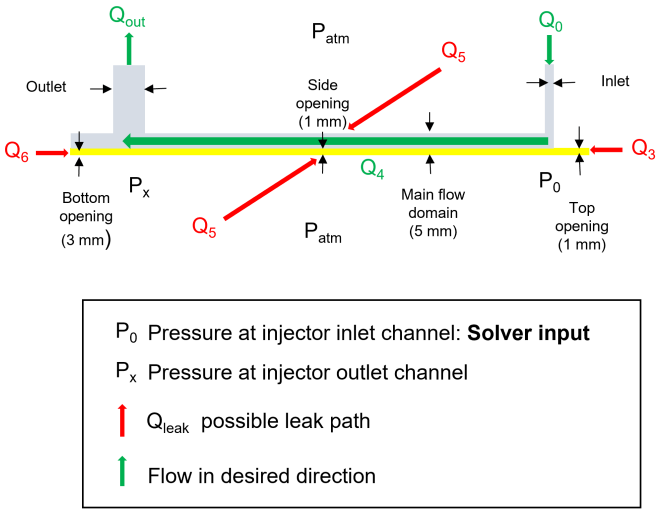

Figure 68: Side view of injector used in the LAC. Figure adapted from [28]

The Peclet number is the ratio between the convective and diffusive transport. It plays an important role in determining whether a particle may cross (due to diffusion) a counter flowing medium. Here the laminar flow is the counter flowing medium (it is the flow of the process gases in the laminar direction, Q4). To determine the safe mounting distance between the injector and the substrate, the Peclet number was calculated.

According to Hamers in [36], the general form of pressure drop over a geometry is given by,

$$\delta p = F\phi_v \tag{16}$$

where δp is the pressure drop [Pa], F is the geometry and gas dependent factor [Pa s/m^3], and ϕ_v is the volumetric gas flow through the restriction.

The gas flow Q is given by,

$$Q = p\phi_v \tag{17}$$

therefore,

$$Q = (F^{-1})p\delta p \tag{18}$$

where p is the gas pressure.

For our injector geometry, we consider out-diffusion through a slit, between two plates. The geometric factor F for this is given by [36],

$$F = bd^3/12l\eta \tag{19}$$

Here d is the short side opening, b is the long side opening, l the length of the slit.

Therefore Q_{leak} through the slit is given by,

$$Q_{leak} = (bd^3/12l\eta) * (p\delta p) \tag{20}$$

This is not a general form for flow through a restriction. The geometric factor is specific to the injector slit geometry. However, since the gas locks are so crucial, this geometry is treated throughout the calculations [36].

The Peclet number Pe is a measure for the ratio between the convective and diffusive transport [36] and is defined as,

$$Pe = lv/D \tag{21}$$

where D is the diffusion constant of the hazardous gases. In order to avoid diffusion, the condition Pe $\gg$ 1 should hold.

The velocity v of the gas molecule is,

$$v = Q_{leak}/Ap_{avg} \tag{22}$$

where A is the size of the area perpendicular to the flow direction, p_{avg} is the average pressure.

The chance of finding a particle is given by [36],

$$chance = exp(-0.5P_e) \tag{23}$$

A simplified safety model based on two-dimensional flow was built on Excel under the guidance of Edward Hamers, using the inbuilt solver function to obtain the leak rates of the gases through the top, bottom, and side openings of the injector. Using this leak rate, the velocity of the gas molecules, the Peclet number, and the chance of diffusion of the hazardous gases were estimated.

The input parameters for the model are the height difference between the vacuum table and the injector, the pressure drop over the channel (assuming only Q_0), the geometric dimensions of the injector, the mass flow rates at the inlet, and the exhaust.

The objective function is to minimize the difference between the difference of the flow rates over the channel and at the exhaust (mass balance) to zero by adjusting the pressure P_0 at the injector inlet channel.
The mass flow rate, Q_{out} at the exhaust was estimated across orifices of different diameters using the following equations (some back of the envelope calculations).

$$Q_{out} = \frac{C_d}{\sqrt{1-\beta^4}} \frac{\pi d^2}{4} \sqrt{2\Delta p \rho_1} \tag{24}$$

$$\beta = \frac{orificediameter(d)}{pipediamter(D)} \tag{25}$$

where C_d is the coefficient of discharge of the orifice, δp is the measured pressure drop across the orifice of diameter d, ρ_1 is the density of the fluid.

The mass flow rate through the exhaust changes due to the change in pressure drop across the orifice, which is influenced by change in the orifice diameter. This also influences the leakage rate of the gases through the slits.

To simplify the calculations the fluid was assumed to be incompressible and the pressure was assumed to be homogeneous along the width of the injector. The pressure in the channel was estimated with respect to the pressure at the inlet.

Thus Q_{leak} was estimated. Using this, the velocity of the gas molecules was determined. Furthermore, the Peclet number was calculated and the chance of finding the hazardous gas particle due to diffusion was calculated and can be visualized in Figure 69.

The diffusive flow will scale with the area bd. The flow of the hazardous gases due to diffusion has been theoretically quantified by taking into account the diffusive transport in a convective flow. This can be approximated to [36] ,

$$Q_{diff} = \frac{bdDp\delta pexp(-0.5P_e)}{l} \tag{26}$$

Here pδp has been approximated to P_{atm}.

The Peclet number was thus used to calculate the diffusive flow rate, Q_{diff} for the top, bottom, and the side of the injector. This was then multiplied by the fraction of the hazardous gases in the gas mixture to estimate the diffusive flow rate of the hazardous gases.

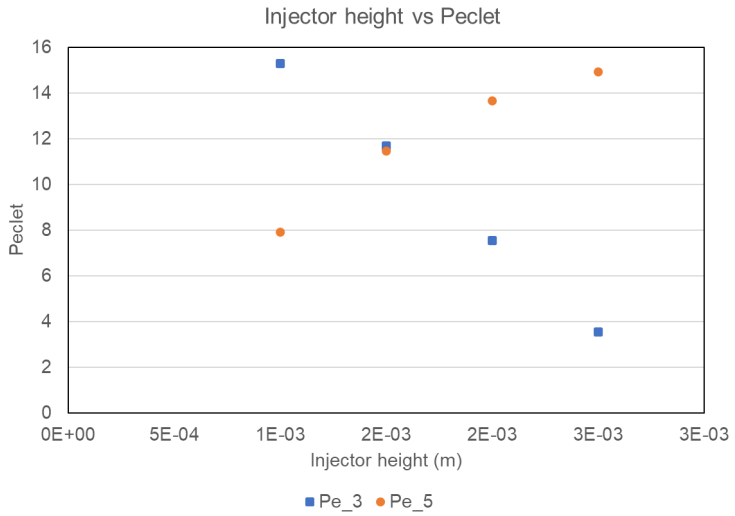

Figure 69: Peclet number for dominant leak flows Q_3 and Q_5 different injector-substrate distances

The Peclet number drops with increasing distance between the substrate and injector for flow direction at the top of the injector. The diffusive flow in this slit becomes dominant with increasing injector-substrate height due to the increase in average pressure while the diffusive flow at the side slit drops due to a decrease in average pressure. Based on the result of the model, a safe distance of the injector-substrate height was estimated to be 1.5 mm.

D.1 Problems encountered in getting the LAC operational

This section contains information on the summary of the problems encountered when getting the LAC operational and how they were solved.

During the first deposition, the table was stuck under the injector due to thermal expansion of the stainless steel table on heating to 550 °C. The injector- substrate height was modified after checking with the safety model and

the injector-substrate height was set at 2 mm from 1.5 mm.

During the first deposition on the LAC, it was realized that even after stabilising the $SnCl_4$ through the pipelines, the LFM of tin tetra chloride was fluctuating very rapidly between 20 and 110 g/hr within the span of a few seconds; the rapid switch in the controller output was due to an error in the integral constant. The controller had to be tuned again with the chemicals running through the lines (so the gain constants were set at default values and now had to be tuned and calibrated for the fluid running through the system). Figure 70 shows a screen capture from the Bronkhorst flow suite software with fluctuation in controlled output during a test run.

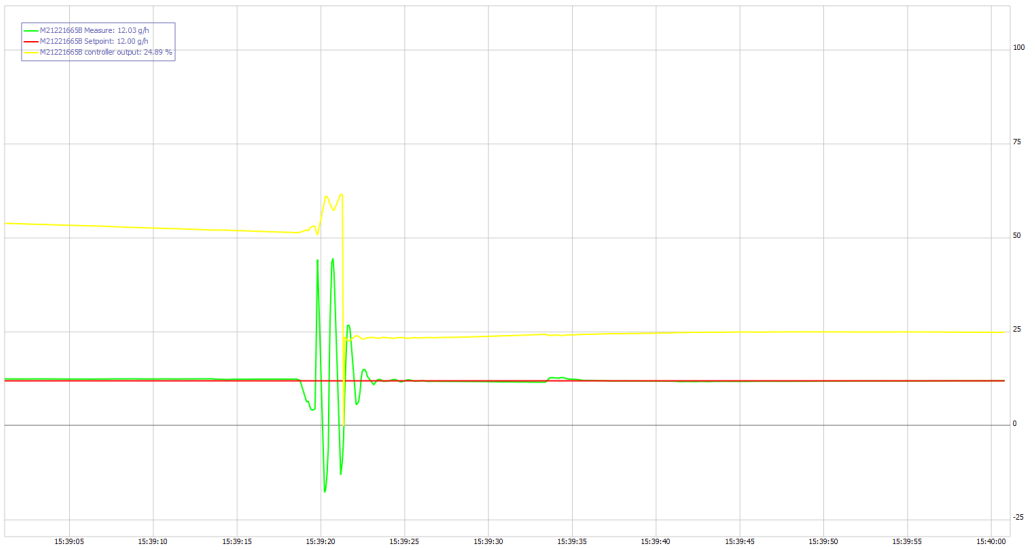

Figure 70: Fluctuation of controller output on changing set point

The Proportional term PID-Kp was first set to a fixed value. Then the integral term PID-Ti was adjusted to correct the offset in sufficient time for the process before causing instability until controller was fast without overshoot (Ti was reduced). Finally, PID-Kp was increased until the controller is fastest without overshoot. Figure 71 shows the instrument settings window of the Bronkhorst PID controller.

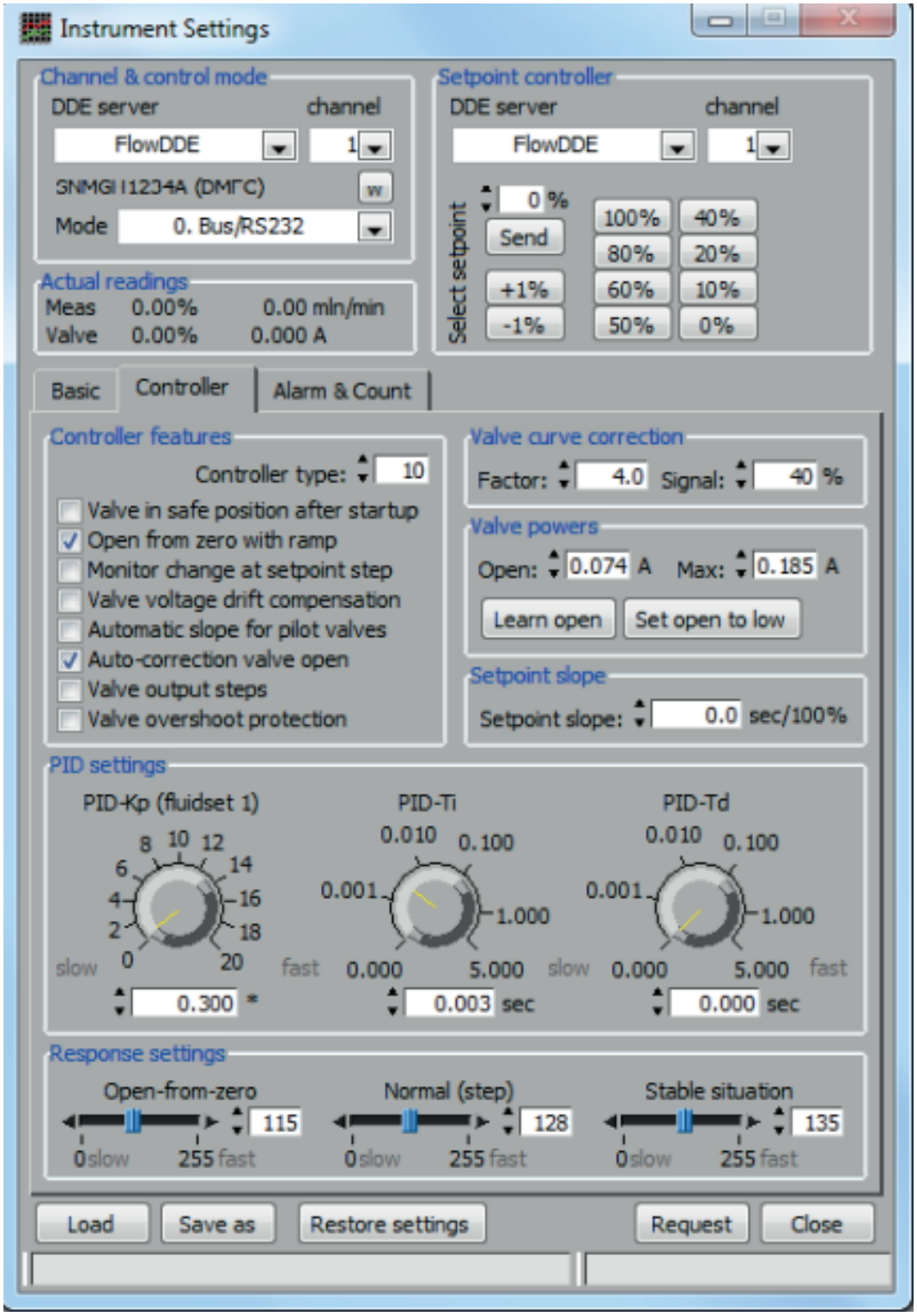

Figure 71: Instrument settings window of the Bronkhorst PID controller

During the second deposition, there was no deposition in one portion of the foil so a subsequent deposition was made and the substrate passed twice under the injector.

Then the speed of the table was varied and the diameter of the orifice was changed in an attempt to influence the pressure in the exhaust.

After these set of experiments, a deposition pattern was noticed along the width of the injector. The injector was heated to 150 °C with oil heating. The substrate was heated to 550 °C and the middle portion of the substrate was placed below the injector, so the injector could have been heated upto more than 150 °C by radiative heating from the substrate and hence a small portion of the gases could have been deposited along the width as it could have been radiatively heated to around 250 °C which is the minimum temperature required for the deposition of TCO. Flakes of white particles were found sticking to the exit of the injector leading to the belief that the injector was clogged.

Then the injector was taken apart and cleaned. Severe clogging was noted in the injector inlet channel. After cleaning the injector, hot nitrogen was used to purge the pipelines to the scrubber in an attempt to get any clogging out.

It was observed that the liquid flow meter (LFM) did not respond to changes in set point. The TTC connection was bypassed and the LFM was connected to the nitrogen mass flow controller (MFC) and the flow was checked. The LFM was functional. The pipelines leading from the TTC vessel could be clogged. To unclog the lines, the lines were purged with hot nitrogen and it was attempted to deposit again. This did not succeed. The valves that led to the vesssel were taken out and cleaned with Iso-Propanol (IPA), severe clogging was found in the valve right on top of the mix block indicating that the temperature tracing was not functional. The tracing was changed and all the pipes leading from the TTC supply to the controlled evaporator mixer (CEM) were cleaned systematically to remove the clogging.

Clogging was severe and vapors of HCl were observed every time the valves and pipes were disconnected. The valves and pipelines were disconnected with personal protective equipment. TTC is extremely volatile in air and forms HCl, a corrosive gas readily with moisture present in air. Hence, TTC should always be handled in an inert atmosphere.

After this cleaning procedure, nitrogen was used to flush the lines down the scrubber systematically for over 10 hours. A leak test was done to verify the system was leak tight and an attempt was made for the next deposition. It was realized that the LFM was clogged when it was attempted to purge the TTC through the lines to the scrubber using nitrogen.

It was understood that the gas had to be heated to 150 °C to prevent moisture from beading up and sticking to the wall of the pipes. TTC could have reacted with the moisture sticking to the inside of the pipelines and formed intermediary chloride compounds which clogged up the inlet to the LFM.

The LFM was taken apart and the mechanical parts of the LFM were immersed in IPA and cleaned in an ultrasonic bath for two hours. The setup was tested after this by directly connecting it to a Mass Flow controller (MFC), and an attempt was made to change the setpoint. The LFM responded only to very low flow values and it was realized that the LFM could be partially clogged. As a result, a pressure of 200 bars was applied and the residual clogging shot out of the LFM. The TTC connection was bypassed and the LFM was connected to the nitrogen MFC and the flow was checked. The LFM was functional. The clogging problem seemed to have been solved. The pipelines were purged with nitrogen heated to 150 °C for over 48 hours and a deposition was attempted again.

This time the controller output of the mix valve on top of the CEM fluctuated rapidly. Attempts were made to troubleshoot the CEM system. The LabVIEW program was bypassed and the CEM was connected to the Bronkhorst Flowsuite software though RS232 communication.

It was found that the mix valve opened and closed rapidly which resulted in a rapid clicking noise in an attempt of the controller output to stabilise, but it kept rapidly switching and it was not possible for the process value to reach the setpoint. The setpoint was changed multiple times in order to check the response of the system and the clicking continued, with no gas flow detected at the CEM outlet.

The CEM was taken apart and the mix valve assembly, the piston on top of the CEM, was immersed in IPA and cleaned in an ultrasonic bath for over two hours. Finally, the set up was verified to work by connecting it to a MFC and checking the controller output response.

A deposition was attempted again. This time it was found that the quick valve connector at the TTC inlet was clogged. In an attempt to exchange it with a spare connector, the nitrogen supply was turned off and an attempt was made to remove the quick ball-lock connector.

The vessel was pressurized with 4 bars of N_2 prior to the attempt to open the quick ball-lock connector. Before releasing the ball-lock connector the presure was released according the pressure meter in the TTC line. However there still was pressure on the vessel when releasing the quick ball-lock (The manual over-pressure valve had not been released). The safety valve failed to release the pressure safely and 800 g of TTC leaked rapidly through the outlet of the TTC vessel. The fumehood was closed and IPA was sprayed over contaminated items before disposing them off in the hazardous waste container.

It is possible that the safety valve had failed due to the corrosion of the stainless steel spring inside the TTC vessel. The vessel was 304 stainless steel which had to be replaced with 316 stainless steel (which is corrosion resistant).

E Poor deposition due to clogged injector in the production APCVD machine

This sections contains the pictures of the clogged injector and resultant striping and splatters in the foil as a result of the malfunction in the exhaust.

(a) Homogeneous thickness - TCO without striping

(b) TCO with splatters and striping HF/TTC = 0.2

Figure 72: Striping and splatters in the foil as a result of injector clogging

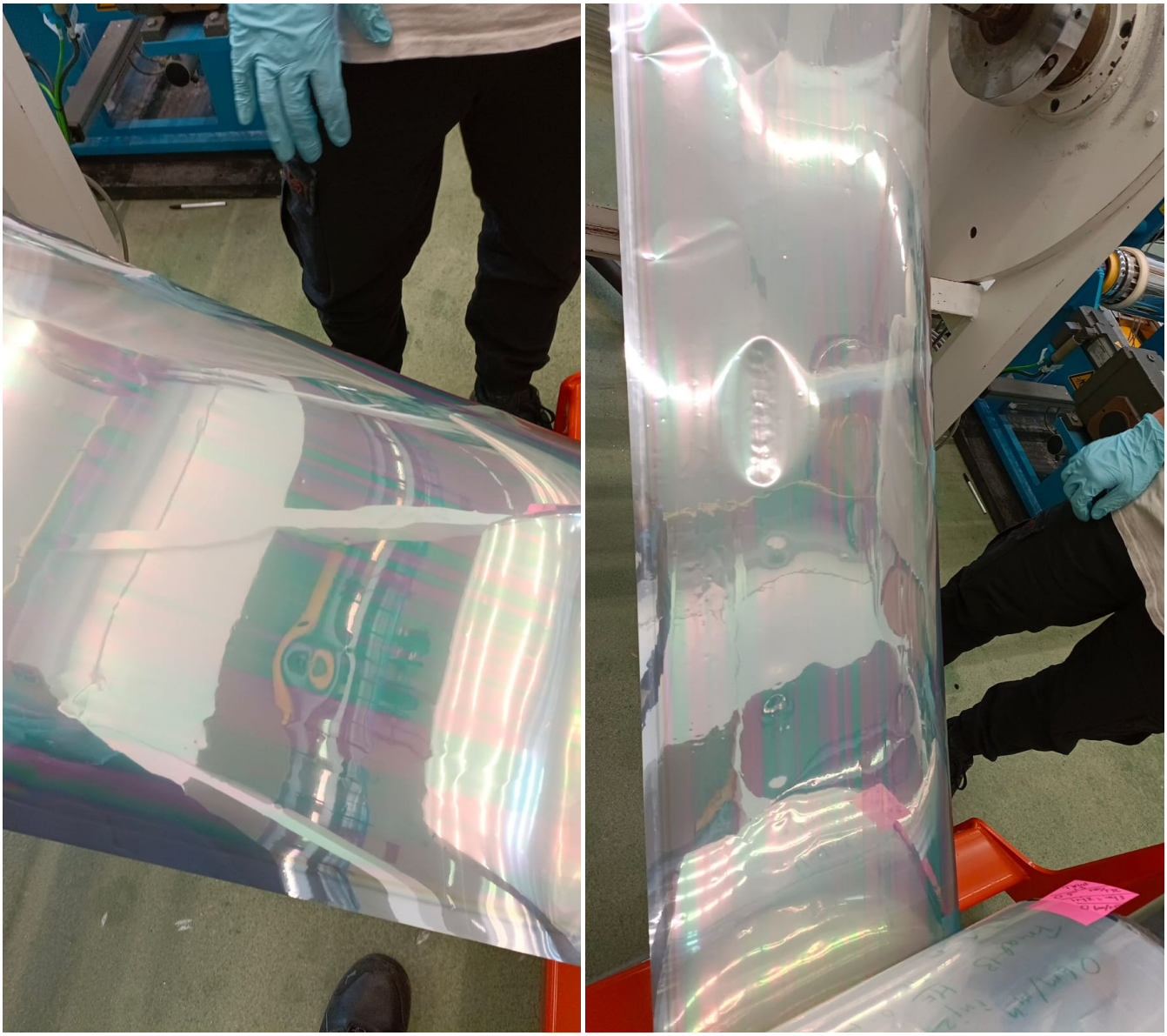

(a) TCO with splatters and striping HF/TTC = 0.3 (b) TCO with splatters and striping HF/TTC = 0.4

Figure 73: Striping and splatters in the foil as a result of injector clogging

List of Figures

List of Tables

References

[1] "Longi, nov 2022 [online]." Nov 2022. [Online]. Available: https://www.longi.com/en/

[2] HyETSolar. Thin film composition. [Online]. Available: https://www.hyetsolar.com/Thin-Film-Solar/thin-film-composition/

[3] K. Jäger, J. Lenssen, P. Veltman, and E. Hamers, "Large-area production of highly efficient flexible light-weight thin-film silicon pv modules," in *Proc. 28th European Photovoltaic Solar Energy Conf., Paris, France*, 2013, pp. 2164–2169.

[4] B. Macco and W. M. Kessels, "Atomic layer deposition of conductive and semiconductive oxides," *Applied Physics Reviews*, vol. 9, 12 2022.

[5] M. Afzaal, H. M. Yates, and J. L. Hodgkinson, "Translation effects in fluorine doped tin oxide thin film properties by atmospheric pressure chemical vapour deposition," *Coatings*, vol. 6, no. 4, p. 43, 2016.

[6] Y. Matsui, M. Mitsuhashi, Y. Yamamoto, and S. Higashi, "Influence of alcohol on grain growth of tin oxide in chemical vapor deposition," *Thin Solid Films*, vol. 515, pp. 2854–2859, 1 2007.

[7] C. Drosos and D. Vernardou, "Perspectives of energy materials grown by apcvd," *Solar Energy Materials and Solar Cells*, vol. 140, pp. 1–8, 2015.

[8] C. Y. Kim and D. H. Riu, "Texture control of fluorine-doped tin oxide thin film," *Thin Solid Films*, vol. 519, pp. 3081–3085, 3 2011.

[9] A. H. Smets, K. Jäger, O. Isabella, R. A. Swaaij, and M. Zeman, *Solar Energy: The physics and engineering of photovoltaic conversion, technologies and systems.* UIT Cambridge, 2015.

[10] C. Habis, J. Zaraket, and M. Aillerie, "Transparent conductive oxides. part i. general review of structural, electrical and optical properties of tcos related to the growth techniques, materials and dopants," *Defect and Diffusion Forum*, 2022. [Online]. Available: www.scientific.net.

[11] R. Klein, "Uv-vis-nir transmission and haze measurements of tco samples on foil, hyet internal literature," *Hyet Solar*, vol. M05053, p. 6, 11 2005.

[12] Archer, "Investigation of large grain transparent conducting oxide layers for increased optical transmission, hyet internal literature," *Hyet Solar*, vol. MT-RAP-2008-00896/rie, p. 28, 12 2007.

[13] M. Gotoh, Y, "Effect of methanol addition on formation of tin oxide films by cvd, 34(2), 123," *Asahi Garasu Kenkyu Hokoku*, vol. 34(2), pp. 123–140, 1984.

[14] W.-H. Baek, M. Choi, T.-S. Yoon, H. H. Lee, and Y.-S. Kim, "Use of fluorine-doped tin oxide instead of indium tin oxide in highly efficient air-fabricated inverted polymer solar cells," *Applied Physics Letters*, vol. 96, no. 13, p. 133506, 2010.

[15] S. Das and V. Jayaraman, "SnO_2: A comprehensive review on structures and gas sensors," *Progress in Materials Science*, vol. 66, pp. 112–255, 2014.

[16] C. Habis, J. Zaraket, and M. Aillerie, "Transparent conductive oxides. part ii. specific focus on ito, zno-azo, SnO_2-fto families for photovoltaics applications," *Defect and Diffusion Forum*, vol. 417, pp. 257–272, 2022.

[17] G. J. A. Mannie, "Surface chemistry and morphology of tin oxide thin films grown by chemical vapor deposition," *HyET Solar*, 2013. [Online]. Available: https://doi.org/10.6100/IR751861

[18] Y. Matsui, K. Matsuishi, and S. Kojima, "Mechanism of surface morphology development of tin oxide transparent conductive films," *Japanese Journal of Applied Physics*, vol. 51, 2 2012.

[19] I. Volintiru, A. D. Graaf, J. V. Deelen, and P. Poodt, "The influence of methanol addition during the film growth of sno 2 by atmospheric pressure chemical vapor deposition," *Thin Solid Films*, vol. 519, pp. 6258–6263, 7 2011.

[20] G. Sanon, R. Rup, and A. Mansingh, "287-301 preparation and characterization 287 growth and characterization of tin oxide films prepared by chemical vapour deposition," *Thin Solid Films*, p. 190, 1990.

[21] M. A. Olopade, O. E. Awe, A. M. Awobode, and N. Alu, "Characterization of sno 2 :f films deposited by atmospheric pressure chemical vapour deposition for optimum performance solar cells," *The African Review of Physics*, vol. 7, p. 18, 2012.

[22] Z. Remes, M. Vanecek, H. M. Yates, P. Evans, and D. W. Sheel, "Optical properties of fto films deposited by atmospheric pressure cvd," *Thin Solid Films*, vol. 517, pp. 6287–6289, 10 2009.

[23] T. Muranoi and M. Furukoshi, "309 properties of stannic oxide thin films produced from the snc14-h20 and snc14-h20 2 reaction systems," *Thin Solid Films*, vol. 48, pp. 309–318, 1978.

[24] HyETSolar. Production process. [Online]. Available: https://www.hyetsolar.com/production-process/

[25] M. Reedijk, "Influence of hf and methanol on the crystal growth of tin oxide," *Hyet Solar*, vol. F04240, pp. 10–14, 11 2004.

[26] R. N. Ghoshtagore, "Mechanism of cvd thin film sno2 formation," *Journal of The Electrochemical Society*, vol. 125, no. 1, p. 110, jan 1978. [Online]. Available: https://dx.doi.org/10.1149/1.2131373

[27] S. Goldschmidt, "Cfd simulation of apcvd injector," *HyET Solar*, vol. CSO F02005, 2005.

[28] M. Goldschmidt, "Cfd simulation of apcvd injectors," *Hyet internal literature*, vol. F04242, p. 5, 12 2004.

[29] Schlattmann, "Process settings tco properties and transfer of solar cells from al to plastic," *HyET Solar*, vol. CSO F05042, 2002.

[30] N. Duboust, H. Ghadbeigi, C. Pinna, S. Ayvar-Soberanis, A. Collis, R. Scaife, and K. Kerrigan, "An optical method for measuring surface roughness of machined carbon fibre-reinforced plastic composites," *Journal of Composite Materials*, vol. 51, pp. 289–302, 2 2017.

[31] J. H. Lee, Y. H. Kim, S. J. Ahn, T. H. Ha, and H. S. Kim, "Grain-size effect on the electrical properties of nanocrystalline indium tin oxide thin films," *Materials Science and Engineering B: Solid-State Materials for Advanced Technology*, vol. 199, pp. 37–41, 6 2015.

[32] B. Stannowski, "Hypotheses for crack forming in tco and modules, hyet internal literature," *Hyet Solar*, vol. CSO M05005, p. 5, 01 2005.

[33] R. Schlatmann2, "The influence of tco on crack forming and voc in cells and modules," *Hyet Solar*, vol. CSO M05018, p. 5, 03 2005.

[34] J. Li, S. Sathasivam, A. Taylor, C. J. Carmalt, and I. P. Parkin, "Single step route to highly transparent, conductive and hazy aluminium doped zinc oxide films," *RSC Advances*, vol. 8, pp. 42 300–42 307, 2018.

[35] J. M. Dekkers and W. P. Service), *Transparent conducting oxides on polymeric substrates by pulsed laser deposition*. s.n.], 2007.

[36] Hamers, "Gas lock dimensions and relation to impurities in plasma zone: a theoretical study," *Hyet Solar*, vol. M06068, pp. 10–11, 5 2006.